Probing planetary system histories via observations, experiments, and modelling of circumstellar gas and dust

by

Tajana Schneiderman

Submitted to the Department of Earth, Atmospheric, and Planetary Sciences
in partial fulfillment of the requirements for the degree of

Doctor of Philosophy in Planetary Science

at the

MASSACHUSETTS INSTITUTE OF TECHNOLOGY

June 2022

Author .....
Department of Earth, Atmospheric, and Planetary Sciences
May 9, 2022

Certified by .....
Sara Seager
Class of 1941 Professor of Planetary Science, Professor of Physics, and Professor of Aeronautics and Astronautics
Thesis Supervisor

Accepted by .....
Paul O'Gorman
Chairman, Department Committee on Graduate Theses

Probing planetary system histories via observations, experiments, and modelling of circumstellar gas and dust

by

Tajana Schneiderman

Submitted to the Department of Earth, Atmospheric, and Planetary Sciences
on May 9, 2022, in partial fulfillment of the
requirements for the degree of
Doctor of Philosophy in Planetary Science

Abstract

Circumstellar disks of gas and dust are integral parts of planetary systems from formation to maturation. Protoplanetary disks, the name for circumstellar material at the earliest stages of a stellar lifetime, provide key information about the formation processes of planets, and therefore of the initial conditions that set system evolution in motion. These disks are host to both primordial interstellar materials and reprocessed constituents that become part of nascent planets and planetesimals. Debris disks, the name for circumstellar material after the protoplanetary disk dissipates, are remnants of earlier processes and carry clues to the formation conditions and evolutionary pathways of mature systems. In this thesis, I discuss three approaches to probing planetary system histories by examining circumstellar gas and dust.

The first approach is to experimentally measure the desorption binding energies and entrapment efficiencies of neon, argon, krypton, and xenon in astrophysical ice analogs. Noble gases are valuable tracers of both nebular gas accretion and volatile delivery to planetary atmosphere; placing experimental constraints on these fundamental physical properties allows us to understand the extent to which each gas traces different sources of volatiles within the protoplanetary disk. We find that all four nobles are likely present in the nebular gas, and able to be directly accreted to nascent planets. We further find that argon, krypton, and xenon are trapped efficiently in interstellar ice analogs, with entrapment efficiencies ranging from 65-95% in astrophysically relevant ices. This suggests that that they are valuable tracers for the solid volatile content within the disk. Lastly, we find that neon is inefficiently trapped; maximally 10% of neon is entrapped in interstellar ices, although the actual entrapment efficiency may be lower than 1%. Thus, neon is a tracer of only the nebular gas.

The second approach is to examine archival data from the Atacama Large Millimeter Array for the HD 172555 system. This system is unique among debris disks due to its atypical dust composition. We detect the presence of carbon monoxide gas in the circumstellar debris. By considering the morphology and composition of both CO gas and dust in the system, we are able to rule out several origins for the

debris. We instead find that the only scenario that adequately describes observations of the system is that of a giant impact; the CO gas is likely the remnant of a stripped planetary atmosphere, while the dust is debris produced in the collision. These observations provide evidence for giant impacts in systems other than our own.

The third approach simulates the dust spectra of nine highly inclined debris disks for a range of compositions and particle size distributions. Multibandpass observations are required to adequately characterize dust in a system; dust spectra allow for an understanding of compositional classes of parent planetesimals, while deviations from steady-state predictions for the particle size distributions might indicate a history of giant impacts in a system. This chapter aims to develop a preliminary framework for analysis of systems in advance of data from the James Webb Space Telescope. We find that iron and troilite compositions are most easily disentangled from the suite of compositional families we consider, although silicates, water ice, and carbonaceous compounds are identifiable.

Thesis Supervisor: Sara Seager
Title: Class of 1941 Professor of Planetary Science, Professor of Physics, and Professor of Aeronautics and Astronautics

Acknowledgments

I have gratitude for more folks than I can possibly mention, as I am fortunate to have a life enriched by a caring, broad community. As I reflect on the past six years, however, there are several folks who must be directly called out as they have irrevocably shaped my journey to this thesis.

First and foremost, I'd like to thank my PhD supervisor, Sara Seager, for taking me on as a student. She has supported me as I followed my research interests, and I am immensely grateful for the opportunities she has enabled me to pursue over the course of my studies.

I'd like to also thank members of Sara Seager's research group that have supported me and offered valuable help and advice. Roberta Allard and Kayla Bauer have been excellent administrators that have ensured I had access to resources I needed, as well as provided a kind word whenever possible. Sukrit Ranjan and Janusz Petkowski have been excellent at providing feedback on talks. Ana Glidden and Zahra Essack have been wonderful friends and helpful individuals to bounce ideas off of.

I would like to thank Karin Öberg for taking me on as a second generals project student. Little did I know when I reached out to her in October 2016 that I would end up working as closely with her as I have. She has opened her lab to me, provided me with mentorship and advice, and encouraged me throughout my PhD. I'd further like to thank her for teaching the ISM class at Harvard, and telling me to reach out to Luca Matrà for my final project. At the time, I would not have suspected that an end-of-term project would end up becoming a central chapter of my thesis.

This brings me to thanking Luca Matrà for his help and collaboration in getting my first first-author paper from forgotten archival data to a fully-formed, well-received manuscript. I have learned so much during the process, and feel extremely grateful for his patience as I navigated my fledgling steps into scientific maturity.

I would like to thank the current and former members of Karin Öberg's group that have helped me over the years. Mahesh Rajappan has been an endless source of support and help in the lab; I am incredibly grateful that he has turned off experiments at the end of the day for me, saving me from a return trip to lab at 10 pm. I'd also like to thank Edith Fayolle, Jennifer Bergner, and Pavlo Maksiutenko for their help when I first joined. Rafael Martin-Domenech, Elettra Piacentino, and Alexia Simon have been excellent resources during the final year of my PhD; Rafa and Elettra - thank you for filling LN_2 tanks for me when I was hobbling around lab on crutches and helping me change out gas bottles.

I would also like to thank the members of my committee not yet mentioned - Rick Binzel, Julien de Wit, and Taylor Perron.

I of course cannot go without thanking my first scientific mentor in the planetary sciences - Pablo Sobron. I am so grateful that he both accepted me as a summer REU student at SETI, and agreed to continue mentoring me remotely for the last two years of my undergraduate studies. He encouraged me to pursue planetary sciences, and provided me with an opportunity to first begin to pursue independent research.

I find myself profoundly thankful to a group of extraordinary women who have

supported me, encouraged me, and lifted me up. What started as a semi-regular lunch group morphed into a weekly Zoom and Loom that has provided me with a stable source of companionship and advice. Clara Sousa-Silva - your mentorship has been incredibly valuable for as long as I've known you. From our first meeting, I could find refuge in your office. You were always willing to listen, brainstorm, and help. I am thankful to have met you, and benefited from your wisdom. Mary Knapp - I have always been able to rely on you for sound advice, good judgment, and answers to silly questions. Your patience in teaching me not only basic astronomy, but also spinning and weaving, is a testament to the breadth of your skills. I am also profoundly grateful for the use of your couch - you opened your home to me more times than I can count as I finished up thesis work in the last year. Thank you for giving me a home-away-from-home. Elisabeth Matthews - thank you for taking a lost disk-girl under your wing. Your scientific mentorship has been invaluable as I have familiarized myself with the broader world of direct imaging and disk science. I am also incredibly grateful for your example - your confidence has been inspiring, and I strive to speak up in the ways you have shown me. Zahra Essack and Ana Glidden - thank you for the laughs, the slack gifs, and the genuine friendship that you've offered me. It's been a pleasure to have you as both group-mates and friends.

Fiona Grant and Ana Lo - thank you for being the most excellent roommates I could have ever asked for, and for making our apartment a home for the years I lived there. Our Mambo No. 6 cocktails, pizza nights, and baking parties remain fond memories and the source of several delicious recipes.

I also want to thank two teachers from my earlier education. Mrs. Laura Tonkin - you named me most likely to become a rocket scientist. While I'm not quite a rocket scientist, I am a scientist whose work depends on rockets, and that is hopefully close enough. Your enthusiasm for science shone through and made science profoundly cool. Your belief in my abilities also gave me a sense of belonging at an age where it's critical to find that. Mrs. DeeDee Messer - thank you for showing me that women could be physicists. Thank you also for giving me my first ever B. Although I was incredibly upset at the time, I'd like to think that it allowed me to accept imperfections in myself. I look back on your class as a challenging time that inspired a love for physics, and set me on the path I am on today.

I must also thank my family. Alena and Katarina - I am so grateful to have two amazing younger sisters who are clever, kind, and generous. It's an immense privilege to be your sister, and I am grateful that you have been so patient with me. I don't always live up to the responsibility of being a sister, but you both are gracious when I struggle. Mama and Dad - thank you for reading "All About Space" every time I asked for it. It gave me a chance to dream. Thank you also for building my resiliency and drive - I am a better person for being your daughter. Mama - thank you for being a scientist before me and taking me into lab when I was small, to show me that women can be and are scientists.

Babka, Dedko - každe leto ste sa o mňa starali, vychovávali a kŕmili. Najkrajšie spomienky z detstva patria Vám a Slovensku. Som vďačná za to že ste mi dali lásku a blizkosť celej rodiny; za to že som mohla vyrásť medzi vsetkymi vašimi vnúčatami. Ďakujem že ste mi ukázali Európu a našu rodinu, a že ste prišli pomôct mame keď

som bola malá. Dedko - som vďačná že si ma naučil že ťažká praca je súčasťou radosti. Babka - ďakujem že si ma naučila ručne práce, varenie a pečenie. Ďakujem za všetky rozprávky a recepty, za lásku, a za to že si mi ukázala čo to je, byť úžasnou ženou.

*[**Translation:** Babka and Dedko - you cared for, raised, and fed me every summer. The most beautiful memories of my childhood belong to you and Slovakia. I am grateful that you gave me the love and closeness of our entire family; I am grateful that I was able to grow up amongst all of your grandchildren. Thank you for showing me Europe and our family, and thank you for coming to help Mom when I was small. Dedko - I am grateful that you taught me that hard work is a part of joy. Babka - thank you for teaching me how to cook, bake, and work with my hands. Thank you for all of the stories and recipes, for love, and for showing me what it means to be an exceptional woman.]*

To my darling, cuddly Wren-pup, I thank you for the endless unconditional adoration. You came home a tiny ball of fluff and have grown into a goofy dog that seems to know exactly when I'm struggling, and beelines to me to sit and beg for attention.

To Pahul Hanjra: thank you for being my person. Words can't begin to describe how profoundly grateful I am for your friendship. From our high school days, I've relied on your counsel and advice. Your willingness to pick up the phone and comfort me has been a constant that I count on - your presence through grief has made it more manageable, and your presence in joy has made it greater. It's been a sincere pleasure to go from days of shouting 'serotonin and sunshine' at each other at 2 am, to the days where we're living the dreams we talked about. In you, I've found a sister and a lifelong friend. I hope that one day we can actually live in the same city and trade in our phone calls for brunches. Until then, I will treasure our phone calls and text threads, and eagerly plan regular visits to see you. It's been a sincere pleasure to grow up alongside you; I marvel at the woman you are and the example you set.

Last, but certainly not least, I must thank Alexander Jarjour. From the time that we were juniors in quantum, you have been one of my closest friends. Falling in love with you has been a singular joy in my life, and I am so thankful that we both found the courage to speak our truth to each other. You have held me as I cried, celebrated with me through the victories, and provided a place of peace and comfort. Thank you for picking up the slack for me when I drop it, for keeping me grounded and present, for making me think critically and deeply, and for being the most scintillating conversational partner I could ask for. You have changed me, helped me grow, and grown alongside me. I don't know that I would have gotten to this point without you as my cheerleader and best friend. This thesis contains many nuggets of your wisdom, is written because of the support you have given me, and has reached completion because you have catered to my whims and needs as I have grown increasingly less tethered to to the humdrum of daily life. I look forward to helping you in this next year as you finish your thesis as much as you have helped me over this past year.

This thesis is dedicated to all the folks who told me I could and I would. Thank you for helping me through the times I thought I could not.

Contents

List of Figures

List of Tables

Chapter 1

Introduction

1.1 Overview

Planetary systems are born out of the dust of the interstellar medium; they become dust as they die. Pockets of dense gas and dust collapse to form stars and protoplanetary disks, dust within disks coagulates into larger bodies, which grow to become planetesimals and planets. As planet formation proceeds and the protoplanetary disk gas recedes, belts of icy and rocky material are left, in addition to any planets that have formed. These planetesimals collide and grind each other back down into dust that we can observe in the form of debris disks.

The building blocks of planets - gas, dust, and ice - provide key clues to the formation pathways of planets, and to the histories of planets in stellar systems. This is true when we observe protoplanetary disks, as we can see planet formation in action. It is also true when we observe debris disks, where we can see the remainders of planet formation and the processes that have modified bodies in the system.

The following chapter aims to provide an overview of circumstellar disks throughout various epochs. In section 1.2, we discuss the basics of planet formation, tracing gas and dust as they collapse from molecular clouds in the interstellar medium to protoplanetary disks around young stars. This section traces the history of systems to about 10 million years (Myr) after collapse. In section 1.3, we discuss debris disks - the remnants of planet formation after the initial protoplanetary disk has dispersed.

This section will discuss both terrestrial planet formation that is expected to be dominated by collisions and occur from approximately 10-100 Myr after collapse, as well as the phenomenon of steady-state debris disks that can last for the entirety of a system's lifetime.

1.2 Protoplanetary disks

Protoplanetary disks are rich regions surrounding young stars. They have complicated dynamics and chemistries, and are the locations for ongoing planet formation. We will briefly discuss the typical pathway of a protoplanetary disk, and then turn to discussing the typical architecture of a protoplanetary disk before reviewing planet formation within these disks.

Regions of the interstellar medium (ISM) termed molecular clouds are denser than the surrounding ISM (Figure 1-1a). The molecular cloud, which is cooler than its surroundings, consists of gas (largely molecular hydrogen and helium, with some additional volatiles) as well as silicate and carbonaceous dust [50, 30] and volatile ices. Molecular clouds are by no means uniform; some regions, termed dense cores, are sufficiently dense that the the self-gravity of the cloud overcomes thermal pressure, magnetic support, and turbulence to collapse (Figure 1-1b). At that point, the dense core begins to collapse and the center heats. To preserve angular momentum, some of the material spreads out into a disk around a central protostar, which acts to funnel material into the center. Additionally, stellar outflows and jets form, ejecting material and angular momentum from the system (Figure 1-1c). After accretion to the central star ceases, a protoplanetary disk remains to orbit the pre-main sequence star (Figure 1-1d). During this phase, giant planets complete their formation and terrestrial protoplanets form. By 10 Myr at the latest, the gas in the system dissipates, leaving a mature debris disk (Figure 1-1e). Material within the protoplanetary disk is both primordial and reprocessed. There is evidence that at least some of the primordial ices that formed within the ISM may survive the process of collapse to form planetesimals and planets [193, 35]. Some of the primordial material is reprocessed;

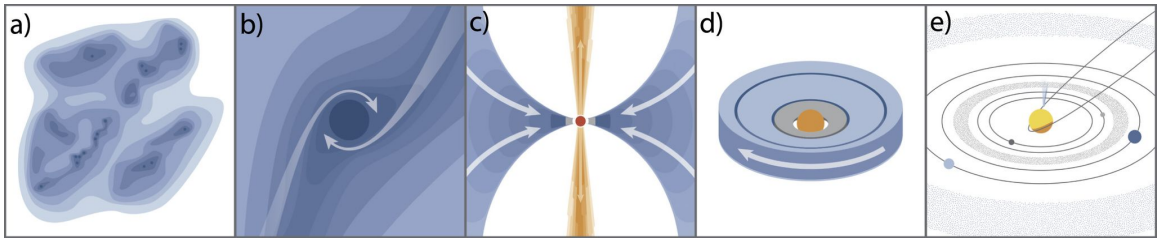

Figure 1-1: Schematic of the steps of planet formation. **(a)** Dense cores in interstellar molecular clouds. **(b)** A dense core begins to collapse due to self-gravity, starting star formation. **(c)** The center of the collapsing core heats up, the cloud becomes a disk due to conservation of angular momentum, the central protostar accretes material through the disk, and the protostar ejects stellar outflows. **(d)** The core collapse results in a protoplanetary disk orbiting the pre-main sequence star; planets form within the protoplanetary disk. **(e)** Gas dissipates from the protoplanetary disk by (at latest) 10 Myr, by which point gas giant planets have formed. Smaller planets continue to grow, and the orbital configurations and compositions of planets are modified by migration and impacts. Image reproduced from [152].

this generally occurs in the interior of the disk and along the disk surface. However, mixing within the disk due to turbulence and pressure gradients does occur, which further complicates the structure of a disk.

1.2.1 Architecture of a protoplanetary disk

Figure 1-2 provides a cartoon cross-section of disk structure as well as pictograms of processes relevant to that disk structure. The gas disk is usually flared, with gas temperature increasing towards the star and along the outside of the disk. The external surfaces are often hotter as they are not efficiently shielded from stellar radiation, allowing for heating, while the interior of the disk is more protected from stellar radiation due to dust and gas opacity. Gas density is also higher closer to the star; at higher temperatures, more volatiles are in the gas phase. As you move outwards through the disk and pass a volatile snowline, the volatile in question goes from gas to solid phase. Within the disk, gases are subject to sublimation and condensation as well as to photochemistry. Grains are also subject to growth via pebble accretion; growth results in decoupling from the gas which leads to settling and inward drift. The settling of dust grains is evident in work such as [192], which has shown that the

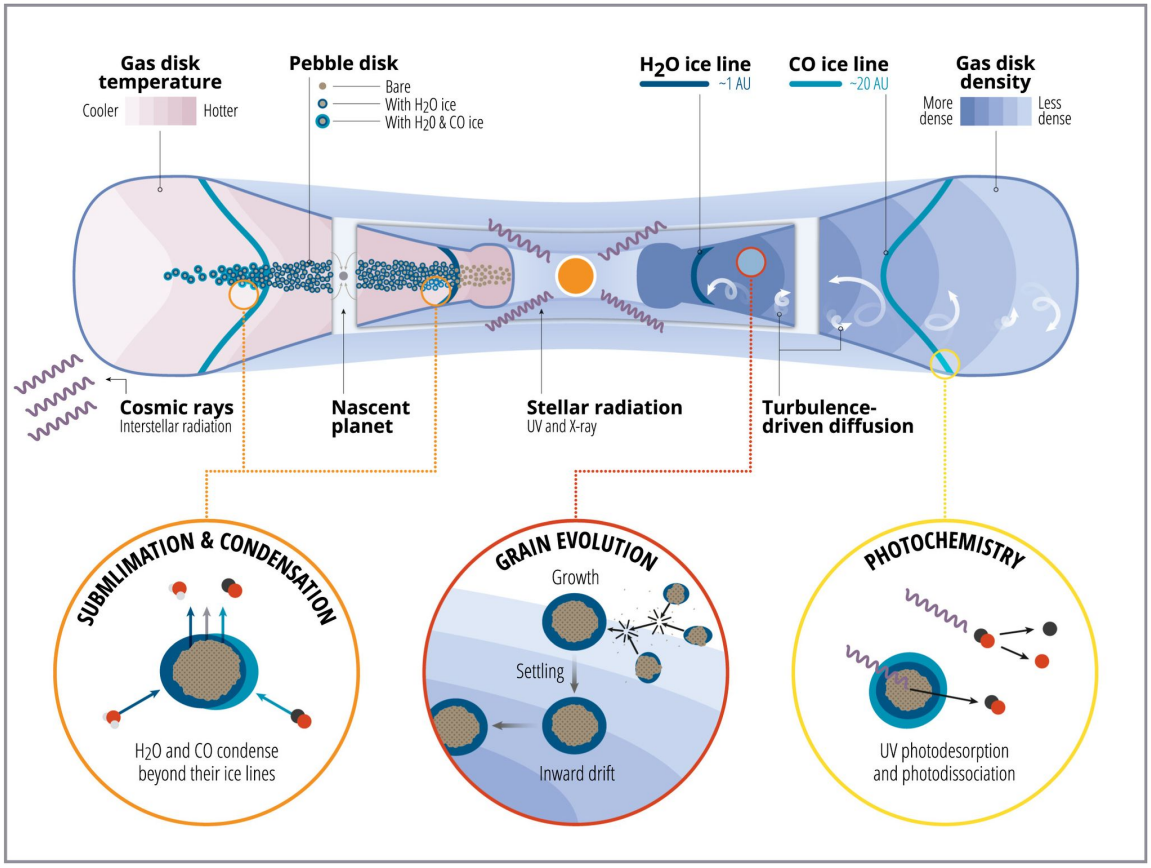

Figure 1-2: Slice-away of protoplanetary disk structure and various effects at play within the disk. Image reproduced from [152].

dust-disk within the gas disk is vertically thin and quite confined, which aligns with expectations of dust settling.

The primary features we consider when it comes to describing the architecture of a protoplanetary disk are the typical disk mass, the radial extent of disks, substructures within disks, and disk lifetimes. Many of the constraints on these features come from surveys of planet-forming regions, although experimental and theoretical work play a role in developing our understanding.

The typical disk mass is best estimated from sub-millimeter observations of thermal continuum emission [11]. This is a probe of the amount of dust present, although it is insensitive to the amount of mass in large bodies, as measurements at a given wavelength are most sensitive to thermal emission by particles of that wavelength. Thus, we expect that submillimeter observations are sensitive to particles up to a

centimeter in size [51]; mass estimates are constrained by a lack of knowledge of the size distribution above this. Further, there are uncertainties in the typical gas to dust ratio within the disk, which leads to an uncertainty in the overall mass of the disk. However, the minimum mass solar nebula (MMSN) [26] provides a lower bound on the amount of material needed for at least the Solar system protoplanetary disk; this sets the minimum mass as that required to explain the present mass of the planets and planetesimals remaining in our system, scaled to include hydrogen and helium. In addition to the MMSN being too low an estimate, there is evidence that the estimates for disk masses derived from observations are too low. For one, [4] shows that masses derived from sub-millimeter photometry are in tension with estimates of masses from accretion rates integrated over protostellar ages [69]. [64] also shows that disk mass estimates are too low to explain the incidence of giant planets detected in surveys of exoplanets. The current statistics should therefore be viewed as lower bounds on disk masses. However, comparisons between disks to identify trends are likely valid, given that the uncertainties may be similar. We see that the brightest stars lack extended disks, possibly due to rapid photoevaporation. Up to O stars, however, we see that disk masses tend to scale with stellar mass (although there is spread in the ratios). The median ratio between the disk and stellar masses is about 1% [197].

The typical extent of a protoplanetary disk is also challenging to constrain. Dust in the furthest reaches of a protoplanetary disk is cold, which reduces its emission and makes it harder to observe. The best constraints on radial extent come from [191], where images of protoplanetary disks in absorption rather than emission were taken. This survey found that outer edges up to 200 au are fairly typical, although there were two outliers in their sample extending significantly further out.

Disk lifetimes can vary significantly, although they are quite short in comparison to total system lifetimes. It is clear that by 10 Myr the vast majority of protoplanetary disks are cleared of gas. Indeed, typical disks clear their gas by 2-5 Myr [110], although there are stars that appear to be as young as 1 Myr that have cleared their disks. The c2d survey [34, 160] found that 50% of weak-lined T Tauri stars are cleared by 2 Myr. There does appear to be a stellar mass dependence on clearing time; for stars

more massive than the sun, disk lifetimes can be up to a factor of two shorter [24]. What is clear is that gas giant planet formation within the disk must, therefore, occur on rapid timescales, given that the gas necessary to build a giant planet dissipates rapidly. The following section will discuss planet formation within the planetary disk in more detail; any mechanism seeking to explain planet formation must explain it on these short timescales.

Given the rapid evolution of protoplanetary disks, it is perhaps unsurprising that significant structure has been detected within protoplanetary disks at early ages. The DSHARP program using ALMA [3] surveyed 20 protoplanetary disks and identified ubiquitous substructures. Specifically, they found rings and gaps, as well as spiral features and azimuthal asymmetries within disks. This suggests that protoplanetary disks are not uniform in having a power-law surface density, but instead complex structures with complicated physics occurring. This program was a major step forward in understanding dust structures within protoplanetary disks, and many of the systems in the sample have been extensively characterized. The MAPS program [153] sought to begin developing a comprehensive survey of gas chemistry within protoplanetary disks by examining some of the most abundant molecules with ALMA. They find substructure within the gas, which suggests that each region of the protoplanetary disk may be unique, which could lead to a wide diversity in the outcomes of planet formation.

1.2.2 Planet formation in the protoplanetary disk

The conditions within the protoplanetary disk both set the stage for planet formation and are impacted by ongoing planet formation. At least some of the structures described in the DSHARP program [3] may be attributed to lane clearing by protoplanets; additional work such as [40, 91, 39] have shown forming protoplanets within disks affecting the structure within the disk. Forming planets, however, may not be the only explanation for structure within protoplanetary disks. [162] shows that gaps can form as a result of snowlines, while additional work from the DSHARP program associates some structure with pressure bumps within the protoplanetary disk.

Planet formation within the disk begins with grain growth; the smallest grains that form in the ISM can collisionally grown and aggregate within the protoplanetary disk. This process may start extremely early (as soon as 100,000 years after collapse) [68]; there may be additional grain growth that occurs in the interstellar medium that survives infall. Grains begin small enough that they are efficiently thermally and dynamically coupled to the gas and orbit with it; as grains grow, they decouple from the gas [42, 2], and begin to experience gas drag. This results in inward spiraling of the large grains, which may allow them to grow more quickly as they experience crossing orbits with smaller dust grains. Large grains additionally settle towards the midplane [16]. This pebble settling and inwards drifting results in substantial redistribution of volatiles vertically and radially [41, 32, 95, 96].

Volatile distribution is also intimately dependent on the snowline - the region where a particular volatile goes from existing in the gas phase to being bound as a solid on grains. The snowline sets the radial distribution of molecules. Where a volatile is solid, it can be incorporated into the cores of planets; where it is gaseous, it can be accreted into primary atmospheres. [52, 35] find that exterior to the water snowline, much of the ice may be inherited from the ISM; thus, the location of the water snowline may be vitally important for determining the composition of planetesimals. For planetesimals forming outside of the water ice snowline, significant primordial matter may be inherited.

In addition to setting the material (and material origin) available for accretion, snowlines can speed up pebble growth, which enhances planet formation. Beyond the snowline, the sticking efficiency may change [67], leading to enhanced formation of pebbles, while decreasing fragmentation rates [48, 194, 65] make it less likely that growing pebbles break up. This is in addition the fact that beyond the snowline, the solid material surface density increases, simply because additional materials are in solid form. The existence of a snowline also leads to pressure gradients forming within the disk; this results in a diffusive flow accross the snowline, leading to accumulation of ices [185, 32]. Lastly, snowlines can create pressure traps, leading to dust density enhancement [41]. These factors all combine to increase planet formation beyond

at least the water snowline [135, 6]. The enhancement in formation efficiency is significant - [135] finds mars-sized embryos inside the snowline while gas giant grows external to the snowline.

Of course, this entire picture is complicated by the fact that snowlines themselves are not static; the simple picture of a static disk does not fully incorporate the complex dynamics at play within the disk. First, a snowline can move as a function of stellar age [46]. As the star ages, radiation decreases, which acts to cool the disk. However, the disk mass also decreases, which increases heating efficiency, so there's a complex dependence on stellar age and disk clearing times that will affect the snowline structure within the disk. Additionally, the drifting of icy grains inwards may affect snowline location, because grain drift timescales are similar to sublimation timescales, leading to inwards motion of the snowlines [32, 163].

A detailed review of the chemistry of the major volatile species carbon, nitrogen, and oxygen within the protoplanetary disk is available in [152]. Because of the complexity of protoplanetary disks, it is important to consider as much data as is available to interpret individual systems. Individual systems can add to our understanding of the class as a whole, and help to enrich our overall understanding of protoplanetary disks.

1.3 Debris disks

Debris disks are both an outcome of planet formation, and a phenomenon distinct from planet formation. Debris disks are formed of parent planetesimal bodies that are remnants of planet formation as well as of protoplanetary disks. However, these large bodies are not detectable with current technologies. Instead, debris disks are observable due to the presence of dust. Although the majority of the mass of a debris disk is in the parent planetesimals, the majority of the surface area is in the smallest grains, due to the sheer number of them. This dust is not the same dust as is present in the protoplanetary disk. It is instead of second-generation origin, as dust grains are efficiently removed from a system through either Poynting-Robertson drag

or radiation pressure. Thus, some secondary collisional processes must be in place to replenish dust mass. We will discuss both steady-state collisional processes and stochastic events such as giant impacts that replenish dust.

The distinction between protoplanetary disks and debris disks is largely one of optical depth: whereas protoplanetary disks are optically thick in both gas and dust, debris disks are optically thin. Although the presence of optically thin dust in other stellar systems has been known since at least the 1980s, thanks to the Infrared Astronomical Satellite (IRAS), the detection of optically thin gas within debris disks is a relatively new phenomenon. While protoplanetary disks are dominated by accretionary and growth processes, debris disks are dominated by destructive processes - namely collisional grinding.

Our own solar system has a two-component debris disk: the asteroid and Kuiper belts. Both of these belts contain solid bodies remnant from planet formation, and both produce dust through collisions within the belts. The zodiacal cloud consists of both collisionally-ground dust and dust released through comet sublimation [143]. Both of our disks, however, are far below are current detection capabilities. In the past, however, the solar system debris disks may have been more massive [184, 156] and at a different location [62, 188]. To alien observers in the past, our system may have been detectable. Observations suggest that, as might be expected, the mass of a debris disk decreases with time as the parent planetesimals get depleted [134].

The overall detection rate around solar-type stars is on the order of 20% [134, 178]. It is important to note that this is not an incidence rate, as we are not able to access fainter disks; the rate of incidence is expected to be higher, as most (if not all) planetary systems are expected to have remnant planetesimals after formation. To-date, the composition of known debris disks seems to be not dissimilar to the composition of dust in our system - namely silicates [158, 133]. However, the parameter space that is explored is often limited, and where studies do not consider multibandpass characterization of dust in debris disks, compositions may be missed (see i.e. [171]).

We currently study debris disks both through spectral energy distribution (SED) excesses (see i.e. [183, 140, 45] and references therein) and imaging in both scattered

light and thermal emission (see i.e.[18, 38, 169, 7]). The concept of studying debris disks through SED excess is illustrated in Figure 1-3. SED excess is, to put it simply, excess emission when observing a star above what is expected based on the stellar blackbody curve. Excess emission arises when dust orbiting a star absorbs stellar radiation and then emits its own radiation based on its temperature and physical properties. In Figure 1-3, there are two component belts that are broad analogues to the asteroid and kuiper belts (in blue and green respectively). Their emission contribution is noted in the SED of the star. There are two additional coponents to the SED excess - the exozodiacal dust, composed of small dust grains in the interior that largely are migrating inwards from the asteroid belt, and an extended halo of small grains blown out of the system. This sample SED is for disks more massive than our own, and around a star brighter than our own. This particular illustrative SED falls into the category of two-component models; while many debris disks can be explained by a single component, others require multiple rings, as in [29, 72], while others require dust with multiple temperatures in the same radial location, as in [131].

1.3.1 Steady-state debris disks

We first discuss the canonical steady-state debris disk, which can be more fully described by [199] and references therein. As we mention above, the presence of dust in debris disks requires an origin of second generation. The very youngest debris disks may still contain remnant protoplanetary dust, but most debris disks are likely to have cleared protoplanetary dust via radiation pressure and instead must produce dust from parent planetesimals. The standard explanation for debris disks is that of a steady-state collisional cascade where large bodies collide with each other to form smaller bodies, which collide to form even smaller bodies, and so on until the blowout size of the disk is reached and the smallest particles are removed. The theoretical predictions for the particle size distribution of such a steady-state disk is $dN/da \propto a^{-3.5}$ where a is grain size [47]. Observations of debris disks find that, generally, the particle size distributions are consistent with steady-state predictions, with a few exceptions [170, 106, 133]. The blowout size that is inferred in various

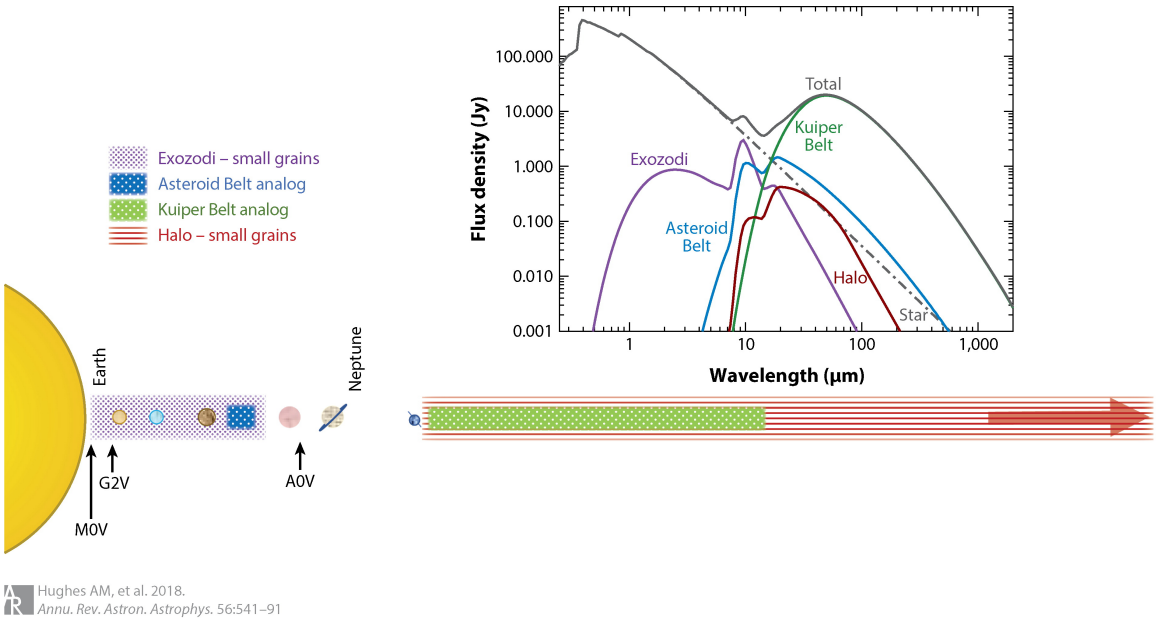

Hughes AM, et al. 2018.
Annu. Rev. Astron. Astrophys. 56:541–91

Figure 1-3: Schematic and illustrative spectral energy distribution (SED) for the components of a hypothetical Solar system analog debris disk. The system pictured is an A0V star at 7.7 pc. An asteroid belt and Kuiper belt analog are present. The exozodiacal cloud is from small grains spiraling inwards due to Poynting-Robertson drag. The halo is composed of dust grains produced in a steady-state collisional cascade that are below the blow-out size. Black arrows represent the equilibrium 150 K blackbody distance from the star for the three spectral types listed. Earth and Neptune orbits represented for a sense of scale. The SED illustrates the components of the debris disk and their contributions to the emission from the system as a whole. Image reproduced from [77].

surveys in the mid-infrared of approximately 1-20 μm is consistent with theoretical predictions [133, 75, 178, 161]. However, the mid-infrared is not as effective at tracing smaller grains as visible wavelength light is; scattered light constraints on minimum particle sizes are much weaker.

1.3.2 Giant impacts

Although many debris disks can be explained by a steady-state collisional cascade ([199] and references therein), some require singular stochastic events to explain the dust. Stochasticity may take the form of giant impacts, which are expected to be common in planetary systems between 10 and 100 Myr after collapse.

Within the solar system, there is abundant evidence of giant impacts. All four of the terrestrial planets have signatures of catastrophic collisions. In the case of Mercury, its unusual iron enrichment [13, 28] is suggestive of a giant impact that left behind a dense core. Venus has retrograde rotation, which is hypothesized to have occurred as a result of a catastrophic impact [44]. The formation of the Moon [22, 23, 125] is thought to have been a consequence of a collision between a proto-Earth and a Mars-sized impactor. Lastly, the Martian hemispheric dichotomy [117, 148] has been attributed to being a giant impact basin. Such catastrophic collisions produce large amounts of debris that should, in theory, be observable. Even smaller collisions are visible within the solar system zodiacal cloud [142]. Work such as [199, 80] also indicate that giant impact debris should be observable in exo-systems. To-date, however, there is limited evidence for giant impacts elsewhere. For the most well-characterized system with evidence of giant impacts, see Chapter 4. The lack of evidence does not imply, however, that giant impacts do not occur.

In some scenarios, giant impacts or other stochastic events may set into motion a steady-state collisional cascade. In the case of giant impacts, this will occur on the symmetrization timescale, as described in [205]. As time post-impact increases, the debris produced in the aftermath of the impact will circularize, which can result in a disk that is morphologically identical to a debris disk. Some disks we see may be, at least in part, remnants of giant impact debris.

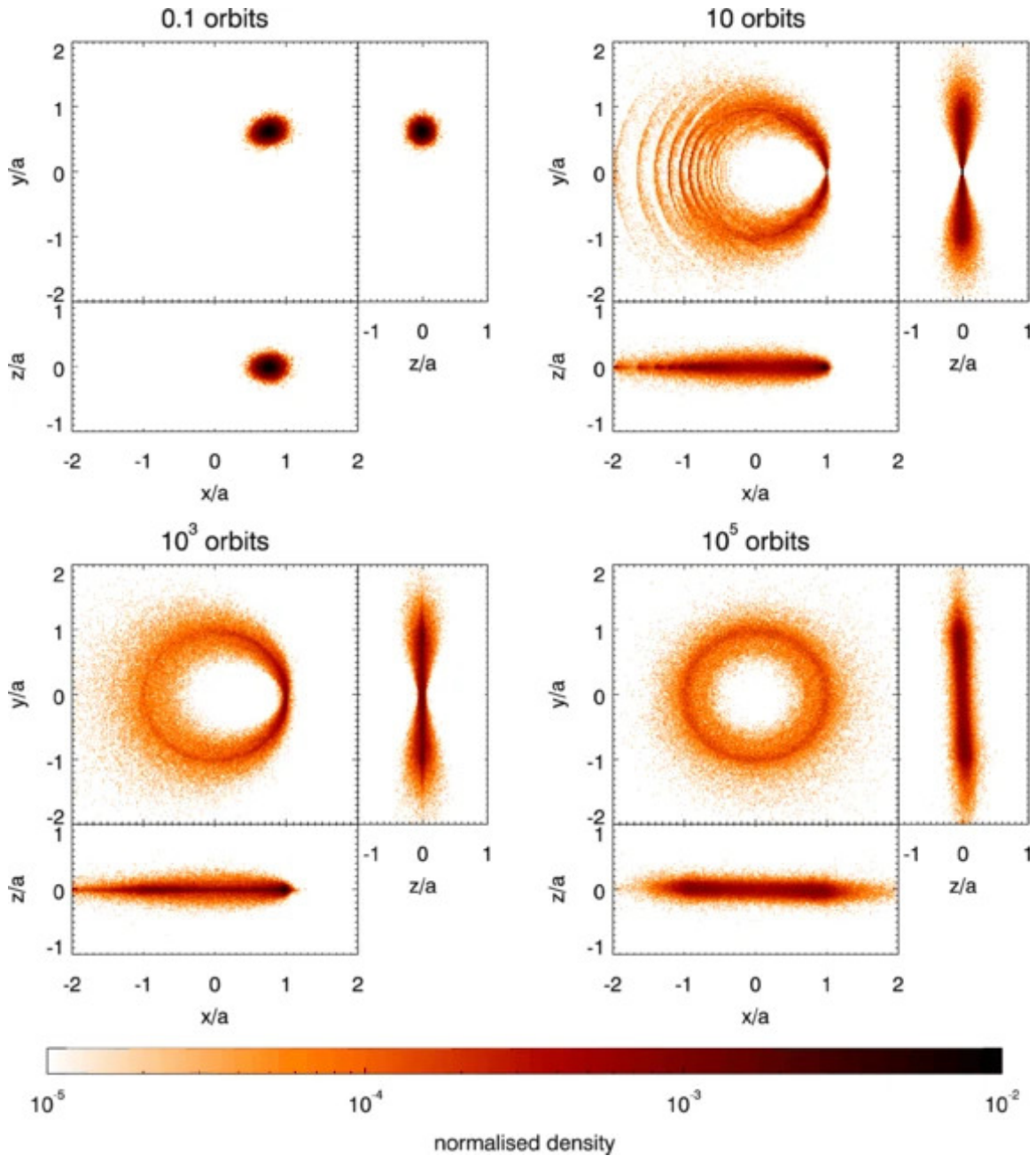

Figure 1-4: Snapshots of the evolution of debris ejected in giant impacts as a function of time. Image reproduced from [205].

1.4 Focus of the thesis

In this thesis, we discuss methodologies to understanding planetary system histories by looking at the components of circumstellar disks. The work is united by a desire to better understand how planets initially accrete their atmospheres, and how those atmospheres evolve over time. This thesis brings together experimental, observational, and modeling studies of both gas and dust, which provides for a holistic view of the atmospheric history of planetary bodies.

In Chapters 2 and 3 we discuss experimental techniques for determining the desorption kinetics and entrapment of neon, argon, krypton, and xenon. These methods allow us to understand the gas-phase and solid distribution of nobles in protoplanetary disks, and to probe to what level these elements can be used as tracers of nebular gas accretion or delivery via icy bodies to the atmospheres of nascent planets. The physical entrapment mechanisms explored for the noble elements in these chapters are novel measurements to examining noble gas abundances within the solar system; prior work has often focused on the theory of chemical entrapment mechanisms such as clathration. The experimental determination here provides a plausible mechanism for noble gas delivery to planetary atmospheres.

In Chapter 4, we discuss observations of the HD 172555 system via the Atacama Large Millimeter Array (ALMA) telescope. In this system, we have detected - for the first time - the remnants of an atmosphere stripped from a protoplanet during a giant impact. We find that a holistic understanding of the gas and dust in the system is necessary to rule out other origins for circumstellar debris. Previous attempts to understand atmospheric stripping in the aftermath of a giant impact have been theoretical in nature [173, 14]. Further, most searches for giant impact candidates have looked for abnormal dust signatures within debris disks. In contrast, we present observational evidence for a giant impact by examining both the abnormal dust in the HD 172555 system as well as the presence of carbon monoxide gas.

In Chapter 5, we simulate dust spectra for nine highly-inclined debris systems in advance of data from the James Webb Space Telescope (JWST); constraints from

JWST on the spectra of these disks will yield information about dominant dust compositions and particle size distributions, providing insights into the formation histories of the parent planetesimals in these systems. The simulated spectra encompass the bandpasses of the Hubble Space Telescope (HST), JWST, and ALMA. This approach to characterizing dust spectra stands in contrast to much of dust modelling, which often relies on data points in either scattered or thermal emission. As we show, the limited approach is not sufficient to characterizing dust compositions.

Chapter 2

Experimental determination of the desorption binding energies and entrapment efficiencies of Argon, Krypton, and Xenon in water ice

The present-day concentrations of noble gases in comets, planets, and other Solar System objects depend on the distribution of noble gases in the Solar protoplanetary disk. The location of noble gas snowlines determines the concentration of noble gases accreting into the atmospheres of nascent planets as well as the abundance of noble gas solids in reservoir bodies such as comets that deliver volatiles to planets. The binding energies of noble gases to water ice informs the snowline location, while the noble gas content of reservoir bodies can be enhanced by efficient trapping. We have measured both the multilayer and sub-monolayer binding energies of argon (846,1120 K), krypton (1192,1440 K), and xenon (1558,2000 K) on amorphous solid water. We have additionally measured the entrapment efficiencies of these species, finding expected dependencies on both ice thickness and ice mixing ratios. Yet in astrophysically relevant ice analogs ($\geq$ 50:1 ratio), trapping efficiency always exceeds 60%. We use a static disk model to present a simple picture of the distribution of ice-phase

and gas-phase abundances of all three noble gases in the Solar Nebula. These values place the snowline locations at $\sim$ 37, 24, and 14 au, respectively, which means that only comets forming close to the Kuiper belt would be rich in all three noble gases. However, the measured high entrapment efficiencies imply that comets assembling at any distance beyond the water snowline may have preserved a substantial noble gas reservoir, and potentially delivered it to terrestrial planets.

2.1 Introduction

Solar system objects such as asteroids, comets, and planets formed in the Solar nebula. Understanding the present-day composition of such astrophysical objects requires a knowledge of the distribution of solid and gaseous material within the protoplanetary disk, which in its turn formed through gravitational collapse of the natal molecular cloud [197]. The molecular cloud is expected to contain $\sim$99% molecular hydrogen and helium and $\sim$1% gas-phase volatiles and solid dust grains. Dust acts as a site for both chemistry and ice deposition; water ice may form from atomic hydrogen and oxygen directly on the grains [189, 76]; other ice constituents form similarly or freeze out on the grains from the gas phase directly. The noble gases are among the species that freeze out onto grains. These processes result in composite amorphous ice structures. When gravitational collapse is triggered, material begins to fall in towards the star, forming a disk so as to preserve angular momentum. As material descends towards the midplane, it passes through a shock front and is heated - the degree to which depends on the radial distance from the star [19]. [193] find that grains are sufficiently heated so that water ice desorbs in the inner 10 au of the disk. As the nebula cools, some of the sublimated ices may reform, probably as layered ices due to sequential freeze-out of increasingly volatile species.

In the disk, the distribution of volatiles in the gas and solid phase sets the composition of dust grains and icy materials that are the building blocks of larger planetesimals, which in turn may become planetary cores. Icy grains within disks may migrate inwards as they grow and decouple from protoplanetary disk gas [3, 141],

allowing forming planets to accrete ices enriched in volatiles. These forming cores can accrete and retain gas-phase volatiles if they grow massive enough before disk gas dispersal [27]. Comets and other icy bodies, forming from the initial ice/dust, may deliver additional volatile material to planetary atmospheres after formation.

As such, condensation fronts/snowlines - boundaries where the majority of a volatile goes from vapor to solid phase - govern the composition of forming planets and their atmospheres [154]. The location of snowlines can also enhance planet formation efficiency [31, 82, 66, 172]. As desorption kinetics set the location of the snowlines, quantifiying desorption energies is key to understanding the compositions of planetary bodies.

Desorption energies are not the only ice characteristics that set the distribution of gaseous and solid species in disks. Species may become trapped in matrices of other ices. Their entrapment in pores of a less-volatile ice allows them to persist in solid bodies until the less-volatile ice either restructures or desorbs. The process of entrapment allows material to persist interior to its snowline. Entrapped volatiles surviving the infall phase may also affect planetary composition; they can both alter the amount of gaseous volatile available for direct accretion into an atmosphere by sequestering volatiles in ices, and enhance final concentrations by delivering volatiles to existing atmospheres. Characterizing the efficiency of entrapment can enhance the understanding of the compositions of planets and the bodies responsible for volatile delivery.

Noble gases in particular are useful as tracers of volatile delivery within disks. While the distribution of molecules or other elements requires an inventory of chemical interactions, the distribution of noble gases is tied entirely to desorption and entrapment behavior, as well as any migration of material within the disk. The inertness of the noble gases, which allows us to neglect chemical interactions, simultaneously makes it difficult to observe them outside the solar system. However, HeH^+ [145], ArH^+ [81], krypton [25], and xenon [159] have been observed within the interstellar medium or planetary nebulae. These noble gases have not been measured in protoplanetary disks. Within the solar system, volatile delivery to bodies such as

Jupiter, Titan, and the Earth can be explored through the lens of the noble gases.

These solar system objects have been subject to in-situ analysis, enabling noble gas measurements. The Galileo Probe Mass Spectrometer found that the abundances relative to hydrogen for argon, krypton, and xenon in the Jovian atmosphere were 2.5±0.5, 2.7±0.5, and 2.6±0.5 times the solar ratios, respectively. The uniform enhancement in these noble gases suggests that the environment Jupiter formed in must have had abundant noble gas present, in addition to delivery of solid noble gas to either the core or atmosphere.

In the case of Titan, the Gas Chromatograph Mass Spectrometer aboard the Huygens probe detected small amounts of atmospheric argon and neon [146], and provided upper limits on the abundance of krypton and xenon. The scientific community has not reached consensus on the method of acquisition of noble gases by Titan, with the gravitational capture of nebular gases [60], delivery via ices [139], and delivery by rock considered [190]. The depletion of atmospheric noble gas species has been posited to occur via sequestration in surface clathrates [138], condensation via liquid hydrocarbons [73], or trapping in a liquid water ocean [190]. Additional in-situ data, paired with laboratory measurements of noble gas behavior in water ices, are required to make sense of Titan's noble gas history.

Naturally, measurements of noble gases in Earth's atmosphere are abundant; it is possible that a significant fraction of Earth's atmospheric argon, krypton and xenon were delivered through cometary impacts. Although previous work has suggested that the overall volatile composition of the ocean-atmosphere system came from chondritic rather than cometary sources [122, 123], some cometary contribution is required to explain the noble gas component of the atmosphere. The relative contributions of chondritic and cometary bodies to the noble gas abundance in Earth's atmosphere is dependent on the trapping efficiency of noble gases in cometary bodies. Through preliminary analysis of the coma of comet 67P/Churyumov-Gerasimenko with the Rosetta mission, [124] finds that comets are an important source for atmospheric noble gases. Further data on the isotopic fractionation in the coma revealed that xenon in the Earth's atmosphere is 22±5% cometary in origin [121], assuming that

67P has a typical cometary composition. They further found that the cometary xenon is primordial, lending support to the idea that at least some primordial composite ices survive gravitational collapse.

Interpreting the partition of noble gases seen in the solar system requires an understanding of desorption kinetics and entrapment efficiencies of noble gases in astrophysically relevant ices. Temperature programmed desorption (TPD) is a labaratory technique used to measure these quantities. These experiments measure the rate of desorption of a species from a substrate as a function of temperature of the substrate. In a solar nebula setting, the relevant substrate is amorphous water ice. Entrapment efficiency can be probed by comparing the amount of atom or molecule that desorbs around its typical desorption temperature with the total amount desorbing.

There is existing theoretical [33] and experimental work [181, 9, 150, 10, 151] examining both the desorption and entrapment of noble gases. Previous work has been done to measure the desorption kinetics of noble gases. In [181], the multilayer desorption kinetics from graphene and the monolayer desorption kinetics from ASW are measured for argon, krypton, and xenon. The zeroth order desorption energies from graphene for argon, krypton, and xenon are determined to be 7.5 (902), 11.2 (1347), and 14.6 (1756) kJ mol^{-1} (K), respectively. The desorption binding energies of argon, krypton, and xenon from ASW are found to be 7.2 (866), 11.4 (1370), and 16.3 (1961) kJ mol^{-1} (K), respectively.

Some work has also been done to understand entrapment of noble gases. [9] investigate the effect of porosity on trapping a number of volatiles, including Ar. They find that argon is not trapped when deposited on top of dense amorphous water ice, inefficiently trapped when deposited on top of porous amorphous water ice, efficiently trapped (65%) under porous amorphous water ice, and completely trapped under dense amorphous water ice. [150] studied 1:1 mixtures of H_2O:Ar. Their TPD curves appear to suggest that $\sim$50% of initially present argon is trapped in 0.1 and 5 μm thick ice layers. [10] investigate the relative trapping efficiencies of Ar, CO, and N_2 in water ice, but do not investigate the trapping efficiency of the individual species. They do find, however, that CO is trapped with a higher efficiency than

N_2 and the same efficiency as Ar. This suggests that even in mixtures of volatiles, argon may be efficiently trapped. There are no studies on the entrapment efficiencies of krypton or xenon in ices of interstellar relevance, although [151] do investigate isotopic enrichments in entrapped argon, krypton, and xenon.

In this work, we explore the desorption binding energies and entrapment efficiencies of argon, krypton and xenon in amorphous water ices in a laboratory setting. We replicate and expand on previous experiments on noble gas desorption and then quantify the efficiency of noble gas entrapment in astrophysical analogs as a function of composition and ice thickness. In section 2.2, the experimental setup is presented. The experimental results are given in section 2.3. The results and their astrophysical implications are discussed in section 2.4.

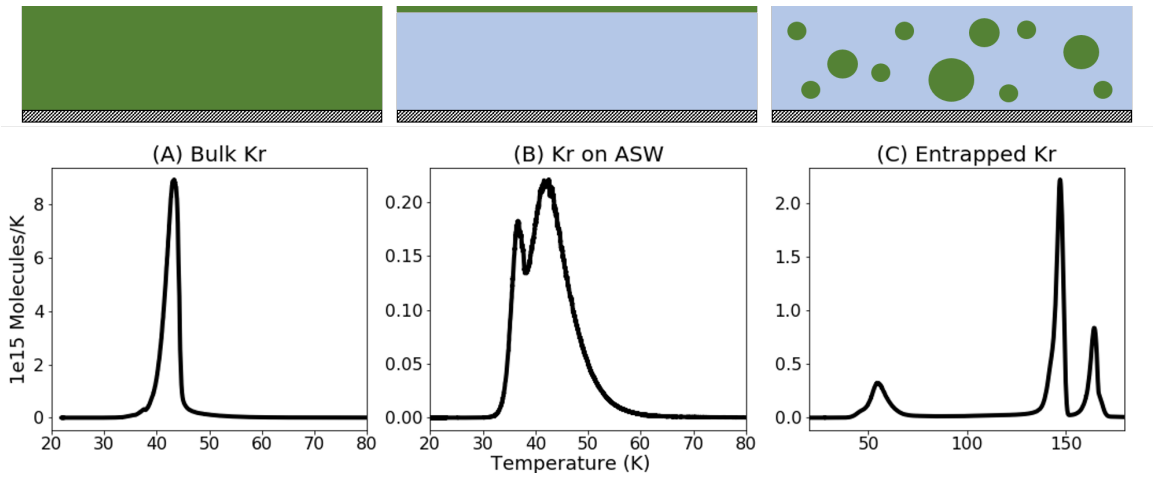

Figure 2-1: Three experimental desorption schemes. (A) Several monolayers of a noble gas are deposited onto a substrate and desorbed to measure the desorption binding energy of a noble gas to itself. (B) A submonolayer to monolayer of noble gas is deposited onto $\geq$20 ML amorphous solid water ice and desorbed to measure the noble gas to water desorption binding energy. The left peak is related to the zeroth order desorption binding energy while the right peak arises from first order desorption. (C) A mixture of noble gas and water is deposited onto a substrate and desorbed. The left peak is associated with noble gas desorption, the middle peak is the release of noble gas during water ice restructuring, and the right peak is the release of noble gas due to desorption of water.

2.2 Methods

We derive the desorption energies of argon (Ar), krypton (Kr), and xenon (Xe) ices from compact amorphous solid water (ASW) ice through temperature programmed desorption (TPD) experiments. They are also used to measure the entrapment efficiencies of the same species in porous ASW. Figure 2-1 illustrates the three kinds of experiments we carried out to characterize monolayer desorption, multilayer desorption, and entrapment. Multilayer (zeroth order) desorptions probe the desorption biding energies of an atom or molecule to itself. We measure this desorption energy by depositing several monolayers of noble gas onto a substrate and desorbing at a constant rate. Zeroth order curves are characterized by common leading edges and a lack of coverage dependence. Submonolayer desorptions (first order) probe desorption binding energies to a substrate, in this case amorphous solid water (ASW). We deposit submonolayer thicknesses of noble gas onto ASW and desorbing. Entrapment efficiencies are measured by characterizing the fraction of noble gases desorbing with water from water and noble gas ice mixtures. All experiments are carried out on a custom-made experimental setup designed for ice experiments; the instrument is described in detail by Simon et al. (in prep), and summarized below.

2.2.1 Experimental Setup

The experiments were carried out in a laboratory setup (Figure 2-2) designed to investigate thermal processing of interstellar ice analogs. This setup is a miniaturized version of the experimental chamber described in [100], has been previously introduced in [179], and will be fully described in an upcoming paper (Simon et al., in prep). This setup consists of a 6.5" ID ultra-high vacuum (UHV) stainless steel chamber (custom-made, Kimball Physics) with a base pressure of 4×10^{-9} Torr at room temperature. The chamber is evacuated using a turbomolecular pump (Pfeiffer HiPace®400 with pump speed of 350 l/s for N_2) backed by a Kashiyama NeoDry 15E dry pump with a maximum pumping speed of 250 l/min. Chamber pressure is monitored by a MKS series 999 Quattro multi-sensor vacuum transducer coupled

with a series PDR900 single channel controller, providing continuous measurement from atmosphere to 10^{-10} Torr.

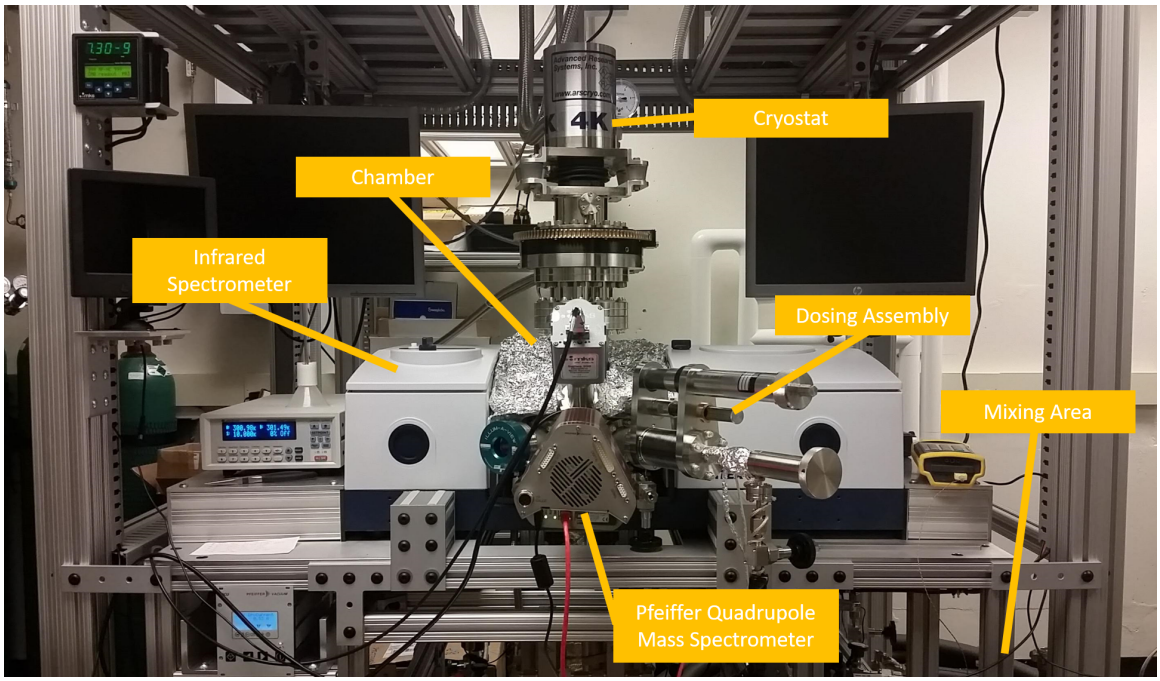

Figure 2-2: Photo of the chamber, with the main experimental instrumentation marked

The UHV chamber is inside the sample compartment of a Bruker Vertex 70 FTIR spectrometer. The IR spectrometer and UHV chamber are placed on separate solid frames equipped with vibration isolation slides such that the optical path of the IR instrument is aligned with the horizontal axis of the chamber in the transmission geometry as shown in Figure 2-2. The UHV chamber is separated from the IR spectrometer by two differentially pumped IR transparent KBr windows. The entire optical path of the IR spectrometer is continuously purged with dry and CO/CO_2 free air using a Parker 75-62 Purge Gas Generator.

The UHV chamber houses an IR transparent 2 mm thick CsI window (0.75" clear view) mounted on an optical ring sample holder attached to a closed cycle helium cryostat (Advanced Research Systems model DE-204S). The cyrostat is integrated with a DMX-20B interface which decouples and vibrationally isolates the CsI window from the cold head of the cryocooler with helium exchange gas. A differentially pumped rotary seal (Thermionics RNN-400) on the cryostat assembly allows for 360°

rotation of the sample mount.

A nickel plated oxygen-free high conductivity (OFHC) copper radiation shield is attached to the first stage of the cryostat, enabling the CsI substrate to reach base temperatures of 11K. Temperature is controlled between 11K and 350K with $\pm$0.1K precision by a 75W resistive heater and calibrated Si diode sensor (LS-670B-SD) located on the cryocooler tip near the heater using a Lakeshore Model 335 temperature controller. A second Si diode sensor is mounted directly to the CsI substrate to measure ice temperature.

Ices are grown in situ by exposing the cold CsI substrate to a constant flow of gas from an independently pumped gas line. A 4.8 mm ID stainless steel deposition tube is attached to a VAT variable leak valve and compact z stage (MDC Vacuum Products) to enable directed vapor deposition. The independent gas line is used to store gases and prepare gas mixtures before delivery to the chamber. It is pumped down to pressures $< 5 \times 10^{-4}$ Torr using a turbopump station (Pfeiffer Vacuum HiCube Eco) with pump speed of 67 l/s for N_2. The gasline pressure is monitored with two active capacitance transmitters (Pfeiffer) CMR 361 and CMR 365 in the overall range $5 \times 10^{-4} - 1100$ Torr.

Water ice thicknesses are quantified by employing IR spectroscopy between 4000-400 cm^{-1}. Spectra are recorded using a liquid N_2 cooled Mercury Cadmium Telluride detector with a resolution of 1 cm^{-1} and averaged over 128 scans with an aperture setting of 1mm. Background spectra are recorded before each ice deposition and subtracted from the respective ice spectra.

Monitoring of gas composition during both ice growth and desorption is achieved with a Pfeiffer quadrupole mass spectrometer (QMS) (QMG 220M2, mass range 1-200 amu, and resolution of 0.5 amu). The QMS signal is proportional to the number of desorbed molecules.

2.2.2 Changes in setup between 2018 and 2021

Approximately two-thirds of the data were taken prior to 2020, and one third of the data were taken after. Between the two sets of measurements, a couple of changes

to the chamber were made. In 2018, an aperture was located in front of the QMS in the chamber to enable more directed measurements of gases. A chamber pump has also been exchanged, although this has not substantially altered the base pressures achieved. Lastly, the tip of the cryostat/sample holder has been adjusted, which has enabled the base temperature of the chamber to go from 17 K in 2018 to 11 K in 2021.

2.2.3 Experimental Procedure

The experiments described below use deionized water purified through several LN_2 freeze-pump thaw cycles. Experiments additionally use ^{40}Ar, ^{84}Kr, and ^{129}Xe (all 99.95% purity, Sigma-aldrich).

Binding Energies

To measure multilayer (zeroth-order) desorption kinetics, between ∼10 ML and ∼40 ML of noble gas are deposited onto the CsI substrate below 15 K at a rate of ∼2 ML min^{-1}. Ices are heated at a constant rate of 1 K $minute^{-1}$ to 200 K. The desorbing species are monitored with the QMS; the QMS signal and molecular desorption rate per Kelvin are related via a scaling factor (see below).

To measure monolayer (first-order) desorption kinetics, ≥20 ML of DI water are deposited onto the CsI substrate at 100 K over the course of 10 minutes. Deposition at 100 K ensures an amorphous, compact water ice structure analogous to water ice that would freeze out onto cooling interplanetary grains. The substrate is then cooled to between 10 and 17 K and submonolayer to monolayer (ML) coverages of noble gases are deposited at a rate of ∼0.1 ML min^{-2}. Following deposition, ices are heated at a constant rate of 1 K $minute^{-1}$ to 200 K. The noble gas ice thickness is estimated after deposition; we set the conversion factor for 1 ML to correspond to the integrated TPD signal for a curve where the multilayer peak begins to disappear, see Figure 2-4. These conversion factors are then applied to the multilayer experiments to determine the thickness of the multilayer depositions.

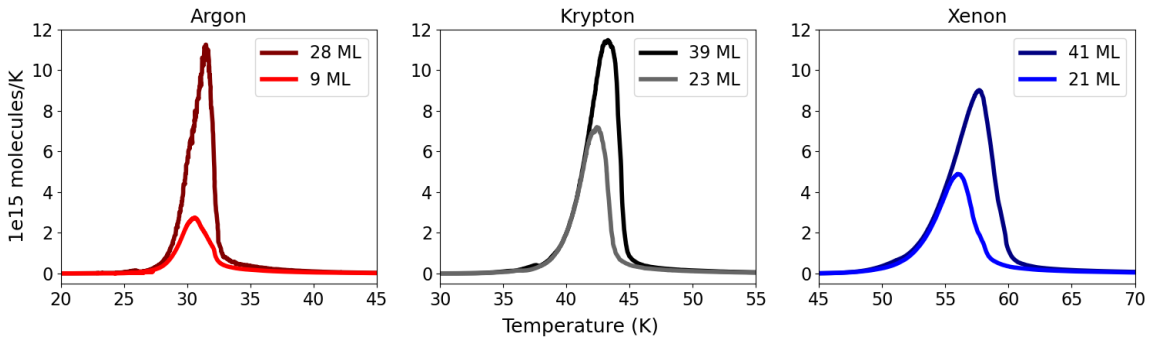

Figure 2-3: Temperature programmed desorptions for multilayer depositions of argon, krypton, and xenon. The maximum desorption rate shifts towards higher temperatures with increasing ice thickness, as expected from a zeroth order desorption. In addition, the leading edge of the desorption for each ice thickness is aligned, a further signal that we are in the zeroth-order regime.

Entrapment Efficiencies

For the entrapment experiments, mixtures of DI water and noble gases in the range between ∼5:1 and ∼100:1 ratios are first prepared in the gas line. Approximately 20 torr of water vapor is released into the fixed volume of the mixing area. This amount of water vapor is then condensed into a vacuum flask attached to the mixing area and submerged in liquid nitrogen (LN2). This freezing cycle is repeated until ∼50 torr of water have been condensed into the vacuum flask. Between 1 and 5 torr of noble gas is then condensed into the vacuum flask, depending on the intended ratio of the mixture. The vacuum flask is then closed off from the mixing area and let to sit overnight to ensure proper mixing between the components. The following day, the mixtures are deposited at 11 K onto a CsI window. Deposition of water at 11 K ensures a water ice structure analagous to water ice that would form through grain-surface chemistry in the ISM [59]. Depositions are monitored with both the QMS and IR spectrometer described earlier. Ice thicknesses are varied between ∼15 and ∼200 ML, with deposition rates of ∼10 ML min^{-1}. After deposition, ices are heated at a constant rate of 1 K minute^{-1} to 200 K. The desorbing species are monitored with the QMS.

2.2.4 Calibration of the QMS signal

To determine the ratio of noble gas to water in the entrapment experiments, a mixture of methods is used. Approximately two-thirds of the data were taken prior to 2020, and the other third were taken after. In both cases, the amount of water ice deposited is determined through use of the IR spectrometer in the laboratory setup. For data taken prior to 2020, the amount of noble gas present in the ice is determined by comparison to the monolayer experiments as described above. A conversion factor of QMS ion current to number of molecules is established through the monolayer desorption experiments, as in e.g. [12, 56].

In the case of data taken after 2020, the amount of noble gas present is determined through the method described in [119]. This method relies on both a comparison to an infrared-active species (in the case of these experiments, ^{13}CO is used), and the realization that the integrated ion current measured by a QMS corresponding to a mass fragment m/z during a TPD is proportional to the total number of molecules desorbed. The relation of the integrated ion current of a noble gas during a TPD to the number of molecules desorbed during that TPD is expressed as:

$$A(m/z) = k_{CO} \times \frac{\sigma^+(mol)}{\sigma^+(CO)} \times N(mol) \times \frac{I_F(mol)}{I_F(CO^+)} \times \frac{F_F(mol)}{F_F(CO)} \times \frac{S(m/z)}{S(29)} \tag{2.1}$$

where $A(m/z)$ is the integrated ion current of a given mass fragment (m/z) during desorption, $\sigma^+(mol)$ is the ionization cross section for the first ionization of the species at the incident electron energy of the mass spectrometer (70 eV), $N(mol)$ is the total thickness of the noble gas deposited, $I_F(mol)$ is the ionization fraction of a noble gas with charge z, $F_F(mol)$ is the mass fractionation of a species of interest (definitionally $F_F(mol) = 1$ in the case of a noble gas), $S(m/z)$ is the sensitivity of the QMS to a mass fragment (m/z), and

$$k_{CO} = \frac{A(29)}{N(CO)} \tag{2.2}$$

is the proportionality constant that links the integrated ion current $A(29)$ of CO to the thickness of CO measured with the IR spectrometer $N(CO)$. The proportionality

Table 2.1: Summary of the calibration parameters

Species	m/z	$\sigma^+(mol)^*$	$I_F(mol)^{**}$	$S(m/z)^{**}$
Ne	20	4.75×10^{-17}	0.9852	3.86×10^{14}
^{13}CO	29	2.52×10^{-16}	1.0000	3.14×10^{14}
Ar	40	2.52×10^{-16}	0.8424	2.47×10^{14}
Kr	84	3.45×10^{-16}	0.7191	9.63×10^{14}
Xe	129	4.67×10^{-16}	0.6212	4.95×10^{13}

* [168]

** Experimentally measured for this setup

constant k_{CO} for this experimental setup has been measured and described in an upcoming paper (Simon et al., in prep). The values used in this relation are reported in Table 2.1.

The CO proportionality constant is used in the post-2021 data as the removal of the aperture in the chamber setup has made it more difficult to acquire high-quality sub-monolayer data for xenon. For both argon and krypton, both methods for QMS signal calibration can be used. We find that there is a consistent factor of 3 between the resulting amount of noble gas present. Specifically, the amount of noble gas present as determined from the [56] method is three times lower than the amount of noble gas present as determined by the [119] method. This is likely due to the fact that the [56] method does not account for any pooling by noble gas on the ASW surface. Due to the consistency in the factor of three, all of the noble gas contents determined with the [56] method are adjusted upwards by a factor of three in Figure 2-6 for clarity of comparison. The values are not updated in the tables, and instead reflect which method was used to determine the ratios.

The sensitivity of the QMS to a mass fragment (m/z), $S(m/z)$ has been determined for this experimental setup. The QMS ion current in response to a mass fragment (m/z), $I(m/z)$, is related to the sensitivity of the instrument via

$$I(m/z) = k^*_{QMS} \times \sigma^+(mol) \times P(mol) \times I_{S_F}(m) \times I_F(z) \times F_F(m) \times S(m/z) \quad (2.3)$$

The new factors are k^*_{QMS}, a proportionality constant that is the same for different species in the chamber, $P(mol)$, the pressure measured in the chamber, and I_{S_F}, an

isotopic factor. The pressure gauge in the chamber does not discriminate between different isotopologs of the same species while the QMS does; the factor reflects the amount of gas that is actually measured by the QMS. The pressure additionally needs to be corrected by gas correction factors provided by the gauge manufacturer.

With this relation, $S(m/z)$ can be measured for each noble gas by introducing the noble gas into the chamber and measuring both the pressure and QMS signal at a range of pressures. With this, an average sensitivity $S(m/z)$ can be derived. We measure $S(m/z)$ for neon, argon, krypton, and xenon. An exponential fit leads to a sensitivity curve of

$$S(m/z) = \left(5.94e^{-0.025(m/z)} + 0.24\right) \times 10^{14} \tag{2.4}$$

This is an empirical relation between (m/z) and $S(m/z)$ that can be used to determine the sensitivity for any mass in the chamber.

2.3 Results

We first present the multilayer (zeroth order) and monolayer (first order) desorption binding energies of argon, krypton, and xenon. We then present the results of entrapment experiments in porous ASW.

2.3.1 Binding Energies

To quantify desorption energies, we fit the TPD curves with the Polanyi-Wigner equation:

$$-\frac{d\theta}{dT} = \frac{\nu}{\beta}\ \theta^n\ \mathrm{e}^{-E_{des}/T} \tag{2.5}$$

where θ is the ice coverage, T is the temperature in K, ν is a pre-exponential factor in s^{-1}, β is the heating rate in K s^{-1}, n is the desorption order, and E_{des} is the desorption energy in K. The pre-exponential factor is derived from a harmonic oscillator relation

	Argon		Krypton		Xenon	
Type	ML	E_{des} (K)	ML	E_{des} (K)	ML	E_{des} (K)
Pure Ice	27	845^{120}_{110}	38	1160^{115}_{110}	41	1360 ± 100
Pure Ice	9	875^{125}_{120}	23	1180^{190}_{60}	21	1530 ± 115
H_2O (compact)	1.3	1150[185]	1.6	1430[150]	1.6	1940[210]
H_2O (compact)	1.0	1165[175]	1.3	1440[145]	0.8	1995[210]
H_2O (compact)	0.5	1210[200]	0.7	1470[145]	0.4	2040[220]

Table 2.2: Coverages, Desorption energy with uncertainty for the pure ice multilayer regime or mean desorption with FWHM for the submonolayer regime on ASW. The bracketed values for the first order desorptions represent the standard deviation of the spread in energies, rather than the uncertainty.

(see [70], [1], and [149]):

$$\nu = \sqrt{\frac{2n_s E_{des}}{\pi^2 m}} \tag{2.6}$$

where n_s is the number of adsorption sites ($\sim 10^{19}$ sites m^{-2}) and m is the mass of the molecule in kg. This is valid in the case of small molecules, as it relies on internal and translational degrees of freedom.

The TPD curves of multilayer depositions of argon, krypton, and xenon on the CsI substrate are shown in Figure 2-3. The shape of the TPD curves is consistent with a zeroth order desorption, where the leading edges of the curves align [132]. The desorption energies can be determined by fitting the zeroth-order Polyani-Wigner equation (Equation 2.5) to the curves in the regime well-described by exponential behavior. We left both ν and E_{des} as free parameters in the fit. There is an $\sim$10% uncertainty in the measurement, arising from uncertainties in the temperature calibration. The uncertainty was estimated by fitting curves shifted by $\pm$2K. The binding energies and uncertainties are given in Table 2.2. We find binding energies of 875, 1180, and 1530 K for argon, krypton, and xenon, respectively.

TPD curves for submonolayer and monolayer depositions of argon, krypton, and xenon on compact ASW are shown in the left panel of Figure 2-4. The TPD curves exhibit first order desorption behavior. The first peak corresponds to isolated pools of noble gas desorbing from itself. The second peak corresponds to first order desorption kinetics from the ASW substrate.

The first order desorption peak, related to the desorption of noble gas from the

ASW substrate, is described with a distribution of desorption energies. This is because the desorption is occurring from a disordered and rough substrate, as reported by [149], [36], [49], and [56], using models based on work by [167], [92], and [187]. To derive desorption energies for the submonolayer regime, we used a distribution of binding energies. We fit the submonolayer regime of the TPD curves (second peak) by a linear combination of first-order kinetics as described in [56], sampling the desorption energy in steps of 50 K for argon and krypton and steps of 60 K for xenon. For argon, we sampled between 500 and 2000 K, for krypton between 1000 and 2000 K, and for xenon between 1300 and 1800 K. Fitting is done in python with scipy.optimize.nnls, a non-negative least-squares module. The linear combination coefficients are normalized to the initial coverages, yielding fractional coverages. The data are smoothed using a Gaussian filter and plotted in dashed lines for clarity as well. The right panel of Figure 2-4 displays the results of the binding energy fitting algorithm. The desorption energies are coverage dependent, as seen in [56, 149]. As the coverage decreases, the binding energy increases; it is possible that the noble gases adsorb to the strongest binding sites on the water substrate first, and are therefore also the last to desorb.

2.3.2 Entrapment Efficiencies

The entrapment efficiency is computed as a ratio of the integrated noble gas desorption from 100-200 K to the total integrated noble gas desorption. This effectively computes the ratio of gas that is released during ASW restructuring and ASW desorption to the total deposited gas. This interval is chosen as it begins above the tail end of xenon monolayer desorption (< 70K) and before water ice restructuring (> 120K).

Figure 2-5 shows that entrapment efficiencies are somewhat sensitive to the kind of entrapped gas, ice thickness, and ice mixing ratio. The curves shown are normalized to the maximum desorption rate in a given experiment, and offset for clarity. The first desorption peak corresponds to the desorption of noble gas at its typical binding energy to water. The second desorption peak corresponds to the release of noble gas from water ice as a consequence of water ice restructuring from an amorphous

to crystalline phase [104]. In the left panel, the desorption curves of comparable experiments for each noble gas are presented. The most apparent variation is that the relative importance of the escaping gas decreases with increasing noble gas mass. The middle panel shows argon desorption from water:argon ∼(30-42):1 mixtures, which show negligible changes in entrapment behavior with increasing ice thicknesses. The right panel displays a series of xenon experiments with approximately the same thickness (∼33-43 ML) and increasing ice mixing ratios. In this series of experiments, the entrapment fraction increases when the ratio increases from 30 to 86, but not when further increasing the ratio to 130. The precise values for the selected experiments are presented in Table 2.3. In summary, this selection of experiments indicate that entrapment fractions are sensitive to the entrapped species and to mixing ratio, but quite insensitive to the ice thickness beyond 50 ML. We next evaluate this trend using our complete set of experiments.

We performed 34 experiments, which ranged in ice thickness from 28 to 232 ML, and in ice mixing ratios from 2.5 to 266. While there is overlap in the conditions used for each noble gas, they each cover a somewhat different parameter space. We therefore summarize the results of the experiments with ice mixing ratio greater than 5 in Figure 2-6; All experiments are listed in Table 2.4. Two argon experiments with lower ratios (20220323-1 and 20220324-1) were performed for calibration, but not included in Figure 2-6. Each panel in Fig. 2-6 represents the results from all experiments performed for a given noble gas. The trends we saw in the selection of experiments above are generally confirmed when inspecting Fig. 2-6: as the ratio of water to noble gas increases, the entrapment efficiency also increases. There does seem to be an additional trend in that the heavier the noble gas, the more efficient the trapping. Overall, the experiments suggest that in astrophysically relevant conditions, noble gases are efficiently trapped in amorphous water ice.

2.3.3 Uncertainties

The uncertainties for both the multilayer and monolayer desorption binding energies are systematic rather than statistical in nature. The uncertainties in the multilayer

Table 2.3: Selected entrapment efficiency experiments

Species	Ratio	ML Water	ML NG	Entrapment (%)
Ar	40	47	1.2	58
Kr	50	53	2.3	76
Xe	86	43	0.5	78
Ar	40	47	1.2	58
Ar	42	113	2.7	60
Ar	30	239	7.9	58
Xe	30	33	1.1	46
Xe	86	43	0.5	78
Xe	130	33	0.3	75

*2018 experiments; ratios determined with same method

desorption binding energies are primarily driven by uncertainties in the temperature calibration, as there is a slight discrepancy between the measured temperature and the actual temperature on the substrate. The uncertainty can be estimated by fitting curves that are offset with respect to the chosen temperature. This results in uncertainties of approximately 10%. The temperature uncertainty is valid in the case of the sub-monolayer desorption binding energy as well, and is approximately 10% of the central desorption energy value listed in Table 2.2. However, there is an additional spread in the monolayer desorption energies that is listed in brackets in Table 2.2. This spread is not the uncertainty in the value, but instead the standard deviation of the derived energies. In the sub-monolayer regime, the binding sites on water available to noble gas are of varied strength, as the surface is rough and disordered. This variation results in a spread of desorption binding energies, which in turn is reflected in the standard deviation of the derived energies.

The entrapment efficiency uncertainties, in contrast to the binding energies, are not driven primarily by the temperature uncertainty. This is due to the fact that the entrapment efficiency is independent of the ± 2 K uncertainty in temperature, as the efficiency is a ratio of the amount of noble gas desorbed after 100 K compared to the amount of noble gas desorbed before 100 K. Given that the actual desorption behavior occurs significantly before and after 100 K, the temperature uncertainty does not factor in. There are several other potential sources of uncertainty within

the entrapment efficiencies. First, the water ice thickness as measured with the FTIR spectrometer is subject to an uncertainty in the band strength, which is at most 15%, and dependent on the relative temperature the spectra were taken at. The temperature the IR spectra were taken at in 2018 was 15-17 K, while the post-2020 IR spectra were measured at 12 K. This may account for some of the discrepancy in the measured entrapment efficiencies for both argon and xenon as seen in Figure 2-6. The outliers in the argon and xenon panels with atypically high entrapment efficiencies are for data points acquired post-2021; if the water ice thickness is larger relative to the 2018 data, this would mean that the actual mixing ratio is higher, which may move the entrapment efficiencies to be in line with the other measured data points.

Uncertainty in the entrapment efficiencies may also arise from uncertainties in the measurement of the calibration parameter k_{CO}, which has been estimated in Simon et al., in prep to be $\sim 12\%$. However, this uncertainty is uniform across the experiments using k_{CO} to estimate the amount of noble gas present, so this may be a small overall contribution to the uncertainty.

Unlike the desorption binding energies, the entrapment efficiencies are subject to statistical uncertainties as well as systematic uncertainties (calibration parameter, band strength). This is due to the fact that the entrapment efficiency is likely dependent on the precise structure of the deposited ice. If larger micro-pores form, entrapment efficiency may go down. If more noble gas is deposited close to the surface of the ice, rather than at the bottom of the ice layer, the entrapment efficiency may be lower. Although it is difficult to get exact repeats of experiments, we can compare several experiments in Table 2.4 that have reasonably similar mixing ratios and thicknesses to understand what the order of magnitude uncertainty is. Due to the potential difference in the measured ice thicknesses between 2018 and post-2020, we only compare experiments taken in the same year for this estimate. For argon, the 20220323-1 and 20220324-1 experiments have comparable mixing ratios (2.5,2.9) and thicknesses (37,29). The entrapment efficiencies are within 3% of each other. In the case of krypton, the 20180627-1 and 20180628-1 experiments have comparable

mixing ratios (17,12) and thicknesses (75,111). The entrapment efficiencies for these are approximately the same. In the case of xenon, the 20180916-1 and 20180917-1 experiments have comparable mixing ratios (22,17) and thicknesses (51,75). The entrapment efficiencies are within 2% of each other. Although it may be worth it to more systematically compare the uncertainties for these experiments, this initial examination suggests that the statistical uncertainties are not the dominant factor.

Given that the outliers within the summary Figure 2-6 are from experiments taken in a different experimental setup, it seems possible that the lower base temperature achieved in post-2020 experiments may be driving a systematic underestimation of the water ice thickness and therefore mixing ratio.

2.4 Discussion

We first begin by examining the measured desorption binding energies and their effect on the snowline locations for argon, krypton and xenon. We then proceed to discuss the astrophysical implications of our measured entrapment efficiencies.

2.4.1 Desorption of noble gases

Our multilayer noble gas desorption energy for argon, 845^{120}_{110} K, aligns well with the reported literature value of 902 K [181] when taking into account estimated uncertainties. The desorption energies for krypton and xenon of 1160^{115}_{110} and 1360 ± 100 K do not align as well with the reported values of 1347, and 1756 K [181]. [181] report an approximately 5% uncertainty in their measurements, which means that the Krypton desorption energies just barely overlap, while the xenon energies have a $>$ 200K gap. Although [181] are not explicit in what formulation of the exponential prefactor, ν, they use, it was standard within the literature at the time to couple the prefactor and desorption energy through the harmonic oscillator relation, eq. 2.6. In contrast, we independently fit the prefactor and desorption energy [132]. Regardless of which formulation [181] use, we have substantially different prefactors in units of ML s^{-1} ($\nu_{Smith,Kr} = 6 \times 10^{13}$ vs $\nu_{Kr} = 1.28 \times 10^{11}$; $\nu_{Smith,Xe} = 4.7 \times 10^{12}$ vs $\nu_{Xe} = 3.58 \times 10^{9}$).

This is likely the origin of the discrepancy in multilayer desorption energies.

Our measured sub-monolayer desorption energies of ASW are comparable to those reported by [181] for krypton and xenon (1440 ± 145 K vs 1370 K ; 1995 ± 210 vs 1961 K).In the case of argon, there is a substantial difference. Our measured energy for argon of 1165 ± 175 does not align with the reported value of 866 K [181], although there is only a 90 K difference in the upper bound of the Smith value and lower bound of our value. This discrepancy, as above, could be due to the difference in exponential prefactors. If this is a genuine discrepancy, we believe our value is reasonable as it reflects a similar increase from the multilayer energy to ASW desorption energy as the other two noble gases display.

2.4.2 Noble gas snowline locations

To understand the astrophysical implications of the measured desorption energies, we calculate the snowline locations of argon, krypton, and xenon. The snowline is defined as the location in the disk where at least half of the total species goes from gas to solid phase. In the planetary formation context, this is important as the snowline locations inform what materials solid-body planetesimals are formed from as well as what materials (and in which phases) material is available for accretion to a planetary core. Interior to a snowline, a planet may only accrete noble gas if it is massive enough to begin to accrete gas into its envelope. Exterior to a snowline, a planet can accrete solid noble gas regardless of the core mass.

The snowline location can be calculated by balancing the rates of desorption and adsorption:

$$R_D = n_i^{gr} \nu_i e^{-E_i/T} = n_i^g n_{gr} \sigma_{gr} S_i v_i = R_A \tag{2.7}$$

where n_i^{gr} is the number density of the species on the grain, ν_i is the vibrational escape frequency of the species, E_i is the binding energy, T is the temperature, n_i^g is the number density of the species in the gas phase, n_{gr} is the number density of the grains, σ_{gr} is the cross sectional area of the grain, S_i is the sticking coefficient, and v_i is the thermal velocity. The cross sectional area of the grain is simply πr_{gr}^2, where r_{gr}

is the average grain radius. The vibrational escape frequency can be expressed as:

$$\sqrt{\frac{2k_B E_i N_{sites}}{m_i}} \tag{2.8}$$

where k_B is the Boltzmann constant, N_{sites} is 10^{15} adsorption sites per cm^2, and m_i is the mass of species. The thermal velocity can be expressed as

$$\sqrt{\frac{8k_B T}{\pi m_i}} \tag{2.9}$$

With some algebraic rearrangement, we arrive at an expression for the normalized surface density N_i (equal to 1/2 at the snowline):

$$N_i = \frac{\Omega}{1+\Omega} \tag{2.10}$$

where Ω is

$$\Omega = \sqrt{\frac{N_{sites}}{\pi}\frac{E_i}{T}}\frac{\exp\left(-\frac{E_i}{T}\right)}{2r_{gr}^2 S_i \chi_{gr} n_H} \tag{2.11}$$

where χ_{gr} is the fraction of grains compared to the hydrogen surface density in the disk midplane, and n_H is the hydrogen surface density in the midplane.

The above expression balances microscopic processes; we can use it to understand the structure of a protoplanetary disk. We adopt temperature and surface density profiles from [5] of $T = 200r^{-0.62}$ K and surface density profile $\Sigma = 310r^{-1}$ kg m^{-2} where r is measured in au. These relations are empirically derived from observations of protoplanetary disks. This places the argon, krypton, and xenon snowlines at 35, 24, and 14 au, when considering freeze-out onto ASW surfaces (see Figure 2-7). If Jupiter and Saturn formed in their present day locations, their atmospheres would have accreted any gaseous argon, krypton, and xenon present in the disk.

However, forming interior to the argon, krypton, and xenon snowlines would not explain the uniform enrichment in materials in the Jovian atmosphere. It is possible that Jupiter instead formed exterior to these (and the N_2) snowlines, as suggested in [155]. In this formation mechanism, a nascent Jupiter accreted icy material to its

core. Mixing between envelope and core during bombardment and envelope accretion released argon, krypton, and xenon, resulting in uniform enrichment. This scenario might be aided if, as [157] suggest, a shadowed disk cools the temperature structure, moving the snowline locations closer, resulting in less migration for a nascent Jupiter.

In either scenario, it is possible that additional noble gas be delivered to the Jovian atmosphere by entrapped gases in water ice. If primordial ices survive infall, as [193] suggest, then the original ice structures stay intact. These ices are not deposited sequentially, but instead stochastically in a fashion similar to the ice deposition of our entrapment experiments. As ice grains grow into larger bodies, the ice content may be preserved; comets may contain entrapped noble gases. As these bodies migrate from a region external to noble gas snowlines to interior regions, they preserve much of the noble gas. When these bodies impact nascent planets, they add additional noble gas to the atmosphere.

2.4.3 Entrapment of noble gases

We see high entrapment efficiencies for all three noble gases in astrophysically relevant ice mixing ratios. These efficiencies show a weak dependence on species and precise ice thickness; after ratios of $> 30 : 1$ water to noble gas, even the precise ratio does not seem to substantially affect the entrapment efficiency. Based on these experiments, we expect that the ratios of noble gases entrapped in ices in protoplanetary disks will have close to solar ratios with respect to each other.

There are limited previous experiments on the entrapment of argon, krypton, and xenon. The most thorough experiments exist for argon and water mixtures. Generally, the trends observed in previous work are borne out by our data. [150] report 10% entrapment of argon in a 1:1 mixture with water, at a 0.1μm ice thickness. This is in line with the two calibration experiments we have done at low ratios, where we get entrapment of $\sim$28%. The general trend of decrease in trapping efficiency with a decrease in the ratio of H_2O to water seems supported by this datapoint. [9] have an experimental scheme similar to our high ratio ices; they deposit $\sim$1 ML argon under $\sim$100 ML of porous amorphous water ice. This schema yields 65% entrapment of

argon, which is well in line with our efficiencies that exceed 60% in astrophysically relevant ratios.

The high entrapment efficiency suggests that planets may accrete materials that are enriched in noble gases. It also supports the delivery of noble gases to planetary atmospheres via comets. Further theoretical work should be done to model delivery. This work also does not consider the effect of additional volatile species on either desorption kinetics or trapping efficiency. Given that the snowline locations of argon, krypton, and xenon suggest freezing out onto CO_2 and CO ices, experimental investigations of the desorption binding energies of the noble gases on those species are needed to better refine snowline locations. Experimental investigations of efficiency in gas mixtures should be explored to provide a more accurate picture of trapped noble gases in protoplanetary disks. [10] provides an initial attempt at studying mixtures of argon, CO, and N_2 in amorphous solid water, and find that both argon and CO are efficiently trapped, while N_2 is not; this suggests that the behavior we see experimentally here may hold even in multi-component mixtures.

2.5 Conclusions

In this work, we have measured both the multilayer and sub-monolayer desorption binding energies of argon (845,1165 K), krypton (1160,1440 K), and xenon (1360,2000 K) on amorphous solid water. These values place the snowline locations at 35, 24, and 14 au, assuming binding to water ice dominates the desorption kinetics. We have additionally measured the entrapment efficiencies of these species. In astrophysically relevant ice analogs ($\geq$ 50:1 ratio), trapping efficiency exceeds 65% for all three noble gas species, and can be as high as 90% . There does not appear to be a strong dependence on the molecular weight of the species, or indeed the thickness of the ice layer beyond 50 ML. These results suggest that noble gases are efficiently trapped in primordial interstellar ices. This further suggests that comets may contain large amounts of entrapped noble gases, enabling delivery to nascent planetary atmospheres.

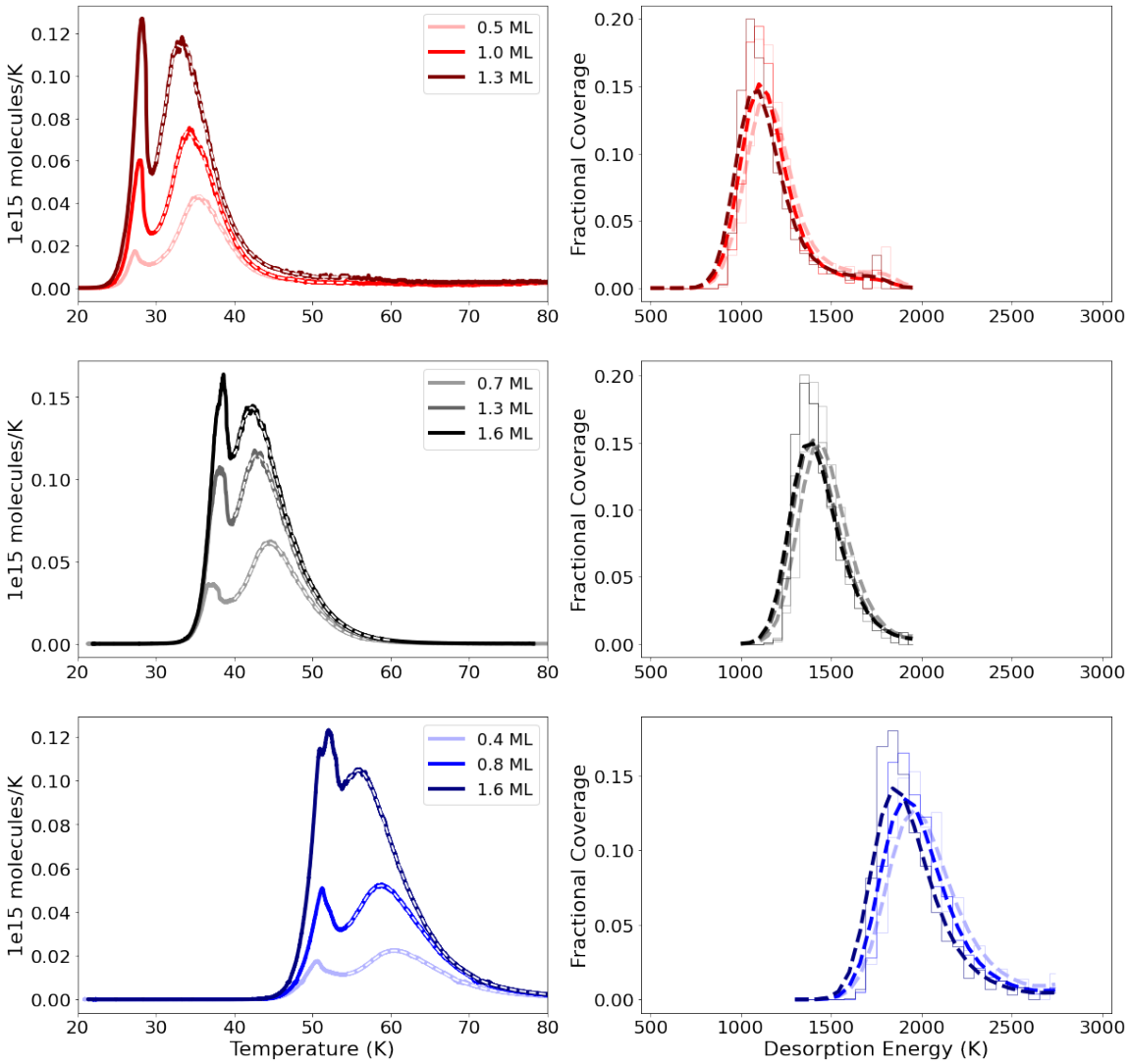

Figure 2-4: **(Left)** Temperature programmed desorptions for monolayer and sub-monolayer coverages of argon, krypton, and xenon on ASW. The characteristic double peak of a first order desorption is present. The dashed lines indicate fits to the first order behavior. **(Right)** Results of the fitting algorithm indicate the spread in desorption energies.

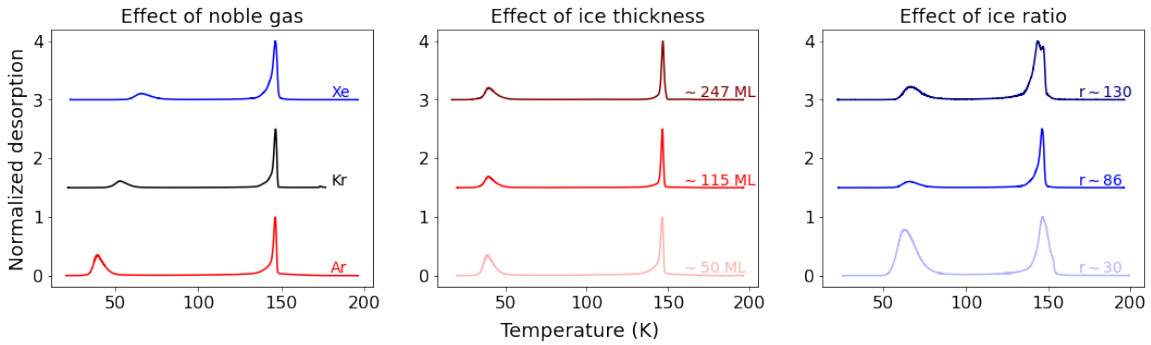

Figure 2-5: TPD curves for a selection of entrapment experiments. All experiments are normalized to the maximum desorption rate in that experiment. **(Left)** From bottom-to-top, the desorption curves for argon (red), krypton (black), and xenon (blue). Selected experiments have comparable water to noble ratios, and comparable ice thicknesses. **(Center)** From bottom-to-top, the desorption curves for increasing ice thicknesses of comparable water to argon ratios. **(Right)** From bottom-to-top, the desorption curves for increasing ratios of water to xenon, for comparable ice thicknesses. For detailed information on each experiment selected for this plot, please see Table 2.3.

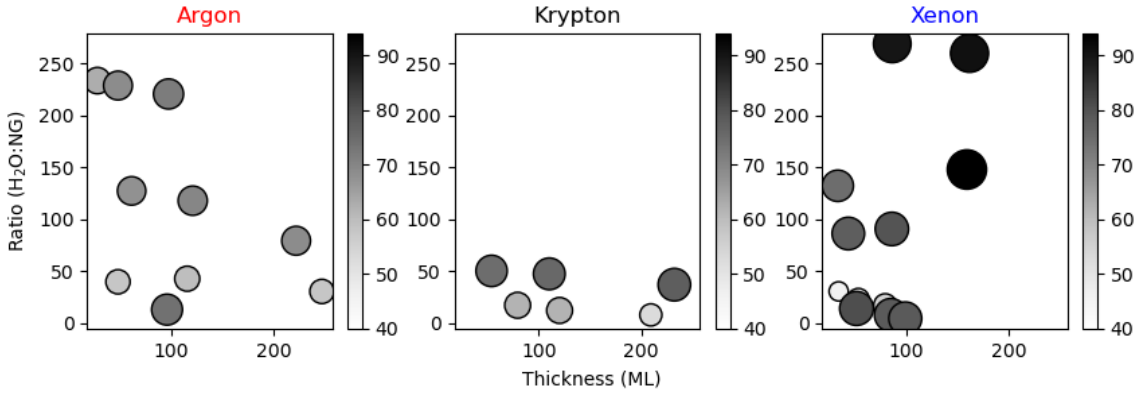

Figure 2-6: Summary of entrapment efficiencies. The x-axis on all plots corresponds to the thickness of ice deposited onto the substrate, while the y-axis on all plots corresponds to the ratio of water to ice. The color bar represents the entrapment efficiency and ranges from 40% to the maximum entrapment efficiency recorded in these experiments (94%). The marker area scales linearly with the entrapment efficiency. The left panel represents the summary of experiments for argon, the central panel the summary for krypton, and the right panel for xenon.

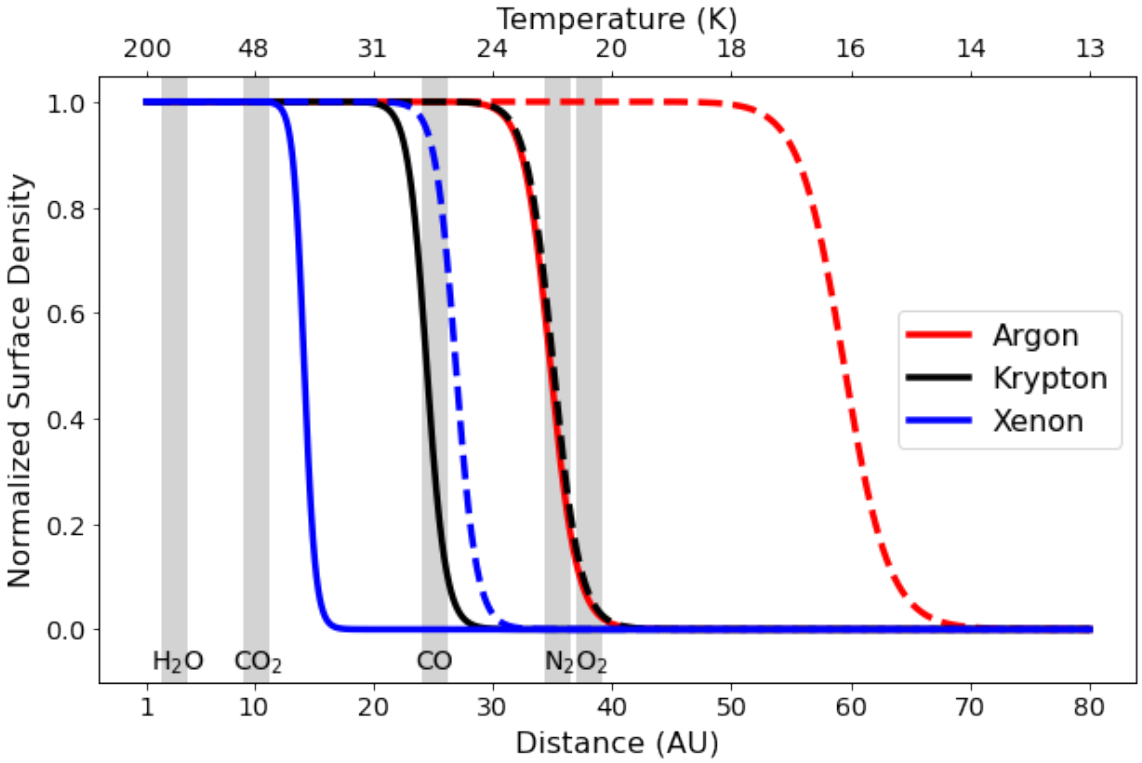

Figure 2-7: Argon, krypton, and xenon snowlines in the context of other astrophysically relevant snowlines. The top axis gives the disk midplane temperature at the radial distance (bottom x axis) from the star. Each shaded bar represents the location of an astrophysically relevant snowline (from left to right, H_2O, CO_2, CO, N_2, and O_2), as calculated from the [181] binding energies to ASW. In this plot, the solid lines are the snowlines as calculated for the noble gas-water desorption energy while the dashed line is the snowline as calculated for the pure ice desorption.

Table 2.4: List of noble gas entrapment experiments

Date	Species	Ratio	ML Water	ML Noble Gas	Entrapment (%)
20180324 - 1*	Ar	30	239	7.9	58
20180614 - 1*	Ar	79	219	2.8	69
20180615 - 1*	Ar	127	61	0.5	68
20180615 - 2*	Ar	118	120	1.0	70
20180616 - 1*	Ar	40	47	1.2	58
20180618 - 1*	Ar	42	113	2.7	60
20180927 - 1*	Ar	241	28	0.1	63
20180927 - 2*	Ar	231	48	0.2	69
20180927 - 3*	Ar	219	97	0.4	72
20210924 - 1*	Ar	35	89	2.6	74
20220323 - 1*	Ar	2.5	37	15.0	25
20220324 - 1*	Ar	2.9	22	7.7	28
20220324 - 2*	Ar	5.2	122	23.5	47
20180309 - 1*	Kr	37	226	6.2	78
20180322 - 1*	Kr	8	185	24.3	53
20180626 - 1*	Kr	47	108	2.3	76
20180626 - 2*	Kr	50	53	1.1	75
20180627 - 1*	Kr	17	75	4.4	62
20180628 - 1*	Kr	12	111	9.3	62
20180912 - 1*	Xe	30	33	1.1	46
20180916 - 1*	Xe	22	51	2.3	53
20180917 - 1*	Xe	17	75	4.4	55
20180918 - 1*	Xe	130	33	0.3	75
20180919 - 1*	Xe	86	43	0.5	78
20180920 - 1*	Xe	90	85	0.9	80
20210920 - 1**	Xe	7	75	10.1	79
20210921 - 1**	Xe	14	48	3.5	81
20210921 - 2**	Xe	4	80	19.0	79
20210922 - 1**	Xe	266	86	0.3	90
20210922 - 2**	Xe	260	161	0.6	91
20210923 - 1**	Xe	147	158	1.1	94

*ratio determined with ion-to-monolayer conversion described in Section 2.2.4
**ratio determined with k_{CO} conversion described in Section 2.2.4

Chapter 3

Experimental determination of the desorption binding energies and entrapment efficiencies of Neon in water ice

3.1 Introduction

Neon is an important tracer of volatile delivery within the solar system, and by extension of volatile delivery during planet formation. As a noble gas, its distribution in a protoplanetary disk is not influenced by chemical reactions, but instead only by its physical properties. Given its high volatility, it is likely that it will be present in the nebular gas phase around most planets forming in the solar system. Depending on its entrapment efficiency, there may be an additional solid reservoir from which to deliver neon. The extent to which neon traces solid volatile delivery as opposed to gaseous accretion remains to be seen.

Several bodies within the solar system have in-situ measurements of neon. Notably, Earth's neon component points to the accretion of a primordial, nebular primary atmosphere [98]. The nebular neon may have dissolved into the magma ocean,

eventually being subducted into the core. Venus has limits on neon detection, but the uncertainties in abundances make it difficult to make definitive claims about the history of Venusian formation. Neon has been detected on Mars [97], and appears to be a probe for the interior of the planet. However, additional data is required to determine the abundance and isotopic composition and place better constraints on neon origin.

The atmosphere of Jupiter is depleted with respect to neon (0.1 solar ratio relative to H_2) while argon, krypton and xenon are enhanced with approximately 2.5 times solar ratio relative to H_2. It is currently hypothesized that the depletion in neon is as a result of neon raining out in helium droplets [198]. Neon has been detected in Titan's atmosphere with the Huygens probe [146], with a $^{22}Ne/^{36}Ar$ ratio consistent with 0.05 to 2.5 times solar abundance. Additional in-situ data are required to fully interpret the results and make statements about formation mechanisms, namely whether Titan could have accreted solid forms of neon, or if it required to have accreted nebular gas. [8] note that noble gas data is required for Uranus and Neptune within the solar system to determine volatile delivery history.

These case studies make it clear that neon abundances vary widely within solar system bodies, and that it can trace the way delivery occurs. To fully understand delivery pathways, however, it is important to understand whether neon will occur exclusively as a gas in the protoplanetary disk, or if it will occur in solid ices. To this end, it is important to measure the desorption energies and entrapment efficiencies of neon experimentally.

There is some previous work done in quantifying the desorption and entrapment behavior of the heavier noble gases argon, krypton, and xenon, (see i.e. Schneiderman et al. in prep., Simon et al. in prep, [181, 10, 150, 9, 151]). However, there is no existing data for neon, likely due to its low temperature of desorption. We have built a new chamber that reaches a sample holder base temperature of 4 K, which opens the door to providing measurements of the entrapment and desorption of neon for the first time (Maksiutenko et al., in prep). It is of particular interest to measure the entrapment efficiency of neon in water ice matrices to see if the behavior is similar

to the heavier noble gases; if the behavior is similar, it is expected that primordial interstellar ices would have solar ratios of the noble gases with respect to each other. If neon is less efficiently trapped than the other noble gases, it provides interesting constraints on how much neon is deliverable in ice form. In either case, having this data for neon will enable us to understand whether neon is solely a tracer of gas accretion, or if neon's story within a protoplanetary disk is more complicated.

In this work, we explore the desorption binding energies and entrapment efficiencies of neon in amorphous water ices in a laboratory setting. In section 3.2, the experimental setup is presented. In section 3.3, the experimental results are given. In section 3.4, the results and their astrophysical implications are discussed.

3.2 Methods

3.2.1 Experimental Setup

These experiments were carried out in the SPACETIGER experimental setup, first introduced in [120] and fully described in an upcoming paper (Maksiutenko et al., in prep). This setup consists of a 500 mm diameter spherical stainless steel, ultra-high-vacuum (UHV) chamber custom made by Pfeiffer Vacuum. This system is able to investigate the thermal processing of interstellar ice analogs, among other forms of energetic processing. The chamber achieves a base pressure of $\sim 10^{-9}$ torr and is pumped by a Pfeiffer Vacuum HiPace 300 (pumping speed 260 l/s for N2). The pressure in the UHV chamber is measured by an IONIVAC IM 640 extractor pressure gauge.

Ice samples are grown in situ on a 10 mm diameter CsI substrate mounted on an oxygen-free high thermal conductivity (OFHC) copper sample holder in the center of the UHV chamber. The sample holder is surrounded by a gold-plated radiation shield connected to the first stage of a closed-cycle He cryostat (Model DE210b-g, Advance Research Systems, Inc.) powered by an ARS-10HW compressor. The sample holder can be cooled to 4.3 K, as verified by a calibrated Si diode sensor and

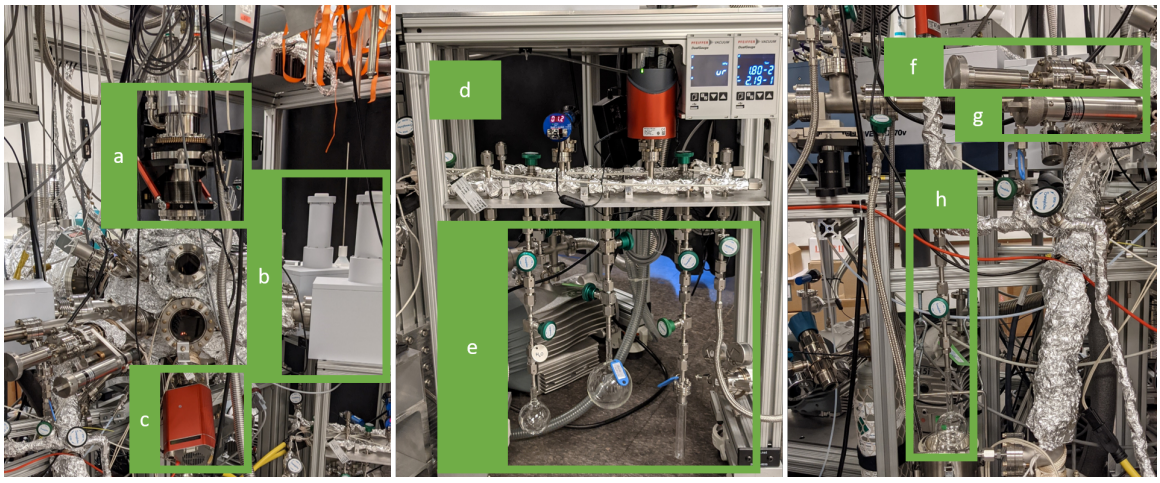

Figure 3-1: Pictures of the experimental setup. **Left:** The SPACETIGER chamber (a) UHV rotary seal (b) Transmission and reflection FTIR detectors (c) Quadrupole mass spectrometer **Center:** The gasline area. (d) to pump (e) Connections for gas bottles and volumes **Right:** The dosing area and mixing volume (f) Dosing assembly and pinhole array. (g) Translational stage. (h) Mixing volume and flask.

monitored by a Lakeshore Model 336 temperature controller. The cryostat is attached to the top port of the UHV chamber; a differentially pumped (Leybold Turbolab 90i pump station with 90 ls^{-1} pumping capacity) UHV rotary seal (Thermionics ZC-B600C-T600TM-4.00-3/LMM & RNN-400/TM/FA) allows for 360° rotation and 10 cm z-axis translation in the sample holder.

Ice samples are deposited in SPACETIGER by exposing the substrate on the sample holder to a constant flow of gas from an independently pumped stainless steel gas line. The gas line assembly is pumped by an Edwards TIC pumping station with a NEXT85D turbomolecular pump and a nXDs 6i scroll pump down to $\sim 10^{-7}$ torr base pressure. Gas line pressure is measured with two Pfeifffer CMR372 Baratron pressure gauges. The gas line contains ports for connection of different species. In addition, there is a mixing area off to the side of the gas line (see Figure 3-1) whose pressure is measured by a PCR 280 Baratron pressure gauge.

The gas line is connected to the chamber via an isolation valve, 10 mm diameter dosing tube mounted on a MDC LMT-154 translational stage, and pinhole array. During dosing, the dosing tube is within 2 mm of the substrate. The dosing tube is isolated by a bellows insulated metal seal valve (SS-4H-VCR). Dosing ends by

evacuating the gas line assembly.

Water ice sample thickness can be measured with a Bruker 70v Fourier transform infrared spectrometer (FTIR) equipped with a liquid-nitrogen-cooled MCT detector. The spectrometer and MCT detector chamber are evacuated to 2 mbar using Edwards scroll pumps nXDs 15i (4 l s^{-1}. The FTIR spectrometer is operated in transmission mode.

The temperature of the ices is monitored and controlled by a LakeShore 336 temperature controller with a calibrated Si diode sensor with 2 K estimated accuracy and a 0.1 K relative uncertainty. The ice samples can be warmed from the base temperature of the instrument (∼4K) to room temperature with a 50 W silicon nitride cartridge heater rod (Bach Resistor Ceramics) embedded into the OFHC copper sample holder. Gas composition in the chamber is monitored with a QMG 220M1 quadrupole mass spectrometer (QMS) from Pfeiffer, with a mass range of 100 amu and resolution of 0.5 amu.

3.2.2 Calibration of the QMS signal

In the case of infrared inactive species such as neon, the amount of species present can be determined by comparing the QMS response to the calibrated QMS response of an infrared active species (^{13}CO), as described in [119], Simon et al. (in prep), and Schneiderman et al. (in prep). The integrated ion current of a noble gas during a TPD can be related to the number of molecules desorbed during the TPD via:

$$A(m/z) = k_{CO} \times \frac{\sigma^+(mol)}{\sigma^+(CO)} \times N(mol) \times \frac{I_F(mol)}{I_F(CO^+)} \times \frac{F_F(mol)}{F_F(CO)} \times \frac{S(m/z)}{S(29)} \qquad (3.1)$$

where $A(m/z)$ is the integrated ion current of a given mass fragment (m/z) during desorption, $\sigma^+(mol)$ is the ionization cross section for the first ionization of the species at the incident electron energy of the mass spectrometer (70 eV), $N(mol)$ is the total thickness of the noble gas deposited, $I_F(mol)$ is the ionization fraction of a noble gas with charge z, $F_F(mol)$ is the mass fractionation of a species of interest (definitionally $F_F(mol) = 1$ in the case of a noble gas), $S(m/z)$ is the sensitivity of the QMS to a

Table 3.1: Summary of the calibration parameters

Species	m/z	$\sigma^+(mol)^*$	$I_F(mol)^{**}$	$S(m/z)^{**}$
Ne	20	4.75×10^{-17}	0.9998	3.25×10^{14}
^{13}CO	29	2.52×10^{-16}	1.0000	1.88×10^{14}
Ar	40	2.52×10^{-16}	0.8909	1.10×10^{14}
Kr	84	3.45×10^{-16}	0.8029	5.45×10^{13}

* [168] ** Experimentally measured for this setup

mass fragment (m/z), and

$$k_{CO} = \frac{A(29)}{N(CO)} \tag{3.2}$$

is the proportionality constant that links the integrated ion current $A(29)$ of ^{13}CO to the thickness of CO measured with the IR spectrometer $N(CO)$. The proportionality constant k_{CO}, sensitivity $S(m/z)$, and ionization fraction $I_F(mol)$ have been determined experimentally for this chamber setup (see Sections 3.2.2 and 3.2.2). A summary of the calibration parameters used in this equation is found in Table 3.1.

Determination of the sensitivity relation and ionization fraction

The sensitivity of the QMS, $S(m/z)$ to a mass fragment (m/z) should be experimentally determined for a given setup. We measure the sensitivity of the instrument to the noble gases neon, argon, and krypton; the procedure to do so is to leak noble gas into the chamber and measure both the pressure in the chamber and the QMS signal at three leak rates. With these measurements, the sensitivity of the instrument can be calculates from the QMS ion current, $I(m/z)$ for mass fragment (m/z):

$$I(m/z) = k^*_{QMS} \times \sigma^+(mol) \times P(mol) \times I_{S_F}(m) \times I_F(z) \times F_F(m) \times S(m/z) \tag{3.3}$$

This equation is similar to eq. 3.1, with three new factors: k^*_{QMS}, a proportionality constant that is the same for different species in the chamber, $P(mol)$, the pressure measured in the chamber, and I_{S_F}, an isotopic factor. The isotopic factor arises because the pressure gauge in the chamber does not discriminate between different isotopologs of the same species while the QMS does. The pressure needs to be addi-

tionally corrected by gas correction factors provided by the gauge manufacturer (0.3, 1.29, and 1.94, for neon, argon, and krypton, respectively). The average sensitivities for the noble gases across three pressure levels are listed in Table 3.1.

With these three data points an exponential fit of the form $\alpha e^{-\beta x} + \gamma$ can be acquired from which the sensitivity for any other mass fragment can be calculated. The sensitivity relation for this instrumental setup is

$$S(m/z) = \left(12.93e^{-0.078(m/z)} + 0.53\right) \times 10^{14} \tag{3.4}$$

While measuring the sensitivities of the noble gases in the chamber, we were able to additionally measure the ionization fraction for each noble gas. While leaking noble gas into the chamber, we can measure (m/z) for $z = 1, 2, 3$. The ionization fraction thus becomes:

$$I_F = \frac{\left(\frac{m}{z=1}\right)}{\left(\frac{m}{z=1}\right) + \left(\frac{m}{z=2}\right) + \left(\frac{m}{z=3}\right)} \tag{3.5}$$

The calculated values are listed in Table 3.1.

Determination of the CO proportionality constant

The ^{13}CO proportionality constant, k_{CO} is required to calculate the amount of neon and argon present in our ice mixtures. To do this, we prepare mixtures of H_2O and ^{13}CO and deposit on to the cold substrate with the methods described in Section 3.2.3. These mixtures are then measured with the IR spectrometer in transmission mode, and then desorbed at a constant rate of 1 K min^{-1}, again as described in Section 3.2.3. The integrated ion current is then compared to the number of monolayers, as determined with the IR spectrometer, yielding the proportionality constant described in eq. 3.2. The values used to determine the proportionality constant are found in Table 3.2.

3.2.3 Experimental Procedure

Experiments described below use deionized water purified through several LN_2 freeze-pump-thaw cycles. Experiments additionally use ^{20}Ne (Ultra High Purity, Matheson). For all experiments, the sample holder is first fully cooled to 4K, rapidly heated to 200K to desorb any species that may have adhered to the sample holder, and then re-cooled to the temperature of the experiment.

Binding energies

To measure both multilayer (zeroth-order) and submonolayer (first-order) desorption kinetics, $\geq$50 ML of DI water are deposited onto the CsI substrate at 100 K over the course of 20 minutes. The substrate is then cooled to the base temperature of the chamber ($\sim$4 K). Submonolayer to multilayer coverages of neon are deposited over the course of 1-15 minutes. Following deposition, ices are heated at a constant rate of 1 K minute^{-1} to 70 K. Desorbing species are monitored with the QMS, see section 3.2.1 The water ice substrate is reused for an additional one or two experiments that day. Experiments of this form are common within the literature, see i.e. Schneiderman et al. in prep; [56, 181].

Neon ice thickness is estimated after deposition via the empirically-derived conversion factor described in Section 3.2.2.

Entrapment efficiencies

Two methods are used to determine the entrapment efficiency of neon in water ice: mixture deposition and burial trapping. The first method utilizes the deposition of prepared mixtures of neon and water onto the substrate and presents a good measure

Table 3.2: Summary of the k_{CO} parameters

H_2O:^{13}CO	$\int i_{CO}$	ML_{CO}	k_{CO}
13.6:1	2.14×10^{-10}	9.77	2.19×10^{-11}
10.0:1	2.54×10^{-11}	1.62	1.57×10^{-11}
15.3:1	3.58×10^{-11}	1.91	1.87×10^{-11}
			$(1.87 \pm 0.31) \times 10^{-11}$

of the entrapment at a specific ratio. Due to the high volatility of neon and specifics of our experimental setup, it is difficult to achieve highly dilute mixtures of neon and water, and so we are unable to measure the rate of entrapment of neon in an astrophysically-analogous ice mixture. To estimate the upper limit on this entrapment rate, we utilize burial trapping.

Mixture entrapment: Mixtures of DI water and neon are first prepared in the fixed volume mixing area. Approximately 30 hPa of water vapor is released into the fixed volume of the mixing area. This amount of water is condensed into the LN_2-submerged vacuum flask attached to the mixing area. This freezing cycle is repeated multiple times, after which between 0.5 and 10 hPa of neon is put into the mixing area. The vacuum flask is opened to the mixing area and the noble gas and water sit overnight to ensure proper mixing between components. The following day, the mixtures are deposited at 4 K onto the CsI window. Deposition of water at this low temperature ensures ice structures analagous to the water ices that would form through grain-surface chemistry in the interstellar medium (ISM) [59]. After deposition, the water ice thickness is measured with the FTIR spectrometer described in section 3.2.1. Then, the ices are heated at a constant rate of 1 K minute^{-1} to 200 K. The desorbing species are monitored with the QMS (section 3.2.1).

Burial entrapment: Thin layers of neon are deposited at 4 K onto the CsI window. Then, between 50 and 200 monolayers of water are deposited (thickness measured with the FTIR spectrometer described in section 3.2.1. Although this method does not estimate the entrapment rate of neon in pores in water ice, it does estimate the maximally efficient trapping rate of highly dilute mixtures of neon and water. After deposition, the ices are heated at a constant rate of 1 K minute^{-1} to 200 K. The desorbing species are monitored with the QMS (section 3.2.1.)

For both methods, the entrapment efficiency is calculated as the ratio of the amount of neon that desorbs between 150 to 175 K to the amount of neon that desorbs between 5 to 30 and 150 to 175 K.

3.3 Results

3.3.1 Measurement of binding energies

We are unable to definitively measure the multilayer (zeroth-order) and monolayer (first-order) desorption binding energies of neon to amorphous solid water (ASW). The nominal coverages in a given experiment are calculated by using the proportionality constant described in Section 3.2.2. However, the shapes of the curves for the given coverages are atypical of what is expected based on other noble gas experiments. It is possible that the first large peak that occurs at $\sim$ 10 K (see Figure 3-2) is not the multilayer desorption peak, but instead forced neon desorption through H_2 desorption. In addition, previous noble gas experiments (see Schneiderman et al., in prep) have shown that argon, krypton, and xenon see monolayer desorption behavior emerging at coverages substantially below 1 ML; pooling and non-uniform distribution of noble gas is suspected to be the cause. In calibration experiments performed on this experimental setup, argon monolayer desorption behavior emerges at coverages of $\sim$ 0.35 ML, which is consistent with the observations in previous experiments. Regardless of the precise origin for the desorption peaks of neon, neon will be totally desorbed by 20 K in a protoplanetary disk. If the forced H_2 desorption is real and applicable in the interstellar context, neon will desorb by 15 K in the protoplanetary disk.

3.3.2 Measurement of entrapment efficiencies

We use two methods of determining the entrapment efficiency of neon in water ice. The mixture entrapment method described in Section 3.2.3 produces an analog ice with similar structure to what would be expected in the ISM. In this ice structure, neon might occupy micropores and persist interior to its snowline. For the ratios achieved (see Table 3.3), we see entrapment efficiencies that are uniformly below 1%. There is a dependence of the efficiency on the mixing ratio; with decreasing neon concentration, the entrapment efficiency increases. By eye, the trapping efficiency

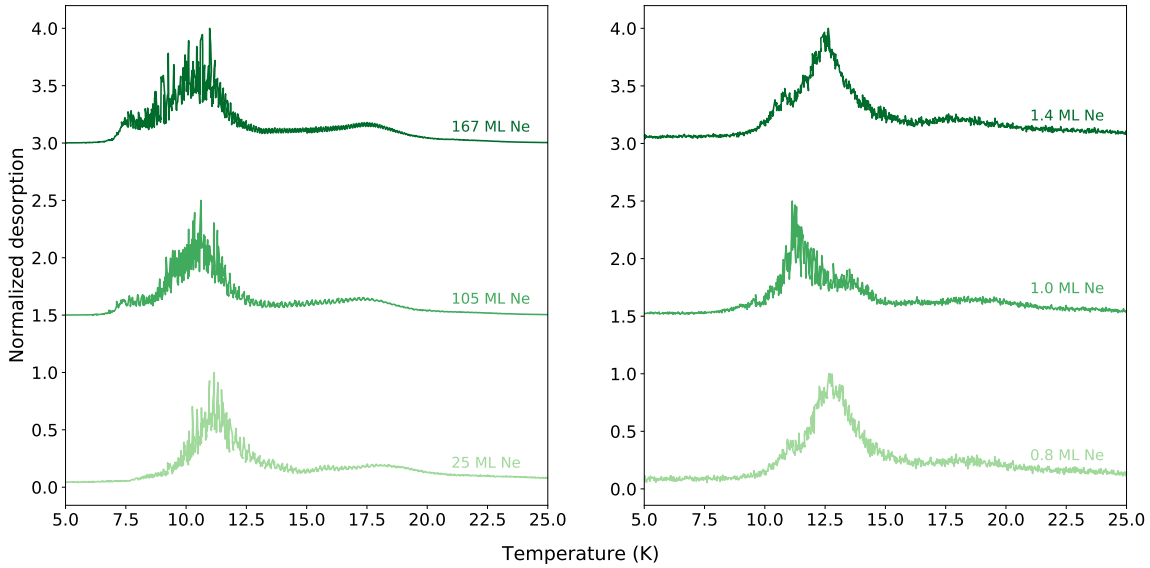

Figure 3-2: Neon on top of amorphous solid water desorptions. All curves are normalized to the maximum desorption rate in that experiment, and offset for ease of viewing. **Left:** Desorption experiments for neon with coverages substantially above a monolayer. **Right:** Desorption experiments for neon with coverages near a monolayer.

slightly increases with increasing ice thickness, but this effect is hard to measure with such low entrapment efficiencies (see Figure 3-3).

The burial entrapment method described in section 3.2.3 provides an upper limit on the amount of entrapment possible for neon in water ice. In this scenario, water is deposited on top of a thin layer of neon. We find that the efficiency in this scenario does not exceed 10%. For the thinner case, the efficiency is <1%; this may be due to the larger amount of neon deposited under the water ice, or it may be that substantial

Table 3.3: Mixture entrapment experiments

ML H_2O	ML Ne	Ratio	Efficiency
20	26	0.7	<1
27	54	0.5	<1
63	134	0.5	<1
34	6	5.8	<1
74	13	5.7	<1
144	34	4.2	1
289	63	4.6	1

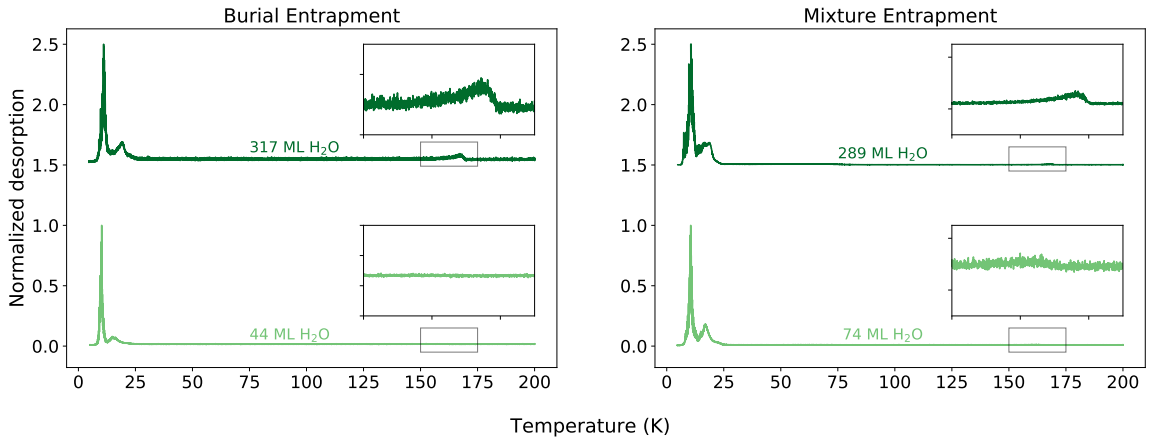

Figure 3-3: Comparison of burial and mixture entrapment experiments. All curves are normalized to the maximum desorption rate in an experiment, and offset for ease of viewing. Insets focus on the desorption of entrapped neon. **Left:** Burial entrapment experiments. Curves from top to bottom are in decreasing amounts of water capping the neon layers. **Right:** Mixture entrapment experiments for ices with a mixing ratio of ∼5:1 water to neon. Decreasing ice thicknesses from top to bottom.

Table 3.4: Burial entrapment experiments

ML Ne	ML H_2O	Efficiency (%)
12	44	<1
5	317	10

amounts of water ice are required to efficiently trap neon. With the thicker layer of neon under the water ice, larger channels to the ice surface may have been created, allowing for efficient removal of neon from beneath the ASW cap.

3.4 Discussion

These data make reasonably clear that, unlike the heavier noble gases argon, krypton, and xenon, neon is not readily trapped and is therefore primarily a tracer of gas-phase volatile delivery to terrestrial atmospheres. The neon snowline will be well outside the region of terrestrial planet formation, and outside the region of the formation of the Solar system gas giants., and likely outside of the comet forming zone. Delivery of entrapped neon in icy bodies is unlikely, as the entrapment efficiencies for neon are almost an order of magnitude lower than those observed for the heavier noble

gases. In comparable mixtures of water and argon (see Schneiderman et al., in prep and Simon et al., in prep), entrapment efficiencies exceeding 25% are observed - substantially higher than our measured neon efficiencies below 1%. While burial trapping experiments do not exist for krypton and xenon, a burial entrapment study in argon (see [9]) finds that burial trapping of Argon results in ∼65% entrapment, compared to the 10% entrapment we see in the most optimistic case for neon.

Our experiments confirm current assumptions that terrestrial neon traces nebular gas accretion to the primary atmosphere of the nascent Earth. Given that neon will not exist in solid form within the terrestrial planet forming region, and it is unlikely to be delivered via entrapment in comets, the only source for neon is direct accretion from nebular gas. In the case of Venus, with a similar mass to Earth, we might expect that observations of atmospheric neon also point to nebular origin; for both Earth and Venus, nebular neon may have dissolved into magma oceans and been subducted into the core, to be released via outgassing at later epochs. Mars, with its smaller mass, may not have had sufficient gravity to accrete a primary atmosphere, and thus may show substantial depletion in neon. Although Titan formed outside of the terrestrial region, it too will have formed in an area with gaseous neon. Its lower mass makes it also unlikely to have accreted abundant nebular gas as part of a primary atmosphere, and thus we expect it to be depleted in neon.

Jupiter shows a depletion in neon of 0.1 with respect to solar, while it shows an enrichment in the heavier noble gases of ∼2.5. The lack of neon entrapment may partially explain this depletion. Given that Jupiter accreted gas-phase nobles from the nebula, it is expected that it accreted solar-ratio levels of the noble gases. However, delivery via icy bodies may have enriched argon, krypton, and xenon, while maintaining neon at Solar levels. Current theory posits that neon rains out in helium droplets within the interior of Jupiter; this mechanism need only explain the depletion from solar ratios of neon to 0.1 solar.

3.5 Conclusions

In this work, we have measured the burial entrapment efficiency of neon to be at most 10%. We have additionally measured the mixture entrapment efficiency of 5:1 H_2O:Ne mixtures to be at most 1%. These results suggest that in contrast to the heavier noble gases argon, krypton, and xenon, neon is inefficiently trapped in primordial interstellar ices. Neon should be treated as a tracer of nebular gas accretion, rather than delivery via comets. We are unable to definitively measure the multilayer or sub-monolayer desorption binding energy of neon as it appears that neon is forced from the substrate by desorbing H_2. All neon desorbs in the experiment by 25 K, with desorption beginning at 7.5 K.

Chapter 4

Carbon monoxide gas produced by a giant impact in the inner region of a young system

Models of terrestrial planet formation predict that the final stages of planetary assembly - lasting tens of millions of years beyond the dispersal of young protoplanetary disks - are dominated by planetary collisions. It is through these giant impacts that planets like the young Earth grow to their final mass and achieve long-term stable orbital configurations [136]. A key prediction is that these impacts produce debris. To date, the most compelling observational evidence for post-impact debris comes from the planetary system around the nearby 23-million-year-old A-type star HD 172555. This system shows large amounts of fine dust with an unusually steep size distribution and atypical dust composition, previously attributed to either a hypervelocity impact [105, 83] or a massive asteroid belt [204]. Here, we report the spectrally resolved detection of a CO gas ring co-orbiting with dusty debris between about six and nine astronomical units - a region analogous to the outer terrestrial planet region of our Solar System. Taken together, the dust and CO detections favor a giant impact between large, volatile-rich bodies. This suggests that planetary-scale collisions, analogous to the Moon-forming impact, can release large amounts of gas as well as debris, and that this gas is observable, providing a window into the composition of

young planets.

4.1 Main

HD 172555 is a (23 ± 3)-Myr-old [111] A-type star with a mass of 1.76 $M_\odot$ [43] and a luminosity of 7.7 $L_\odot$, located 28.5 pc [166, 21] from Earth within the young β Pictoris moving group [210]. Its planetary system hosts large amounts of dust in the terrestrial region, producing an infrared (IR) excess best fit by warm (290 K) dust [37] with an IR luminosity 7.2×10^{-4} times that of its host star [204]. Spatially resolved mid-IR observations constrain this dust to a disk of material in the inner, less than 10 au region, viewed close to edge-on from Earth [180, 55]. Rare solid-state emission features detected at 8–9.3 μm [29] indicate the presence of glassy silica (tektites and obsidian) and solid silicon monoxide. These require high-temperature processing and vapour condensation, supporting a hypervelocity ($> 10\,\mathrm{km\,s^{-1}}$) impact between planetary bodies for the origin of the dust [105, 83]. Detailed, self-consistent modelling indicates that this impact scenario can explain the spectral features, as well as the overabundance of submicrometre-sized grains and steep size distribution inferred from the Spitzer IR spectrum [83].

We used the Atacama Large Millimeter/Submillimeter Array (ALMA) to detect the dust continuum and carbon monoxide (CO)$J = 2 - 1$ (where J is the total angular momentum quantum number) gas emission from the HD 172555 system 4-1. The compact, spatially unresolved dust and gas emission originates from within 15 au of the star, consistent with previous IR and optical observations. The spectrum of CO in 4-2 is extracted from the ALMA data cube and is spectrally resolved. The double-peaked profile is expected from gas orbiting in Keplerian rotation around the central star. The centroid of the CO profile is at a heliocentric velocity of 2.3 ± 0.2 km $\mathrm{s^{-1}}$, consistent with the stellar velocity [63], confirming that the gas emission is associated with the HD 172555 system.

We modelled the CO emission as a vertically thin ring of optically thin gas with radially and azimuthally uniform surface density between an inner and outer bound-

ary, in Keplerian rotation around the central star. We find that the CO is confined to a ring of radius about 7.5 au and width about 3.3 au. The data are consistent with a symmetric disk model; we find no strong evidence of asymmetry between the blue-shifted and red-shifted sides of the CO spectral line profile. We convert the integrated flux of 120 mJy km s^{-1} to a CO gas mass considering no-local thermodynamic equilibrium excitation, finding masses in the range between $0.45 \times 10^{-5} M_{\oplus}$ and $1.21 \times 10^{-5} M_{\oplus}$ for temperatures between 100 K and 250 K. The total millimetre dust mass, as calculated from the observed continuum emission, is $(1.8 \pm 0.6 \times 10^{-4} M_{\oplus}$ for an expected equilibrium blackbody temperature of 169 K at 7.5 au.

To test our assumption that the CO $J = 2 - 1$ emission is optically thin, we create a full three-dimensional radiative transfer model of the ring with the spatial morphology described above. For a gas temperature comparable to, or higher than, the expected blackbody temperature of 169 K at 7.5 au, we find low optical depths, which validates our optically thin assumption. This corresponds to total CO masses of $(1.4 \pm 0.3 \times 10^{-5} M_{\oplus}$ at 169 K. However, we find that colder ($\ll$ 100 K) temperatures would require higher optical depth and much higher CO masses to reproduce our observed CO line emission 4-2. This temperature-mass degeneracy can be resolved by the detailed spectral shape of the emission as models of optically thin, warm gas constrained to a narrow ring produce sharper peaks compared with the optically thick, cold models 4-2. We find that the data are better fit by less massive, warmer models (lower χ^2).

The observed CO gas in the circumstellar environment around HD 172555 will be subject to photodissociation from the stellar and interstellar ultraviolet (UV) field. The former dominates at the 7.5 au location of the CO ring and causes CO (if unshielded) to be rapidly destroyed on a timescale of around one day. However, the lifetime of CO is extended when taking into account shielding effects from atomic carbon [93] (C, as produced by CO photodissociation), molecular hydrogen (H_2), and CO itself (self-shielding), which prevent UV photons from penetrating into the ring. Self-shielding alone, in the warm-temperature, low-CO-mass scenario, extends the gas lifetime by around two to four years. Given the lack of observational constraints on C

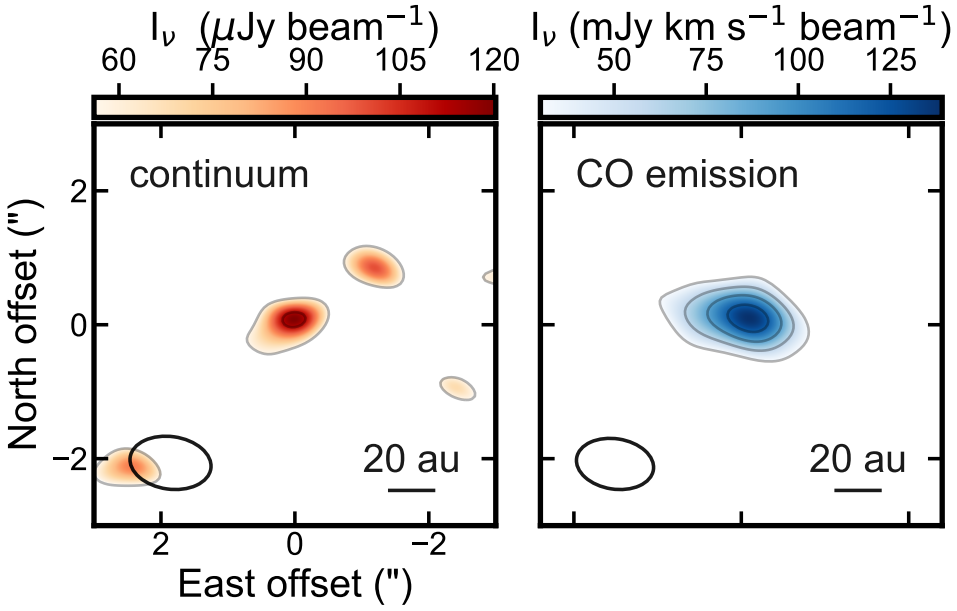

Figure 4-1: Cleaned emission maps of the HD 172555 system. Left: 4σ detection of the dust continuum emission (surface brightness I_ν). Right: The moment-0 (spectrally integrated surface brightness I) map of the CO $J = 2-1$ transition, with 9σ detection. Contour levels are at 2σ levels, with σ being 0.029 mJy per bean and 15 mJy km s^{-1} per beam for the continuum and CO moment-0 maps, respectively. The beam size is denoted in the lower left corner of each panel. Note that the 2σ peaks are background noise and not significant.

and H_2 column densities, we cannot definitively estimate the shielding and hence the CO destruction timescale. However, Co could have easily survived over the system age (23 Myr), both in a scenario where C and CO dominate the gas mass (C/CO ratio of $> 0.16 - 0.43$; Methods) and in a H_2-dominated scenario (H_2/CO ratio of around $> 10^5$). Therefore, CO could either be the result of a very recent production and/or replenishment mechanism, or have survived for a large fraction of the system age.

The CO detection constrains the gas to be located in the roughly 6-9 au region of

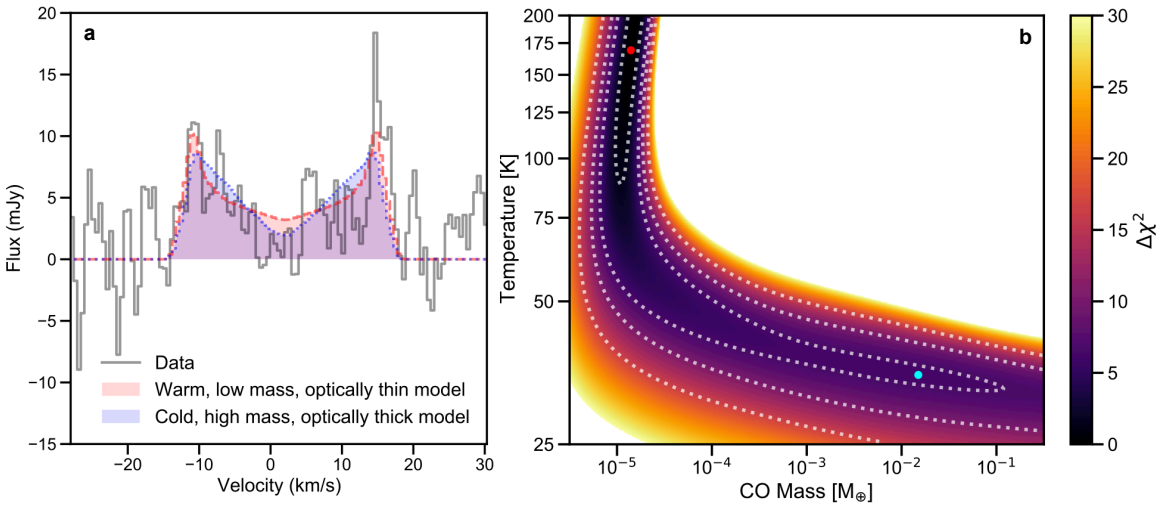

Figure 4-2: Mass-temperature degeneracy of the CO data. **a,** CO $J = 2-1$ spectrum of HD 172555 (grey solid line), compared with the output of two radiative transfer models: a low-mass, warm-temperature CO model (red dashed line), and a high-mass, cold-temperature CO model (blue dotted line). **b,** χ^2 map (where χ^2 is relative to the best-fit model) showing a clear CO temperature-mass degeneracy for models that are good fits to the data (darker on the colour scale). The red and light blue dots correspond to the red (warm) and blue (cold) CO models shown in **a**. Dotted contours enclose models that are consistend with the data at the $> [1, 2, 3, 4]\sigma$ confidence level.

the HD 172555 planetary system, co-located with the dust [55]. Accounting for the difference in luminosity between the Sun and HD 172555, this region corresponds to the same thermal conditions as at about 2.1-3.3 au - the asteroid belt region - in our Solar System. This makes the presence of Co, a highly volatile gas with sublimation temperatures as low as 20 K, extremely surprising in a system with age 23 Myr. Some physical mechanism must explain the presence of gas and dust in the outer terrestrial planet-forming region of HD 172555. We test four hypotheses for the origin of the debris, and examine them in light of existing evidence from both dust observations and from the ALMA detection of CO in the system. These scenarios are: (1) leftover gas and dust from a primordial, protoplanetary disk; (2) collisional production with an extrasolar asteroid belt; (3) inward transport of material from an external reservoir; and (4) release in the aftermath of a giant impact between planetary-sized bodies.

Young A-type stars are born surrounded by protoplanetary disks of primordial gas and dust, but only 2-3% survive beyond the first 3 Myr of a star's lifetime [89, 211].

Even if the CO observed around HD 172555 were primordial, with its lifetime extended through shielding, the system would remain a remarkable outlier not only in age (at 23 Myr old) but also in dust mass (orders of magnitude lower than protoplanetary disks [202]) and in radial distribution of CO and dust (constrained within 10 au, and with a CO cavity, in contrast to protoplanetary disks typically extending out to tens/hundreds of astronomical units [79, 17]). The extreme depletion in dust mass would require efficient dust removal, either through accretion onto the star or grain growth [202]. At the same time, the confined radial extend would require interior/exterior truncation, for example, by as-yet-undiscovered companions. Finally, the peculiar dust mineralogy of HD 172555 (requiring energetic processing) is seldom seen in young protoplanetary disks, although it may have arisen in nebular shocks analogous to those that could have led to chondrule formation in the Solar System [137]. In conclusion, a primordial scenario would make HD 172555 an extreme outlier among other protoplanetary disks, favouring instead second-generation production.

In the second-generation case, a steady-state collisional cascade within an asteroid belt can explain the dust mass detected in the system [186], but not its abnormally steep particle size distribution [83], or its mineralogy requiring high-energy collisions at velocities higher than expected within typical belts [105, 83, 29]. Although CO gas is commonly observed within collisional cascades in colder extrasolar Kuiper belt analogues at tens of astronomical units [130], there its presence can be explained by the release of CO gas initially trapped within icy bodies, or by desorption of CO_2 ice followed by rapid photodissociation of CO_2 gas [128, 113, 126, 94, 209]. This picture is not plausible at 7.5 au; studies of ice-bearing asteroids in the Solar System show that although retaining water ice in the deep subsurface is possible - explaining the presence of outgassing main-belt comets in the asteroid belt - CO and CO_2 cannot remain trapped at these temperature [164, 182]. In addition, any bodies forming at this location would be too warm to have formed with a substantial reservoir of CO or CO_2.

Alternatively, the observed dust and CO might originate from inward scattering of small bodies (exocomets) from an outer, cold reservoir akin to the Solar System's

Edgeworth-Kuiper belt [114]. We first explore the possibility of gas and dust production through sublimation of Solar-System-like, 10-km-sized exocomets. We find that this scenario can reproduce the observations only if exocomets can be delivered on low-eccentricity orbits, finding that the exocomet replenishment rate could potentially be reconciled with the non-detection of an outer belt (Methods). However, this scenario cannot explain the relatively narrow radial distribution of the CO ring, or the mineralogy of the observed dust, and is thus not likely. However, it is possible that a single, cold, massive icy body is scattered inwards from an undetected outer belt. To produce the observed, largely axisymmetric distribution of material and dust mineralogy, the icy body would need to undergo a giant impact and release its CO or CO_2 content. Assuming a 25% CO + CO_2 ice mass fraction, and complete ice release at impact, we find that a dwarf planet (at least half the size of Pluto) would be needed to produce the (lower limit on the) CO gas mass observed.

Finally, CO gas and dust could be produced by a giant impact between planetary bodies formed in situ at around 7.5 au. The epoch of terrestrial planet formation, lasting from about 10 Myr to 100 Myr, is expected to be dominated by giant impacts. Within the Solar System, there is abundant evidence for the occurrence of giant impacts; the iron enrichment of Mercury [13, 28], the formation of the Moon [22, 23, 125], the Martian hemispheric dichotomy [117, 148], and the retrograde rotation of Venus [44] are all hypothesized to have their origins in giant impacts. The HD 172555 system, at 23 Myr, is at the expected age that terrestrial planet formation proceeds through giant impacts; the dust and gas observed in the system are located in a region that is analogous to the terrestrial zone in our own Solar System. Studies of post-impact dynamics allow us to set constraints on progenitor masses and time since impact by considering the current spatial distribution and mass of dust (Methods). The dust in the system is axisymmetric within observational uncertainties, implying that the time since impact is at least the debris symmetrization timescale, which at 7.5 au is of the order of about 0.2 Myr [205]. The width of the dust debris, as resolved at shortwer wavelengths [180, 55], suggests a progenitor mass of the order of about $8M_{\oplus}$, although the exact value is dependent on the radial width of the dust

debris (Methods). Impacts between such bodies produce debris that would survive encounters with leftover planets, on a timescale longer than symmetrization; this indicates that impacts of such planets could be responsible for the observed, long-lived debris field.

Further supporting this scenario, we find that the optically thin CO gas mass detected in the system ($0.45 \times 10^{-5} M_{\oplus} - 1.21 \times 10^{-5} M_{\oplus}$, or about ten times the mass of Earth's atmosphere) is consistent with post-impact release from a planetary atmosphere. We note that any CO_2 in a planetary atmosphere will rapidly be converted into observable CO if liberated from the atmosphere, as CO_2 cannot be substantially shielded by C in the same way as CO because its photodissociation bands extend further towards the optical [71]. Simulations show that up to 60% of a modestly sized, heavy atmosphere can be stripped in the initial shock of an impact [173, 88]. We find that the observed CO mass as well as the C needed to shield the CO for at least the symmetrization timescale require the release of an amount of CO_2 corresponding to just 9-23% of the total present in the Venusian atmosphere [99]. More (less) massive planets with similar heavy atmospheres would require a smaller (larger) fraction of the atmosphere removed, or a smaller (larger) abundance of CO and/or CO_2. For ligher, H_2-dominated atmospheres, longer-term thermal effects can result in the stripping of the entire atmospheric envelope [14], in which case, once again, an amount of CO and/or CO_2 consistent with the observations could plausibly be liberated.

The detection and morphology of CO gas, combined with previous evidence from dust imaging and spectroscopy, supports a picture where a giant impact took place at least 0.2 Myr ago in the outer terrestrial planet-forming region of the 23-Myr-old HD 172555 system. Planetary-scale impacts are predicted to be commonplace in the latest stages of planet formation; the discovery of CO gas in the terrestrial planet-forming region, in amounts consistent with the expectation from atmospheric stripping, suggests that giant impacts may release not only copious, observable dust, but also detectable amounts of gas. Furthermore,the discovery reveals the importance of gas release in post-impact dynamics, and highlights the potential of using gas as a tool to search for giant impacts in nearby planetary systems, while providing a unique

window into the composition of young planets and their atmospheres.

4.2 Methods

4.2.1 ALMA observations

We analysed archival data from the ALMA telescope taken during cycle 1 in band 6 (project code 2012.1.00437.S). The observations were performed with the 12-m array in a compact antenna configuration. the on-source time was 76 min. The spectral setup included four spectral windows, of which three were set up in time-division mode for continuum observations and centred at 213 GHz, 215 GHz, and 228 GHz. One window was set in frequency-division mode (with a high spectral resolution of 488.29 kHz) to target the ^{12}CO J = 2-1 line (rest frequency 230.538 GHz). We calibrated the visibility data using scripts provided by the ALMA observatory. The CASA (Common Astronomy Software Applications) software (version 5.6.1, `https://casa.nrao.edu/casadocs/casa-5.6.0`) was used for visibility imaging. For both the continuum and the CO line emission, we removed data from antennas 7, 19, and 25. These data were taken in a hybrid configuration, with the three flagged antennas far from the compact group of antennas; removing these data substantially improves the imaging.

The CLEAN algorithm [74] was used to image both the continuum and CO line emission through the CASA 'tclean' task. To achieve maximum sensitivity, we used natural weighting for both datasets, resulting in a synthesized beam size of 1.16" × 0.75", corresponding to 32.9 au × 21.3 au at the system distance (28.5 pc) and a position angle of 81°. Before line imaging, we subtracted the continuum (measured in line-free regions of the spectrum) in visibility space using the CASA 'uvcontsub' task. We then imaged the CO to produce a cube with frequencies within ±25 MHz of the rest frequency, corresponding to velocities within ±30 km s^{-1} of the radial velocity of the star. The data were imaged at the native spectral resoluution (twice the original channel width) of 488.29 kHz. To obtain the CO moment-0 map, shown in 4-1, we

integrated along the velocity axis between ±15 km s^{-1} of the stellar velocity.

The emission is spatially unresolved in both the continuum and CO images, which have root-mean-square noise levels of 0.029 mJy per beam and 26 mJy km s^{-1} per beam, respectively. This yields a peak detection at a signal-to-noise ratio per beam of 4 and 9 for the continuum and CO J=2-1 spectrally integrated emission, and total fluxes of 0.12 ± 0.03 mJy and 170 ± 30 mJy km s^{-1}, respectively. Note that the flux calibration is expected to be accurate within 10%; this uuncertainty was added in quadrature to obtain the quoted errors (`https://almascience.nrao.edu/documents-and-tools/cycle-1/alma-ot-reference-manual`). Both the CO gas and continuum dust emission centroids are consistent with the Gaia proper-motion-corrected position of the system [166, 21]. The literature [180] values for the dust location in astronomical units have been corrected to account for the new Gaia distance to the star compared with the previous Hipparcos distance. To extract a one-dimensional spectrum from the data cube, we integrate within a circular mask of radius $2.5\sigma_{beam}$ (with σ_{beam} being the standard deviation of the two-dimensional Gaussian beam, averaged between the major axis and the minor axis).

4.2.2 Millimetre dust mass

To calculate the dust mass, we assuume that the dust grains act as blackbodies and emit according to their Planck function at a temperature of 169 K. Assuming the dust is optically thin, the total dust mass can be calculated from the observed flux density $F_\nu = 0.12 \pm 0.03$ mJy, when accounting for the stellar contribution. This contribution is estimated to be 0.035 mJy at 230 GHz from our best fit PHOENIX stellar model fitted to optical and near-IR photometry (see 'Optically thin CO mass calculation' below). PHOENIX models have been shown to be a good fit to millimetre-wavelength photometry of Sirius A [196], which has a similar spectral type to HD 172555. Subtracting this stellar contribution to the detected millimetre emission yields a contribution due to dust of85 ± 30 μJy. The dust grain opacity is assumed to be 10 cm^{2}g^{-1} at 1000 GHz, and scaled to the frequency of the observation with an opacity power-law index of $\beta = 1$ [11]. These assumptions yield a dust mass of $(1.8 \pm 0.6) \times 10^{-4} M_\oplus$.

4.2.3 Optically thin CO ring modelling

To model the velocity spectrum expected from a circular orbiting ring or disk of material, we calculate Keplerian velocities assuming a stellar mass of $1.76 M_{\odot}$ [43]. Two-dimensional orbital velocity vectors are calculated for a radial and azimuthal grid, assuming a vertically thin ring/disk of gas that has radially and azimuthally uniform surface density between an inner boundary and an outer boundary. They are transformed to the sky plane using the ring/disk inclination to obtain radial velocities along the line of sight. These velocities in the reference frame of the star are then added to the radial velocity of the star in the barycentric frame (left as a free parameter) to obtain barycentric velocities as observed by ALMA. A histogram of these velocities, with the same binning as the observed data, serves as a model spectrum. We normalize the unitless spectrum such that the integral of the spectrum is equal to the integrated flux of the line, a free parameter in the fit. This spectrum is then convolved with a Gaussian of full-width at half-maximum equal to twice the channel width to reproduce the spectral response of the instrument due to Hanning smoothing (`https://safe.nrao.edu/wiki/pub/Main/ALMAWindowFunctions/Note_on_Spectral_Response.pdf`). In addition to these parameters, the model fits the inclination, radial location of the midpoint, and width of the ring/disk.

A Markov chain Monte Carlo (MCMC) approach was used to determine the best fit to the data. We used the Python package emcee[58]. The uncertainty in each velocity bin was assumed to be equal to the root mean square measured in the region of the spectrum outside the detected emission. Flat priors were applied for the radial location, width, integrated line flux, and stellar velocity. A Gaussian prior was applied to the inclination, assuming the gas shares the same inclination as the dust disk, as determined from previous resolved imaging [55]. We carried out an additional run where a flat prior was applied to the inclination, to confirm the assumption of shared inclination. Extended Data 4-3 shows the posterior probability distributions of the parameters obtained from our MCMC runs and Extended Data Table 4.1 indicates the best-fit values, obtained as the 50th $\pm$ 34th percentiles of the posterior distributions

of each parameter, marginalized over all other parameters. Best-fit values from both runs assuming a Gaussian or flat prior on the inclination are included.

Best fit parameters		
	Gaussian	Flat
Inclination (°)	$102^{6.0}_{6.5}$	$107^{12.1}_{17.6}$
Midpoint (au)	$7.4^{0.5}_{0.4}$	$7.4^{1.8}_{0.6}$
Width (au)	$3.4^{0.5}_{0.5}$	$3.1^{0.9}_{0.7}$
V_* (km/s)	$2.3^{0.2}_{0.2}$	$2.3^{0.2}_{0.2}$
Int. Flux (mJy km/s)	$122^{8.9}_{9.0}$	$122^{8.5}_{8.8}$

Table 4.1: Best fit values (50 ± 34 percentile) to the optically thin model of gas emission. Left column indicates values derived from the MCMC run where a Gaussian prior was applied to the inclination. Right column indicates values derived from the MCMC run where flat priors were applied to all model parameters.

4.2.4 Optically thin CO mass calculation

To derive a CO mass from the best-fit spectrally integrated line flux, we begin by assuming that the line is optically thin and considering the excitation conditions the gas may be subject to, which affect this conversion. We follow an existing framework [128], which considers that the energy levels of a CO molecule may be populated by collisions with other species (or by one dominant species, the main collisional partner), or by absorption and emission of radiation, giving rise to two limiting regimes, a radiation-dominated regime (at low gas densities) and a collision-dominated regime (local thermodynamic equilibrium (LTE) at high gas densities). The choice or density of collisional partners (in our case, electrons) does not affect the level populations in these two limiting regimes, and therefore the range of CO masses derived.

To account for the full range of excitation conditions, we therefore us a non-LTE code [128] to solve the statistical equilibrium equations and calculate the level populations. This includes the effect of fluorescence induced by stellar UV and IR radiation as seen by a CO molecule at 7.5 aum from the central star [129]. For the

star, we adopt a PHOENIX [78] model spectrum fitted to multiband opttical and near-IR photometry using the MultiNest code [57], as described in previous studies [177, 206]. This yields a best-fit stellar effective temperature of $T_{eff} = 7840 \pm 30$ K and luminosity of $L_* = 7.7 \pm 0.1 L_\odot$. The non-LTE calculation yields a formal range of possible CO masses between $0.45 \times 10^{-5} M_\oplus$ and $1.25 \times 10^{-5} M_\oplus$ for kinetic temperatures between 100 K and 250 K, encompassing the blackbody temperature of 169 K at 7.5 au.

4.2.5 Three-dimensional radiative transfer modelling

We use the RADMC-3D (`http://www.ita.uni-heidelberg.de/~dullemond/software/radmc-3d/`) radiative transfer code to check the impact of optical depth in more detail. We use the same ring geometry as obtained from optically thin fitting (Extended Data Table 4.1, Gaussian prior). We vary the input CO mass and kinetic temperature over a two-dimensional grid (Fig. 4-2), and connect the latter to the vertical aspect ratio by assuming a vertically isothermal gas disk with a mean molecular weight of 14 (that is, the gas mass is dominated by atomic C and O, as expected in a second-generation scenario). To sample the ring well spatially and spectrally, we create cubes of J=2-1 emission with a pixel size of 6 mas (corresponding to a physical scale of 0.18 au), and the same native channel width as our data. We then spectrally convolve with a Gaussian to reproduce the spectral response of the instrument and extract a one-dimensional model spectrum by spatially integrating the model emission. WE then compared this model spectrum to the data (as shown in Fig. 4-2) and calculated χ_2 for every mass and temperature in our grid, to obtain a χ_2 map (Fig. 4-2).

4.2.6 CO survival lifetime against photodissociation

The observed CO gas in the circumstellar environment around HD 172555 will be subject to photodissociation from the stellar and interstellar UV field. The photodissociation rate in s$^-$1 of a molecule in a radiation field $I(\lambda)$ is $k = \int \sigma(\lambda) I(\lambda) d\lambda$, wher λ is the wavelength, and $\sigma(\lambda)$ is the photodissociation cross-section in cm^2. We use the CO

photodissociation cross-sections from the Leiden database [71] (`https://home.strw.leidenuniv.nl/~ewine/photo/display_co_42983b05e2f2cc22822e30beb7bdd668.html`). We adopt the stellar spectrum from the optically thin mass section above, scaled to the centre of the gas ring (7.5 au) to obtain the stellar radiation field. We find that the star dominates over the interstellar radiation field, and that the CO photodissociation timescale (1/k) at the ring's radial location is approximately one day. The shielding effects are estimated using pre-computed shielding constants [71]; we interpolate the constants for stars of 4000 K and 10000 K to a stellar temperature of 8000 K, closest to the effective temperature of HD 172555. The CO column density is calculated from the centre of the ring along the line of sight to the star, using our best-fit uniform ring model parameters. To find the H_2 and C column densities that provide sufficient shielding, we interpolate the shielding constants along the column-density axis and find the column density required.

4.2.7 Delivery from an outer belt

Replenishment requirement

We consider a scenario where the dust grains and CO gas are produced from sublimation-driven release by Solar-System-like comets entering the inner region of the HD 172555 system. This requires replenishment of the observed total dust mass (in grains up to centimetres in size) on timescales comparable to their removal (assuming steady state). We assume that their removal is dominated by collisions, setting up a cascade down to the smallest grains (of size approximately 3.5 μm for a grain density of 2700 kg m^{-3}) that are then removed by radiation pressure from the central star, to derive a mass-loss rate of $2.2 \times 10^{-2} M_{\oplus}$ Myr^{-1} (using equation (21) in ref. [126]). We neglect the effect of gas drag, assuming that the larger, centimetre grains are unaffected.

We use the results of thermochemical modeling [112] calibrated on Solar System comets to estimate the mass-loss rate per unit surface area of an exocomet at 7.5 au around 7.7 $L_{\odot}$ to be 5.6×10^{-6} kg m^{-2}s^{-1} of dust in grains up to centimetres in size. Dividing by an assumed bulk density of 560 kg m^{-3}, and assuming a 1:1 dust/ice

ratio, this corresponds to an erosion rate of 0.62 m yr^{-1}. Therefore, a comet with a 10-km radius will be emitting dust at a rate of 7040 kg s^{-1} ($3.72 \times 10^{-8} M_{\oplus}$ Myr^{-1}) and will survive (if continuously sublimating at this rate) for about 16 kyr.

High-eccentricity exocomet population

In the first case, we assume exocomets arise from a yet-undetected belt at 100 au (a typical location of cold exocometary belts around A stars [127]) and approach the inner regions on eccentric orbits. The velocity distribution from the observed CO emission implies line-of-sight velocities for the gas of about 14.5 km s^{-1}, corresponding to 7.5 au for circular orbits around HD 172555. However, these velocities will be achieved at larger radii for comets with non-zero eccentricities, random pericentre directions and orbiting in the same plane as the inner system of HD 172555. The pericentre distance corresponding to pericentre velocities of about 14.5 km s^{-1} will increase with the apocentre (and therefore the eccentricity) of the orbits; for an apocentre of 100 au, we derive a pericentre distance of 13.2 au. Therefore, we expect gas released from exocomets on these orbits to be located at and beyond about 13.2 au from the central star. For comparison, this is 80% larger than the radial location derived for circular orbits (7.5 au). However, eccentric exocomets with the observed velocities would produce a CO ring with diameter about 26 au (0.9"), which is comparable to the resolution element of our observations, implying that the ring would have been marginally resolved, which is not the case. In addition, scattered light observations strongly constrain dust emission to less than 0.9" (3σ) diameter, with a sharp outer edge. The fact that the expected radius of a CO ring would significantly exceed the observed value makes the eccentric exocomet scenario inconsistent with the available observations. Note that reasonably changing the apocentre location, and therefore the radius of the hypothetical cold belt where the exocomets originate, does not alter our conclusions significantly. For example, assuming an outer belt location of 20 au instead of 100 au implies exocomet pericenters at 10 au. This would produce CO emission with a minimum expected diameter of 20 au (0.7") and extending much beyond it, which probably would have been spatially resolved in the ALMA data.

Low-eccentricity exocomet population

In the second case, we assume exocomets are being continuously scattered inward from an outer belt by a chain of low-mass planets, undergoing multiple scatterings and producing a low-eccentricity comet population at about 7.5 au. We here assume circular orbits for simplicity. The dust observed requires replenishment at a rate of $2.2 \times 10^{-2} M_{\oplus}$ Myr^{-1}. Assuming exocomets of 10 km in size with an exocometary dust release rate of $3.72 \times 10^{-8} M_{\oplus}$ Myr^{-1}, 5.9×10^{5} exocomets are required to be sublimating at around 7.5 au at any point in time. For a bulk density of 560 kg m^{-3}, this corresponds to $2.3 \times 10^{-4} M_{\oplus}$ in 10-km exocomets. While sublimating at this rate, such an exocomet would survive for about 16 kyr, so comets would need to be resupplied by inward scattering to the inner planetary system at a rate of $1.4 \times 10^{-5} M_{\oplus}$ yr^{-1}. Inward scattering is an inefficient process; simulations maximizing inward scattering by chains of low-mass planets indicate that only a few per cent of comets encountering an outermost planet make it into the inner regions, as the vast majority are ejected [116]. Therefore, higher supply rates of the order of about $10^{-6} M_{\oplus}$ yr $^{-1}$ from a putative outer belt are probably needed, which would imply that a currently undetected outer belt would have resupplied 23 $M_{\oplus}$ in 10km exocomets into the inner regions over the 23 Myr age of the system.

We can compare this to the upper limit on the presence of an outer belt at 100 au from our ALMA data. Assuming blackbody temperatures, and the same dust opacity as used for dust in the inner regions, we derive an upper limit of less than $1.8 \times 10^{-3} M_{\oplus}$ (3σ) on the mass of solids up to centimetre sizes. Extrapolating from centimetre-sized grains up to 10-km exocomets (assuming a size distribution with a constant power-law slope of -3.5), we obtain an upper limit on the total mass in 10-km sized exocomets of less than $1.8 M_{\oplus}$ (3σ). Therefore, the current mass of the outer belt would be at least a factor of about ten smaller than the mass that has been removed from the belt over its lifetime, which is by itself not impossible.

However, it is likely that exocomets reaching their inner regions would retain some eccentricity, which would prolong their survival (lower sublimation rates) and

also potentially make the gas velocity distribution inconsistent with the observations. In addition to that, the narrow CO radial distribution is in tension with production rates of Co as a function of heliocentric distance in sublimating Solar System comets [15], which show no clear enhancement in production rates at radii whose thermal conditions are comparable to that of HD 172555. Although inward scattered, sublimating exocomets could produce a steeper-than-collisional size distribution of grains, down to sizes smaller than the radiation pressure blow-out limit, they would not be able to reproduce the peculiar dust mineralogy indicative of the energetic processing typical of hypervelocity impacts, unless exocometary impacts in the inner regions contribute, and/or are the source of the dust and gas observed. In conclusion, sublimating exocomets could be replenished in the inner system at high-enough rates to explain the observed dust emission, but are unlikely to explain the relatively narrow distribution of CO, and the dust mineralogy observed around HD 172555.

4.2.8 In situ giant impact constraints from axisymmetry and width of debris

Observations of both CO and dust [180, 55] are consistent with the CO and dust distribution being axisymmetric. Because of this, the time since impact must be at least the symmetrization timescale, which is on the order of a few tens of thousands of orbits [205] (about 0.2 Myr at 7.5 au). Constraints on the planet mass can be derived from the width of the debris, as a proxy for the velocity dispersion of released material. The width, dr, is given by d$r = 2re_p$, where e_p is the proper eccentricity of the orbiting debris [201]. This eccentricity is related to the velocity dispersion, σ_v, through $\sigma_v \approx \sqrt{1.5}e_p v_k$, where v_k is the Keplerian velocity at the given semimajor axis. We assume the velocity dispersion is related to the escape velocity v_{esc} at the surface of the colliding bodies [205] by $\sigma_v \approx 0.46 v_{esc} \approx 0.46\sqrt{\frac{2GM_p}{R_p}}$, where G is the universal gravitational constant, and R_p is the planetary radius. Thus, for an observed debris width dr, a planet of mass $M_p \approx 103\frac{m_*^{3/2}}{\rho_p^{1/2}}\left(\frac{dr}{r^{3/2}}\right)^3$ in $M_\oplus$ is expected, where ρ_p is the planet's bulk density in g cm^{-3}, M_* is the stellar mass in $M_\oplus$, and both r and

dr are in astronomical units. If the planetary bodies colliding have rocky, Earth-like compositions, they will have bulk density of about 5.5 g cm^{-3}. We assume that the solid debris is confined to the same radial width as the dust width derived from mid-IR Q-band imaging [180], which finds d$r_{dust}/r \approx 1.2$, where dr_{dust} is the width of the dust ring. These assumptions yield a planetary mass on the order of about $8M_{\oplus}$. We note that the mid-IR imaging is sensitive to small grains whose width might have been broadened due to radiation pressure from the central star; if radiation pressure inflated the width compared with that expected from the velocity dispersion, the planetary mass involved would be reduced. If instead the bulk planetary density is lower, the mass of planet involved in the collision would be larger.

4.2.9 Constraints from debris survival

Progenitor mass constraints must also be considdered in the context of debris survival; the observed debris must survive encounters with a leftover planet in the time since impact. We conservatively assume that the mass of the largest product of the impact is on the order of the mass of the impact progenitors, and consider the outcome of encounters between debris and a surviving planet [200]. Given an assumed planetary density similar to that of the Earth, and a semimajor axis of 7.5 au, we first note that for a leftover planet with mass below about $1.8M_{\oplus}$, the predominant (eventual) outcome of an encounter will be accretion, whereas for masses above that threshold, the predominant (eventual) outcome will be ejection. However, timescales of accretion and ejection have a role in debris survival. These timescales must be at least as long as the symmetrization timescale (0.2 Myr) to ensure that the debris produced in an impact could be seen in the symmetrical structure observed today. For progenitor masses in the range derived from the debris width constraints above, the reaccretion and ejection timescales are much longer than the symmetrization timescale. Therefore, giant impact debris at 7.5 au is expected to survive encounters with leftover planets with masses on the order of $8M_{\oplus}$, as large as those of the progenitors, on a timescale longer than the symmetrization timescale.

4.3 Acknowledgments

Material from: Schneiderman, T., Matrà, L., Jackson, A.P., Kennedy, G.M., Kral, Q., Marino, S., Öberg, K.I., Su, K.Y.L, Wilner, D.J., Wyatt, M.C., "Carbon monoxide gas produced by a giant impact in the inner region of a young system", Nature, published 2021, Springer Nature

T.S. led the optically thin modelling and discussion. L.M. led the radiative transfer modelling. T.S. and L.M. were involved in data reduction, processing, and writing of the manuscript. All authors contributed to discussions of the results and commented on the manuscript.

We are grateful to J. Biersteker for discussions on the liberation of atmospheres in the aftermath of giant impacts. This paper makes use of ALMA data `ADS/JAO.ALMA#2012.1.00437.S`. ALMA is a partnership of ESO (representing its member states), NSF (USA) and NINS (Japan), together with NRC (Canada), NSC and ASIAA (Taiwan) and KASI (Republic of Korea), in cooperation with the Republic of Chile. The Joint ALMA Observatory is operated by ESO, AUI/NRAO and NAOJ. K.I.Ö. acknowledges support from the Simons Foundation (SCOL #321183). G.M.K. is supported by the Royal Society as a Royal Society University Research Fellow.

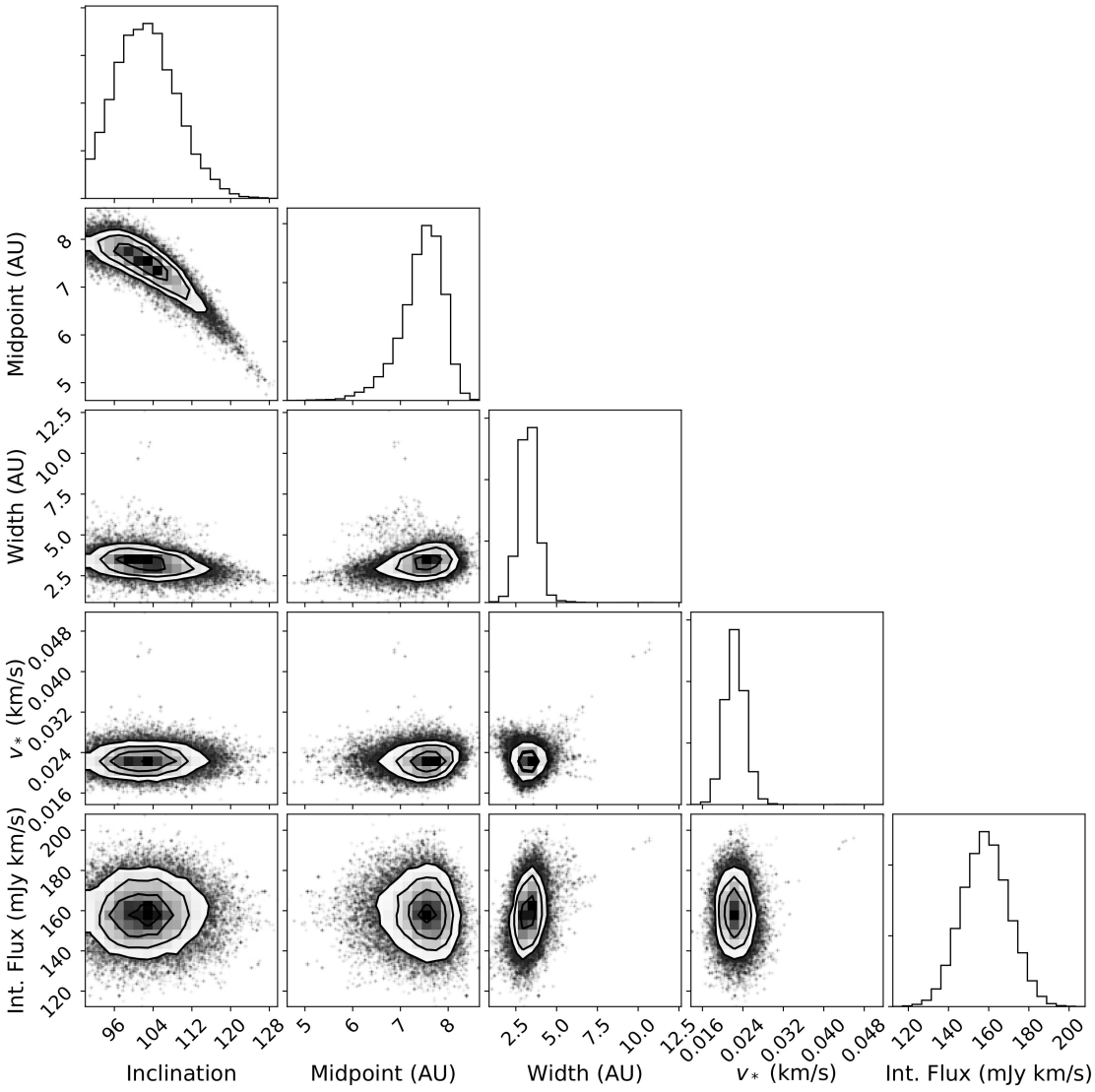

Figure 4-3: Posterior probability distributions for the model parameters obtained from the emcee fitting process. All parameters are well constrained, with best-fit values listed in Extended Data Table 4.1. This model was fitted to spectral data retianing original channel widths, assumed a Gaussian prior on the inclination, and assumed a stellar mass of $1.76 M_{\odot}$

Chapter 5

Simulation of multibandpass spectra of known, highly-inclined debris disks

5.1 Introduction

Debris disks are the natural outcome of planet formation, as they are composed of the remnant planetesimals that constituted the protoplanetary disk. Disks are tracers for the history of an individual system: the composition of dust in disks yields information about the primordial matter that was available for planet formation. In addition, the particle size distribution of dust grains in the system yields information about the history of planetary bodies.

Dusty debris disks are second-generation; the dust observed in circumstellar disks is often attributed to origin in a steady-state collisional cascade [204][203][199]. However, departures from the canonical steady-state particle size distribution indicate that a history of giant impacts may be at work in the system, as seen in [176, 83, 105]. Disks are also stirred and shaped by the presence of extant planets; interactions between the parent planetesimal bodies and planets in the system are expected to lead to dust production, which may lead to the bright disks seen at earlier ages, as in [90, 20, 144].

Debris disks are most often discovered through excesses in the spectral energy distributions of their host stars [54]. For many of the brightest disks, additional

characterization is possible; many disks have been imaged via the Hubble Space Telescope (HST) [174], ground-based observatories such as SPHERE and GPI, and the Atacama Large Millimeter Array (ALMA). Work such as [171] indicates that to fully understand the characteristics of a debris disk, multi-bandpass characterization is required. Indeed, [171] show that the fits to compositions for the HR 4796 A system are dramatically different when considering only scattered light as opposed to thermal emission from dust. Instead, they find that the best fits to available data occur when the system is examined in context, with all wavelengths fitted simultaneously. The consideration of scattered light only allows for a much wider range of silicate compositions, as well as iron compositions and carbonaceous compositions to fit the data. In contrast, fitting of only the thermal data yields exclusively carbon compositions as good fits for the data. When considering both scattered and thermal light, the best fits are narrowed to a small range of silicate compositions.

This suggests that it may be necessary to undertake multi-bandpass characterization of known debris disks to better understand the particle size distributions and compositions of dust in these disks. Forward modelling of dust in debris disks can be computationally expensive, however. In advance of data from the James Webb Space Telescope (JWST), we seek to develop methods that will decrease the parameter space for disk modeling by providing a set of simulated spectra of nine known, highly-inclined debris disks for a range of dust compositions and particle size distributions. By implementing principal component analysis, we can develop preliminary metrics for characterization of disks.

In section 5.2 we discuss the motivation for the disks selected as part of this sample. In section 5.3 we discuss the methods used to simulate the scattered light and re-emitted absorbed radiation of dust in these disks. In section 5.4 we discuss the outcome of this modeling, while in section 5.5 we put these results into context and discuss additional work required.

5.2 Disk sample

Highly inclined disks (i.e disks that are close to edge-on) simplify the geometric problems of interpreting disks by effectively reducing the structure to a 1 dimensional point. This simplification can be made because debris disks are optically thin. Additionally, for edge-on systems, the ansae of the disk - i.e. the apparent extremities of the disk when viewed close to edge-on - are the brightest features in the disk, and light that is scattered from the ansae is scattered at an angle of $\pi/2$ radians into the direction of the observer. This geometric orientation allows the simplification to consider the disk spectrum as originating in the ansae. We set a minimum disk inclination of 60° relative to face-on as a lower bound on inclusion in the sample.

In addition to seeking out disks with high inclinations, we selected disks that have previously been imaged in visible wavelengths (whether through HST or ground-based observatories). Most of these disks additionally have ALMA data in the sub-millimeter, and most will be accessible to imaging via JWST. Only HD 139664 and HD 202917 lack data in ALMA bandpasses. The systems and stellar properties of the host stars included in the sample are listed in Table 5.1. Table 5.2 lists the properties of the debris disks in the sample, as well as relevant citations as to the disk properties and prior observations. These disks surround stars with spectral type ranging from K1V to A0V and encompass a broad range of system ages from 10 to 440 Myr. Further, the disks vary in their fractional luminosities as well as distanes from the star.

5.3 Methods

5.3.1 Overview of zodimap

The modeling of the dust spectra is done using *zodimap*, a new python package I have developed to calculate the scattered light and thermal emission spectra of dust grains. This package calculates single-scattering and emission under the assumption that the dust mass is optically thin; debris disks are characterized by optically thin dust across

Table 5.1: List of systems

System	L_* ($L_\odot$) †	Spec	Dist (pc)††	T_{eff} (K) †	Age (Myr)
HD 109573	25.7 ± 0.6	A0V	71.91	9788	∼10
HD 216956	16.6 ± 0.3	A4V	7.7	8617	∼440
HD 172555	7.8 ± 0.1	A7V	28.79	7844	∼23
HD 32297	8.2 ± 0.3	A0V	129.73	7757	<30
HD 15745	4.23 ± 0.04	F0E	71.99	6800	∼100
HD 15115	3.71 ± 0.03	F4V	48.77	6724	∼12
HD 139664	3.39 ± 0.03	F3V	17.39	6716	∼300
HD 202917	0.69 ± 0.01	G2V	46.85	5440	∼30
HD 92945	0.37 ± 0.01	K1V	21.54	5105	∼80

† Obtained via fitting †† GAIA Data Release 2

Table 5.2: Debris disk properties

System	Disk L_{IR}/L_* †	Inner Edge (au)	Outer Edge (au)	Disk i	Citation
HD 109573	$(44.3 \pm 0.7) \times 10^{-4}$	60	87	77.4	[171][118]
HD 216956	$(7.7 \pm 0.5) \times 10^{-5}$	100	140	65.9	[85][107]
HD 172555	$(5.2 \pm 0.1) \times 10^{-5}$	6	9	78	[55][176]
HD 32297	$(5.5 \pm 0.3) \times 10^{-5}$	78	122	88.7	[53][108]
HD 15745	$(18.9 \pm 0.4) \times 10^{-4}$	128	480	67	[84][174]
HD 15115	$(6.9 \pm 0.6) \times 10^{-5}$	92.2	85.8	85.8	[174][109]
HD 139664	$(12.5 \pm 0.9) \times 10^{-5}$	60	109	85	[86][174]
HD 202917	$(3.1 \pm 0.1) \times 10^{-4}$	55.4	68.6	68.6	[175]
HD 92945	$(6.8 \pm 0.2) \times 10^{-4}$	43	65	62	[61][115]

† Obtained via fitting

the electromagnetic spectrum [77]. Although this package is able to calculate the light scattered off of dust grains at any location around a central star, we use it to instead calculate the ansae spectra for the disks in this sample. The ansae spectra can be approximated by considering the light scattered off of and emitted from a grain at a single location; we model the spectra at the midpoint of the dust ring locations.

Both absorption and emission coefficients, as well as the scattering phase function, are calculated via Mie theory for a range of particle sizes and wavelengths through built-in functionality of *zodimap*. A selection of the Mie theory coefficients are validated through comparisons to the outputs of existing Mie theory codes. The use of Mie theory assumes that the dust particles are spherical. Although this is not likely to be accurate, this approximation is used in the literature elsewhere. It is also possible that the scattering for a suite of many irregularly-shaped grains with random orientations will average out to be the scattering for a collection of spherical particles.

From the Mie theory coefficients, the scattered flux can be calculated as

$$F = B_* \frac{R_*^2}{d^2} \pi Q_{sca} r_d^2 \phi \tag{5.1}$$

where B_* is the stellar emission, R_* is the stellar radius, d is the distance to the dust, Q_{sca} is the Mie scattering efficiency, r_d is the dust radius, and ϕ is the scattering phase function, as calculated from Mie theory.

We determine dust grain temperature by self-consistently balancing input and output radiation. The dust grain temperature allows us to calculate the thermal emission from a grain by taking into account the dust blackbody emission modified by the effective emitting cross section:

$$F = \frac{1}{4} B_d Q_{abs} r_d^2 \tag{5.2}$$

where B_d is the dust blackbody emission and Q_{abs} is the Mie absorption efficiency.

5.3.2 Model parameters

We adopt PHOENIX [78] model stellar spectra that have been fitted to multiband optical and near-IR photometry using the MultiNest code [57]. Stellar properties (i.e. distance, temperature, luminosity) that are adopted are listed in Table 5.1; the luminosity, temperature, and stellar radius are all best-fits from the MultiNest fitting. The dust properties adopted (location, inclination), as well as the references to those values, are listed in Table 5.2

We use 50 distinct particle sizes spaced logarithmically between 0.1 and 1000 μm. These particle sizes then are used in 48 particle size distributions, with power law slopes evenly spaced between -2.5 and -4.5. The canonical steady-state power-law exponent that arises from a collisional cascade is -3.5, so the power law slopes are chosen to provide a range above and below the steady-state predictions. We consider 2000 logarithmically spaced wavelengths between 0.1 and 28.5 μm, and an additional 500 logarithmically spaced wavelengths between 600 and 1400 μm. These

wavelengths are chosen to span Hubble Space Telescope (HST), James Webb Space Telescope (JWST) and Atacama Large Millimeter Array (ALMA) bandpasses.

The composition of dust in debris disks is going to be set by the composition of the planetesimals from which the dust originates. In disks of these ages, the presence of dust requires some secondary production mechanism, as small grains are blown out on timescales shorter than the system lifetime. Canonically, grains are thought to originate in steady-state collisional cascades [204] [203] [199]. We can look to the compositions of planetesimals and dust within the solar system to identify candidates for compositions of dust in other systems. We examine a total of 7418 compositions, calculated from mixtures of 18 root compositions (see Table 5.3) at various porosities (approximated with vacuum). The root compositions were selected in line with the compositions of [171]; they are representative of the constituents of comets and asteroids in the solar system (see [87, 165, 207]). The optical constants of mixed compositions were calculated with Bruggeman effective medium theory [147]. For single-component porous compositions, porosities ranging from 5-95% in increments of 5% are used. For two-component mixtures, mixing ratios ranging from 10-90% in steps of 10% are used. For two-component porous mixtures, each two-component mixture is blended with vacuum in mixing ratios from 10-90% in steps of 20%. These model parameters produce a set of 9 systems with 356064 sample spectra each.

5.3.3 Application of Principal Component Analysis

Principal Component Analysis (PCA) is a technique that reduces the dimensionality of large data sets by transforming the data into an orthogonal basis where each principal component explains decreasing amounts of variance in the data. We use the *sklearn* python package functions StandardScaler and decomposition.PCA to scale the data and compute the principal components for the full set of spectra for a given stellar system. We consider the first two components, which cumulatively explain 81% of the variance in the spectra.

Table 5.3: Root compositions and families

Family	Root composition
Olivine	astrosilicates[102], amorphous olivine[101], iron-poor olivine*,nominal iron olivine*, iron-rich olivine*, crystalline olivine[102]
Pyroxene	iron-poor orthopyroxene*, nominal iron orthopyroxene*, iron-rich orthopyroxene*, pyroxene**
Organics	amorphous carbon[208], organics*, organics[101]
Water ice	water ice*, water ice[103], water ice[195]
Iron	iron*
Troilite	troilite*

* T. Henning (`https://www2.mpia-hd.mpg.de/home/henning/Dust_opacities/Opacities/opacities.html`)

** Aigen Li, priv. comm

5.4 Results

First, we will examine general trends that can be observed in the spectra by examining illustrative cases of the variation across the parameter space of the model. Then, we will examine the results from PCA applied to the full set of spectra.

5.4.1 Selected spectra

In each of the figures 5-1, 5-2, 5-3, and 5-4, the spectra are shown as qualitative comparisons on a log-log scale. The x-axes represent the wavelength in microns, while the y-axes are an arbitrary scaling in flux. The curves are offset for ease of comparison. The purpose of these figures is to get a general idea of the parameter space explored in this work.

Figure 5-1 illustrates the variation in spectra between systems in this sample. The spectra shown are the ansae spectra for each system considering an astrosilicate dust composition [102] with a particle size distribution with power-law slope of -3.5. As

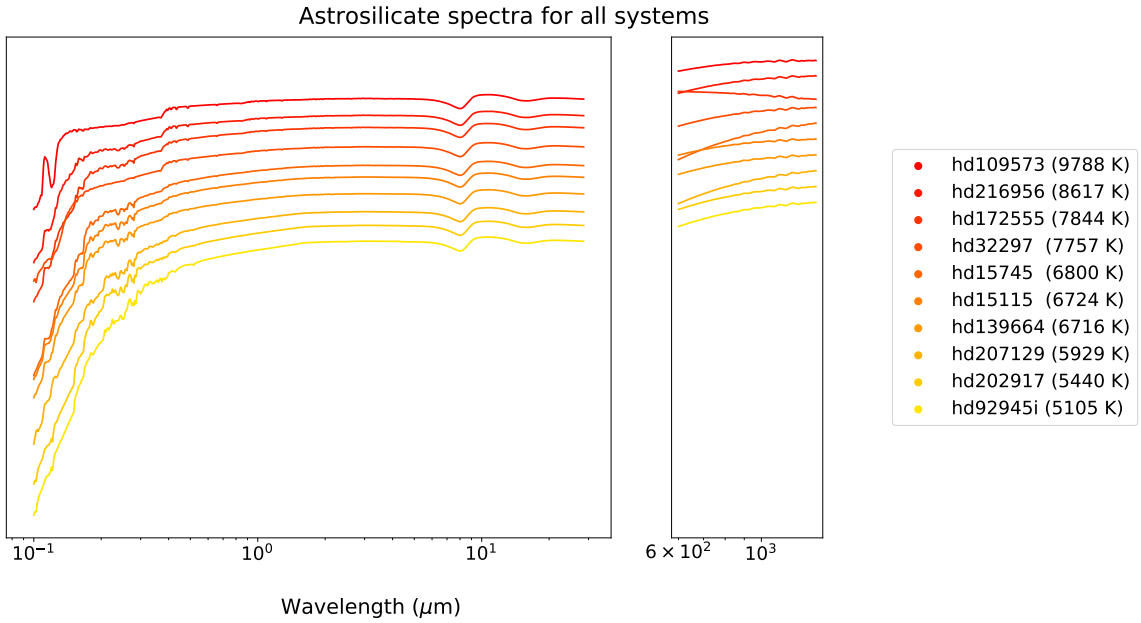

Figure 5-1: Spectrum for each system in our sample for an astrosilicate dust composition with a particle size distribution with power-law slope of -3.5. The spectra from top to bottom are in order of decreasing stellar temperature. The x-axis is the wavelength in micron, while the y-axis is an arbitrary flux in log-space, offset for clarity.

can be seen, the primary variation between systems is in the UV to visible wavelength range, where stellar features will be seen in the scattered emission. There is some variation in the slope of in the sub-millimeter to millimeter range.

Figure 5-2 examines the effect of increasing porosity on a sample spectrum. The spectra here are for the HD 109573 system with an astrosilicate dust composition with a PSD with power-law slope of -3.5. For the most part, there is little variation between spectra of increasing porosities. However, as the porosity increases beyond 75%, the slope of the spectrum in the ALMA bandpasses shifts from positive to negative. This is such a small shift, however, that it is unlikely to be detected when observational uncertainties are taken in to account.

Figure 5-3 examines the effect of altering the power-law slope of the particle size distribution from -4.5 to -2.5 The canonical steady-state power-law slope in a debris disk is -3.5 In principle, the spectrum should change with changing PSD. However, it is quite apparent from this figure that the models we have produced do not change.

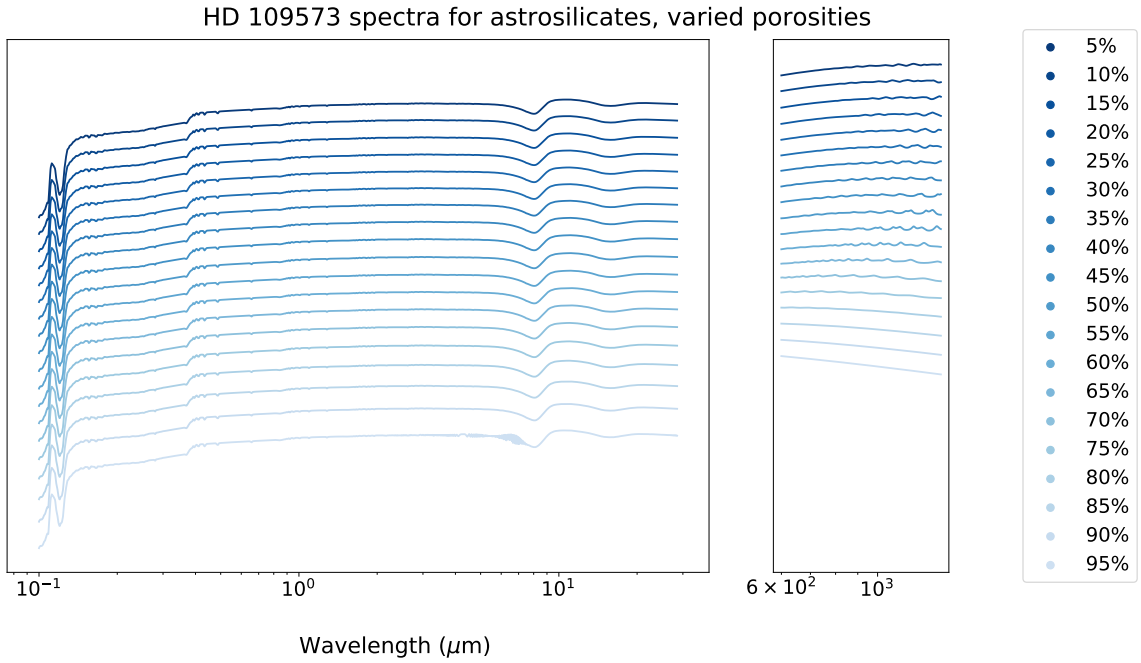

Figure 5-2: Spectra for the HD 109573 system for an astrosilicate dust composition with a particle size distribution with power-law slope of -3.5. The spectra from top to bottom are in order of increasing porosity.The x-axis is the wavelength in micron, while the y-axis is an arbitrary flux in log-space, offset for clarity.

This is likely an artifact of the model. As the particle sizes chosen are log-spaced, there is an additional disproportionate weight placed on small particles, as there are more constituting the spectrum. Further work is required to ensure that the simulated spectra adequately reflect an altered particle size distribution.

Figure 5-4 examines the spectra for the 18 root compositions considered in this sample. The displayed spectra are from the HD 109573 system, with a PSD power-law slope of -3.5. This is the parameter space where we see the most variation in spectra. It is not useful to look at the features in the sub-millimeter. Spectral features here, beyond the general slope of the spectrum, are artifacts of Mie theory, and result from a lack of the largest particle sizes. These features are expected to disappear with an increase in the maximum particle size. The silicates (green and orange color families) show features in the same region of the spectrum; water ice (blue color family) has features in an overlapping region, although additional features that do not overlap with the silicates exist. Carbonaceous species and iron-bearing species

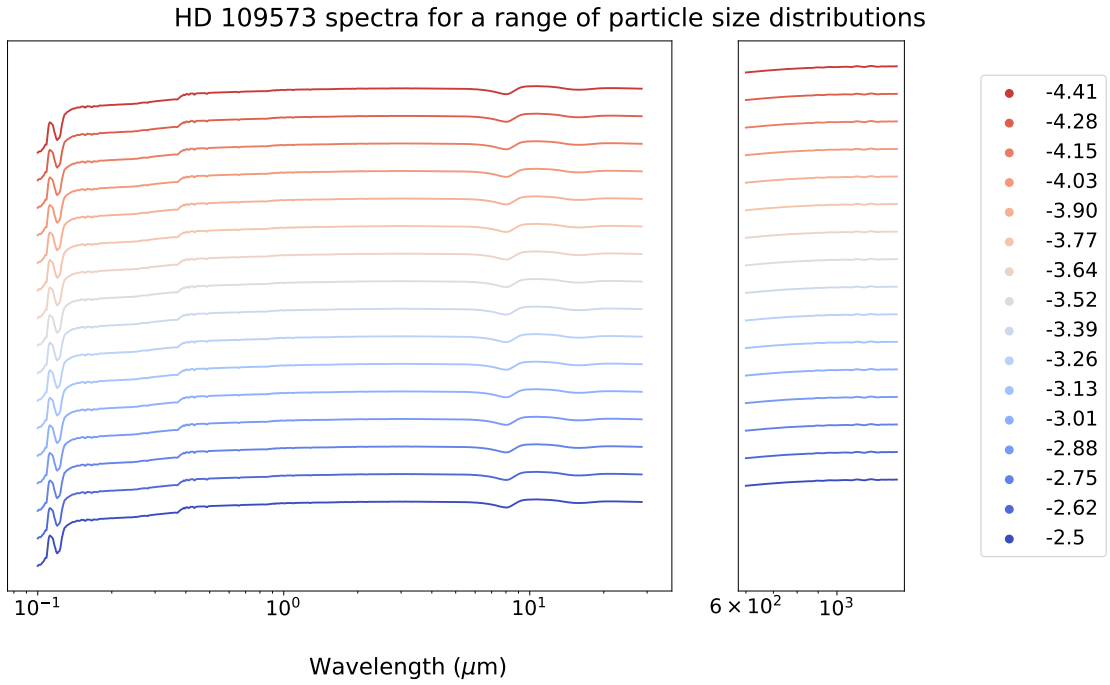

Figure 5-3: Spectra for the HD 109573 system for an astrosilicate dust composition. The spectra from top to bottom are in order of increasing power-law slope.The x-axis is the wavelength in micron, while the y-axis is an arbitrary flux in log-space, offset for clarity.

have few discernible spectral features. These qualitative results suggest that it will be difficult to differentiate specific silicate compositions without finely-resolved spectra.

5.4.2 PCA

The principal component analysis can be seen in Figure 5-5. The x and y axes correspond to the first two principal components, and each dot represents the location in PC-space of a single spectrum for the HD 109573 system. Initial analysis has not yielded a physical explanation for the origin of variation in the first two principal components. The colors of the points correspond to the compositional families described in Table 5.3, with the olivines and pyroxenes treated as a monolithic 'silicate' class (represented in yellow), and the iron and troilite identified as iron-bearing (represented with red). Water is represented in blue, and carbon in black. Mixtures between these components are captured as blends of these four base colors, with the

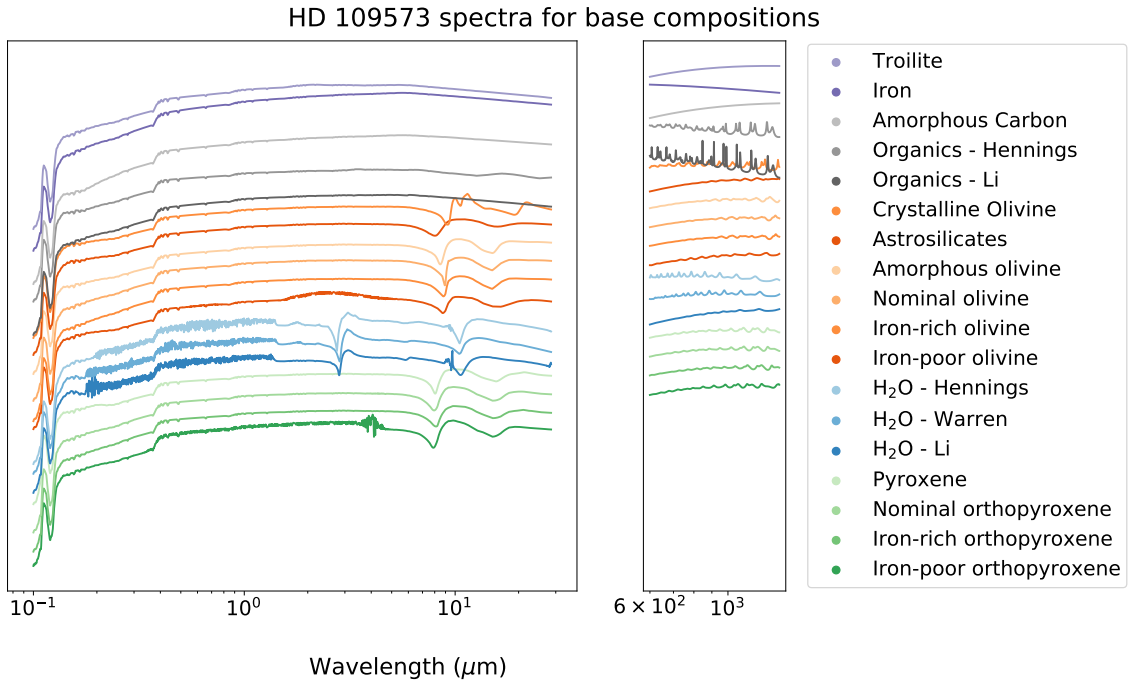

Figure 5-4: Spectra for the HD 109573 system with a particle size distribution with power-law slope of -3.5. The spectra are of the root compositions in the sample, with families of compositions illustrated in the same color family. Greens correspond to pyroxene compositions, blues to variations of water ice optical constants, oranges to silicates, blacks to organic/carbon-based compounds, and purple to iron-bearing compounds.The x-axis is the wavelength in micron, while the y-axis is an arbitrary flux in log-space, offset for clarity.

vacuum porosities captured in the opacity of the marker.

Principal component analysis should group together spectra that are similar to each other. In this iteration of PCA, we see that water, silicates, and carbon all group together in PC-space, with iron-bearing species forming two wings (left panel, Figure 5-5). Mixtures of these compositions fill out spaces between them. There is some separation in water, silicates, and carbon (see Figure 5-5); the separation is made more complicated as mixtures of compositions result in spectra that appear to be more similar to one another. The same trends observed in the HD 109573 PC analysis emerge for the other 8 disks in our sample. This figure follows the same format as Figure 5-5, with the exception that porosity is not reflected in the marker opacities. HD 172555 clusters in a way that diverges from the other disks, as the carbonaceous compositions extend further up along the second principal component axis. This is

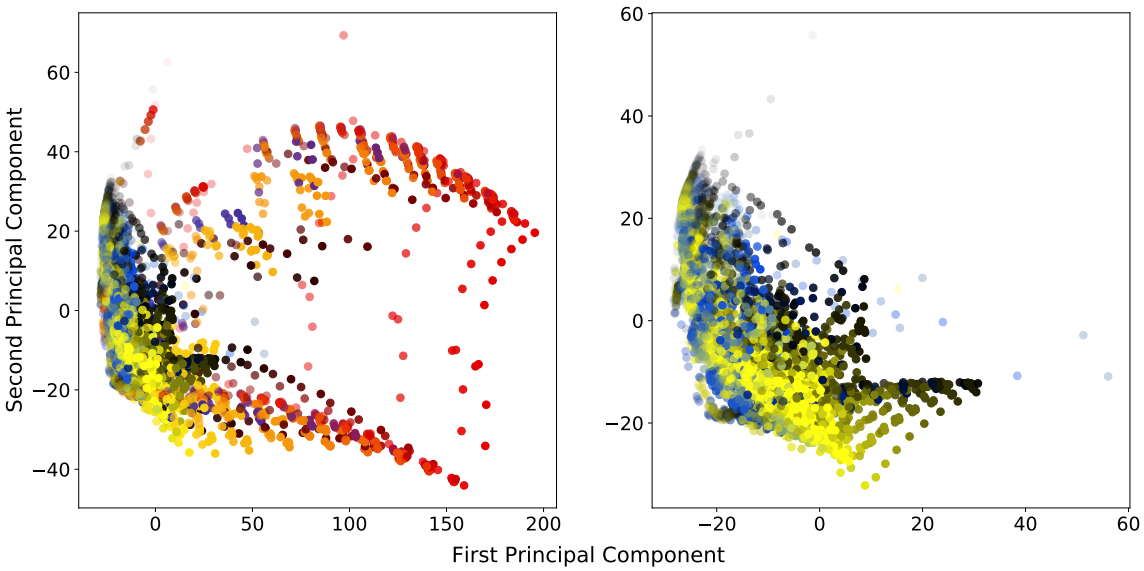

Figure 5-5: Principal component analysis of HD 109573 system with a particle size distribution with a power-law slope of -3.5. Porosity of the dust grains is reflected in the opacity of the point. Colors are represented as blends of four base compositional families: red represents troilite and iron composition, yellow represents silicate compositions, blue represents water compositions, and black represents carbonaceous compositions. The left plot examines all of the compositions in the sample, while the right plot considers only those compositions that do not include any iron or troilite component.

likely a result of the unique temperature and location of the HD 172555 dust; the other disks in our sample have colder dust that is much further out than HD 172555. We also utilize PCA on subsets of the spectra; specifically, we perform PCA on the spectra between 0.1 and 2.5μm (HST), between 2.5 and 28.5 μm (JWST excluding HST overlap), spectra between 0.1 and 28.5 μm (HST and JWST), and between 600 and 1400 μm (ALMA bands 6 and 7). This analysis seeks to understand how the PC-space alters if only subsections of the dust spectra are taken into consideration. As can be clearly seen in Figure 5-7, the PC space alters significantly if any one of the telescopes is used alone, suggesting that different conclusions as to the compositional nature of dust will be arrived at if the dust spectra is not examined in context. When HST and JWST bandpasses are taken into consideration, the PC-space does look more comparable to the PC-space for the full spectrum, but there are notable difference - primarily that the water ice features do not separate out as clearly. This indicates

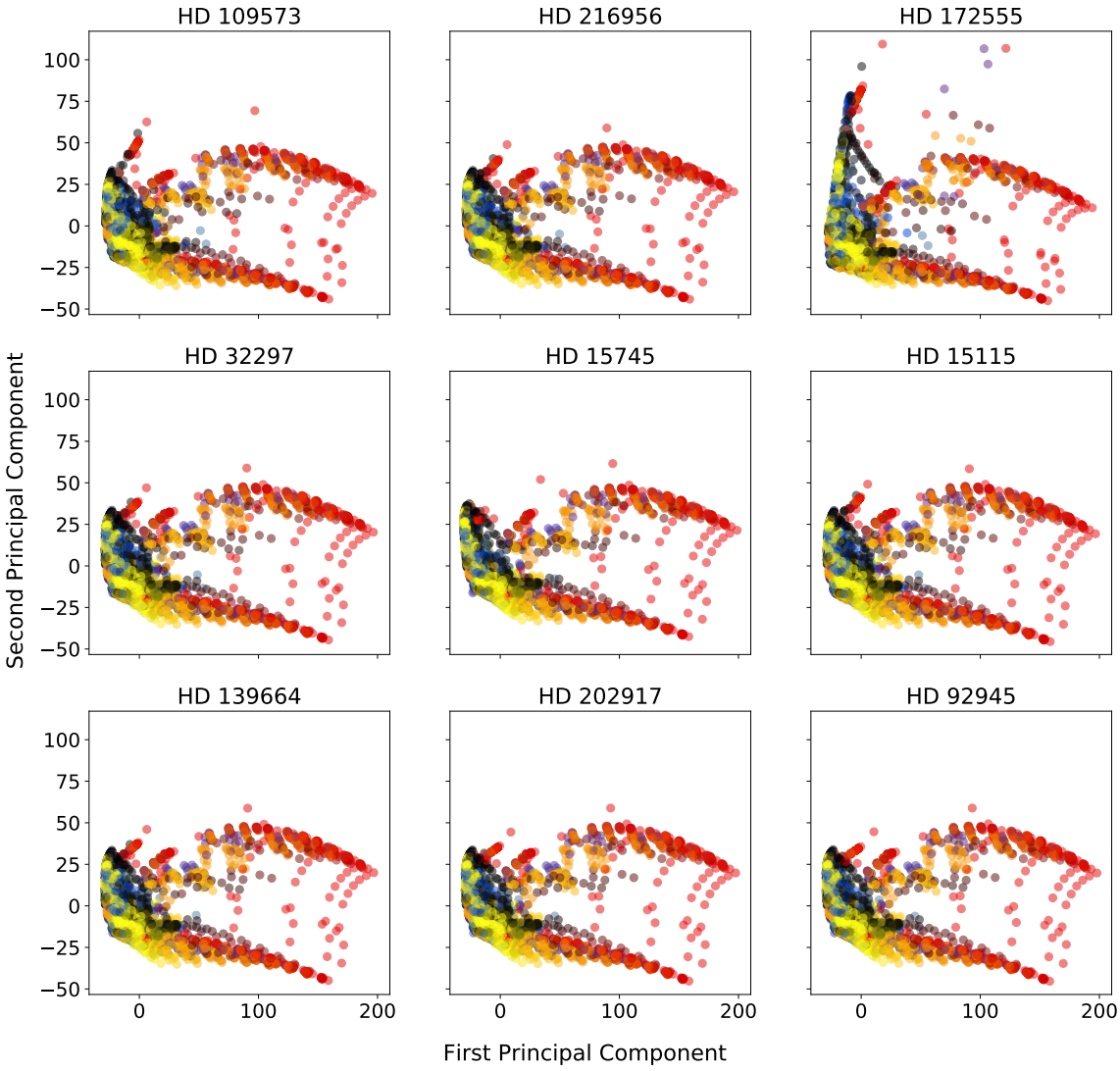

Figure 5-6: Principal component analysis for all 9 systems in the sample for particle size distributions with a power-law slope of -3.5. Porosity is not reflected in the opacity of the point. Colors are represented as blends of four base compositional families: red represents troilite and iron composition, yellow represents silicate compositions, blue represents water compositions, and black represents carbonaceous compositions. These systems are around a varied set of stars, at a range of ages, for a variety of distances from the star, and with different relative luminosities in comparison to their host stars.

that for the systems where ALMA data is not yet available, it should be a priority to acquire band 6 and 7 constraints on continuum emission to fully characterize dust.

5.5 Discussion

The lack of spectral variation observed for changing particle size distributions (Figure 5-3) is unexpected. In [171], similar particle sizes (and spacings), as well as distributions are chosen. Their discussion lacks mention of the PSD effect on their resulting spectra, so it is possible that their fits show no variation based on varying PSDs. We believe that the lack of PSD-driven variation in these samples is due to the choice of logarithmically-spaced particle sizes. This artificially places excess weight in the smallest particles in the distribution, and future work should choose to adopt linearly-spaced particle sizes. Although this will increase the computational load of the calculations, it is necessary for accurate modeling of the PSD in a system. It is also necessary to increase the maximum particle size considered in these models. Currently, the maximum particle size considered is 1000 μm, which corresponds to a maximum Mie size parameter of 4.5. For some compositions, this seems to be large enough to enter behavior approximating the geometric optics regime; for others (most notably carbonaceous compositions), the spectra in the ALMA bandpasses are dominated by Mie resonances. This is not accurate of the actual spectra we may see from these disks, and as such it is necessary to include larger particle sizes to fully capture the scattered and thermal emission of dust in these disks. [51] suggests that maximum particle sizes should be $\sim$3 times as much as the maximum wavelength of the observation, which yields a maximum particle size of 4200 μm. It may also be worth exploring alternate weighting schemes for the PSDs to correct for the logarithmic spacing.

We note that the PCA results diverge from what we might naively expect based on the by-eye examination of the HD 109573 root composition spectra in Figure 5-4. Examining these spectra, it seems that the troilite, iron, and carbonaceous compositions might cluster together, with both water and silicates showing distinct

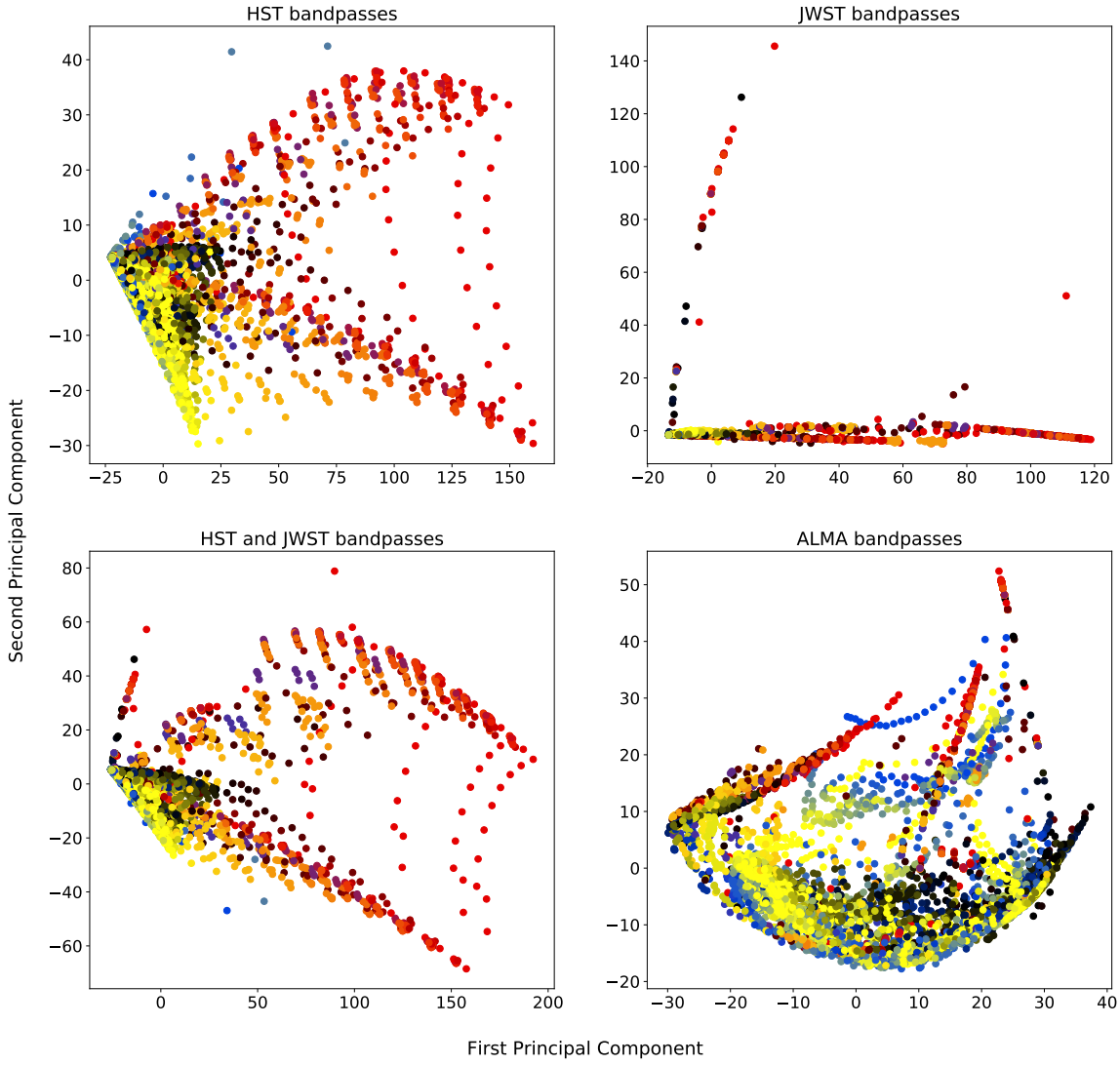

Figure 5-7: Principal component analysis for HD 109573 system for a particle size distribution with power-law slope of -3.5. Porosity is not reflected in the opacity of the point. Colors are represented as blends of four base compositional families: red represents troilite and iron composition, yellow represents silicate compositions, blue represents water compositions, and black represents carbonaceous compositions. Top left panel is looking at the PCA results when considering just spectra in the HST range. Top right panel displays PCA results when considering spectra in the range between the end of the HST range and the end of the JWST range. Bottom left panel looks at PCA results when looking at HST and JWST wavelength ranges together. Bottom right panel looks at PCA results when looking solely at ALMA bands 6 and 7.

features that result in separation in PC-space. Instead, iron and troilite appear to be most differentiated from a grouping of water ice, silicate, and carbonaceous compositions. To identify whether this is a persistent trend, we anticipate running PCA analysis for the new dataset with a better sampling of particle sizes, as described above. Additional principal components should also be used to see if water, silicates, and carbon cluster apart from each other in the subsequent principal component.

For these models to be usable in advance of upcoming data from JWST, the simulated spectra need to be passed through realistic telescope models for HST, JWST, and ALMA and binned appropriately. PCA applied to binned data may pull out different variances, which will result in different clustering within PC space. Realistic telescope models will take into account the spectral width of bins, systematic noise effects, and the relative strength and weighting of the different telescope facilities. We anticipate collaborating with observers who are more familiar with this process.

5.6 Conclusions

Principal component analysis of the spectra for each system in our sample suggest that iron- and troilite-dominated compositions are easy to differentiate from a core of water, silicate, and carbonaceous compositions. The latter three are more complicated to disentangle, and require additional follow-up work to identify the feasibility of use of PCA to understand acquired spectra. However, the PCA suggests that it may be possible to reduce the explored parameter space when fitting observations of nearly edge-on debris disks. If the acquired spectra are transformed into PC-space, the location of the spectrum will point to a subset of compositions that should be explored while fitting. If a subset of compositions can be explored rather than the full parameter space, computational time will be greatly reduced.

Chapter 6

Conclusions

This thesis uses three methodologies to probe planetary system histories by examining different aspects of circumstellar gas and dust at varied ages. In Chapters 2 and 3, experimental methods were used to determine the desorption binding energies and entrapment efficiencies of neon, argon, krypton, and xenon. These physical quantities allow us to probe the gas-phase and solid-body distribution of the noble elements within the protoplanetary disk. Entrapment experiments are applicable to understanding the survival of noble gases entrapped in interstellar medium analog ices while desorption experiments are key to understanding noble snowline locations in the protoplanetary disk. We find that the behavior of argon, krypton, and xenon is markedly different from the behavior of neon. In the case of argon, krypton, and xenon, the desorption binding energies are well-characterized within the experimental setup. Additionally, the three heavier noble gases are efficiently trapped within water ice mixtures; in astrophysically relevant ices, entrapment efficiencies range from 65 to 95%. In contrast, the desorption binding energy of neon is not well constrained within the experimental setup, likely due to the forced desorption of neon by hydrogen. In addition, neon is inefficiently trapped. In mixture ices, less than 1% of neon is entrapped, while in burial entrapment experiments, at most 10% of neon is trapped. These results have implications for the formation histories of the planets within our solar system; due to the inert nature of the noble gases, we currently only have measurements for noble gases in solar system bodies via in-situ studies. It is

important to note that neon is expected to be a tracer of exclusively nebular gas; if neon is detected in a planetary atmosphere, it is quite likely that the planetary body accreted some nebular gas. In contrast, the heavier noble gases argon, krypton, and xenon are expected to be tracers for both nebular gas and solid-body delivery. A comprehensive understanding of formation histories of solar system bodies will be dependent on models that incorporate these experimental results. Any model seeking to explain the migration of bodies and timing for accreting atmospheres will need to account for the noble gas content. It is thus quite promising that the next several decades will increase our understanding of noble gas distributions within the solar system. Upcoming probes to Venus, Titan (in the form of the Dragonfly mission), and the planned flagship mission to Uranus will provide critical data constraining the noble gas content of solar system bodies, which will enable us to better understand formation conditions for the bodies within our solar system.

While Chapters 2 and 3 trace the accretion histories of planetary bodies, Chapter 4 instead focuses on a case study for the evolution of planetary atmospheres. This chapter presents archival observations from the Atacama Large Millimeter Array (ALMA) that have identified the first protoplanetary atmosphere stripped in a giant impact. Although theory has predicted the ability of giant impacts to strip primary atmospheres from terrestrial bodies, these observations of the HD 172555 system are the first direct evidence of the phenomena. The critical finding here is that it is important to examine both gas and dust in tandem to fully understand the history of giant impacts. Although previous studies examined the atypical dust present in the system, debate within the community existed over whether the dust could be explained by a steady-state asteroid belt. The presence of carbon monoxide gas in the system, however, provides additional evidence that excludes other origins for the gas and dust. The work here demonstrates the need to understand circumstellar gas and dust. It also provides an avenue towards identifying more systems where giant impacts have taken place. It is a bit of a quandary in the literature that more giant impact systems have not been identified, as solar-system evidence points to the phenomena being a ubiquitous process. If more systems can be identified as

having both atypical dust signatures and the presence of unexpected gas, a process of exclusion such as the one we exploit in Chapter 4 can be used to identify giant impact candidates. Although no other known systems with the presence of tektite and obsidian mineralogy have been identified, it may be possible to search for systems with non-steady-state particle size distributions. For systems with this anomaly, follow-up searches for CO gas in the system would be worthwhile.

In Chapter 5, a cautious attempt at simulating multibandpass observations of highly inclined debris disks was undertaken. The parameter space explored includes composition as well as particle size distribution. We find that iron and troilite dominated compositions are easy to differentiate from water, silicate, and carbonaceous compositions in principal component space. We also find that multibandpass characterization is required to fully understand dust compositions. Further improvements to the model will enable us to identify anomalous particle size distributions, providing candidate systems in which to search for the evidence of giant impacts. The ability to quickly identify candidate systems for giant impacts, as well as to better understand the bulk compositions of parent planetesimals within debris disks, will provide a better understanding for the formation histories of debris disk systems.

It is clear from this thesis that circumstellar gas and dust must be understood to probe the histories of planetary systems. Noble gases within solar system planetary atmospheres are excellent tracers for the accretion and evolution of those atmospheres from the protoplanetary disk to today. Understanding the dust in debris systems is critical to understanding parent planetesimal compositions and atypical particle size distributions, which provides candidate systems for follow-up observations. Understanding both the dust and the gas within the HD 172555 system has enabled us to identify for the first time a stripped protoplanetary atmosphere.

Appendix A

List of Acronyms

ALMA	Atacama Large Millimeter Array
ASW	Amorphous solid water
au	Astronomical Unit
CASA	Common Astronomy Software Applications
DI	deionized
FTIR	Fourier Transform Infrared
FWHM	Full-width half-maximum
GHz	Gigahertz
HST	Hubble Space Telescope
IR	Infrared
IRAS	Infrared Astronomical Satellite
ISM	Interstellar medium
JWST	James Webb Space Telescope
K	Kelvin
LTE	Local thermodynamic equilibrium
MCMC	Markov chain Monte Carlo
ML	Monolayer
MMSN	Minimum mass Solar nebula
Myr	Million years

NG	Noble gas
OFHC	oxygen-free high thermal conductivity
pc	parsec
PC	Principal Component
PCA	Principal component analysis
PSD	Particle size distribution
QMS	Quadrupole mass spectrometer
SED	Spectral energy distribution
TPD	Temperature programmed desorption
UHV	Ultra-high vacuum
UV	Ultraviolet
WTTS	Weak-lined T Tauri Stars

Bibliography

[1] K. Acharyya, G. W. Fuchs, H. J. Fraser, E. F. van Dishoeck, and H. Linnartz. Desorption of co and o ₂ interstellar ice analogs. *Astronomy & Astrophysics*, 466:1005–1012, 5 2007.

[2] Y. Aikawa and H. Nomura. Physical and Chemical Structure of Protoplanetary Disks with Grain Growth. *The Astrophysical Journal*, 642(2):1152–1162, May 2006.

[3] Sean M. Andrews, Jane Huang, Laura M. Pérez, Andrea Isella, Cornelis P. Dullemond, Nicolás T. Kurtovic, Viviana V. Guzmán, John M. Carpenter, David J. Wilner, Shangjia Zhang, Zhaohuan Zhu, Tilman Birnstiel, Xue-Ning Bai, Myriam Benisty, A. Meredith Hughes, Karin I. Öberg, and Luca Ricci. The Disk Substructures at High Angular Resolution Project (DSHARP). I. Motivation, Sample, Calibration, and Overview. *The Astrophysical Journal*, 869(2):L41, December 2018.

[4] Sean M. Andrews and Jonathan P. Williams. A Submillimeter View of Circumstellar Dust Disks in ρ Ophiuchi. *The Astrophysical Journal*, 671(2):1800–1812, December 2007.

[5] Sean M. Andrews and Jonathan P. Williams. High-resolution submillimeter constraints on circumstellar disk structure. *The Astrophysical Journal*, 659:705–728, 4 2007.

[6] Philip J. Armitage, Josh A. Eisner, and Jacob B. Simon. Prompt Planetesimal Formation beyond the Snow Line. *The Astrophysical Journal*, 828(1):L2, September 2016.

[7] Pauline Arriaga, Michael P. Fitzgerald, Gaspard Duchêne, Paul Kalas, Maxwell A. Millar-Blanchaer, Marshall D. Perrin, Christine H. Chen, Johan Mazoyer, Mark Ammons, Vanessa P. Bailey, Trafis S. Barman, Joanna Bulger, Jeffrey K. Chilcote, Tara Cotten, Robert J. De Rosa, Rene Doyon, Thomas M. Esposito, Katherine B. Follette, Benjamin L. Gerard, Stephen Goodsell, James R. Graham, Alexandra Z. Greenbaum, Pascale Hibon, Justin Hom, Li-Wei Hung, Patrick Ingraham, Quinn M. Konopacky, Bruce A. Macintosh, Jérôme Maire, Franck Marchis, Mark S. Marley, Christian Marois, Stanimir Metchev, Eric L. Nielsen, Rebecca Oppenheimer, David W. Palmer, Jenny Patience, Lisa A.

Poyneer, Laurent Pueyo, Abhijith Rajan, Julien Rameau, Fredrik T. Rantakyrö, Jean-Baptiste Ruffio, Dmitry Savransky, Adam C. Schneider, Anand Sivaramakrishnan, Inseok Song, Remi Soummer, Sandrine Thomas, Jason J. Wang, Kimberly Ward-Duong, and Schuyler G. Wolff. Multiband Polarimetric Imaging of HR 4796A with the Gemini Planet Imager. *The Astronomical Journal*, 160(2):79, August 2020.

[8] Sushil K. Atreya, Mark H. Hofstadter, Joong Hyun In, Olivier Mousis, Kim Reh, and Michael H. Wong. Deep Atmosphere Composition, Structure, Origin, and Exploration, with Particular Focus on Critical in situ Science at the Icy Giants. *Space Sciences Review*, 216(1):18, February 2020.

[9] Patrick Ayotte, R. Scott Smith, K. P. Stevenson, Z. Dohnálek, Greg A. Kimmel, and Bruce D. Kay. Effect of porosity on the adsorption, desorption, trapping, and release of volatile gases by amorphous solid water. *Journal of Geophysical Research: Planets*, 106:33387–33392, 2001.

[10] A. Bar-Nun, G. Notesco, and T. Owen. Trapping of n2, co and ar in amorphous ice-application to comets. *Icarus*, 190:655–659, 2007.

[11] Steven V. W. Beckwith, Anneila I. Sargent, Rolf S. Chini, and Rolf Guesten. A survey for circumstellar disks around young stellar objects. *The Astronomical Journal*, 99:924, 3 1990.

[12] Aida Behmard, Edith C. Fayolle, Dawn M. Graninger, Jennifer B. Bergner, Rafael Martín-Doménech, Pavlo Maksyutenko, Mahesh Rajappan, and Karin I. Öberg. Desorption Kinetics and Binding Energies of Small Hydrocarbons. *Astrophysical Journal*, 875(1):73, April 2019.

[13] W. Benz, A. Anic, J. Horner, and J. A. Whitby. The origin of mercury. *Space Science Reviews*, 132:189–202, 10 2007.

[14] John B Biersteker and Hilke E Schlichting. Atmospheric mass-loss due to giant impacts: the importance of the thermal component for hydrogen–helium envelopes. *Monthly Notices of the Royal Astronomical Society*, 485:4454–4463, 5 2019.

[15] Nicolas Biver, Dominique Bockelée-Morvan, Pierre Colom, Jacques Crovisier, Florence Henry, Emmanuel Lellouch, Anders Winnberg, Lars E.B. Johansson, Marcus Gunnarsson, Hans Rickman, Fredrik Rantakyrö, John K. Davies, William R.F. Dent, Gabriel Paubert, Raphaël Moreno, Jörn Wink, Didier Despois, Dominic J. Benford, Matt Gardner, Dariusz C. Lis, David Mehringer, Thomas G. Phillips, and Heike Rauer. The 1995 2002 long-term monitoring of comet c/1995 o1 (hale bopp) at radio wavelength. *Earth, Moon, and Planets*, 90:5–14, 2002.

[16] J. Blum and G. Wurm. The growth mechanisms of macroscopic bodies in protoplanetary disks. *Annual Review of Astronomy and Astrophysics*, 46:21–56, September 2008.

[17] Y. Boehler, L. Ricci, E. Weaver, A. Isella, M. Benisty, J. Carpenter, C. Grady, Bo-Ting Shen, Ya-Wen Tang, and L. Perez. The complex morphology of the young disk mwc 758: Spirals and dust clumps around a large cavity. *The Astrophysical Journal*, 853:162, 2 2018.

[18] M. Bonnefoy, J. Milli, F. Menard, P. Delorme, A. Chomez, M. Bonavita, A. M. Lagrange, A. Vigan, J. C. Augereau, J. L. Beuzit, B. Biller, A. Boccaletti, G. Chauvin, S. Desidera, V. Faramaz, R. Galicher, R. Gratton, S. Hinkley, C. Lazzoni, E. Matthews, D. Mesa, C. Mordasini, D. Mouillet, J. Olofsson, and C. Pinte. Narrow belt of debris around the Sco-Cen star HD 141011. *Astronomy and Astrophysics*, 655:A62, November 2021.

[19] A.C. Adwin Boogert, Perry A. Gerakines, and Douglas C.B. Whittet. Observations of the icy universe. *Annual Review of Astronomy and Astrophysics*, 53:541–581, 8 2015.

[20] William F. Bottke, Daniel D. Durda, David Nesvorný, Robert Jedicke, Alessandro Morbidelli, David Vokrouhlický, and Harold F. Levison. Linking the collisional history of the main asteroid belt to its dynamical excitation and depletion. *Icarus*, 179(1):63–94, December 2005.

[21] A. G. A. Brown, A. Vallenari, T. Prusti, J. H. J. de Bruijne, C. Babusiaux, C. A. L. Bailer-Jones, M. Biermann, D. W. Evans, L. Eyer, F. Jansen, C. Jordi, S. A. Klioner, U. Lammers, L. Lindegren, X. Luri, F. Mignard, C. Panem, D. Pourbaix, S. Randich, P. Sartoretti, H. I. Siddiqui, C. Soubiran, F. van Leeuwen, N. A. Walton, F. Arenou, U. Bastian, M. Cropper, R. Drimmel, D. Katz, M. G. Lattanzi, J. Bakker, C. Cacciari, J. Castañeda, L. Chaoul, N. Cheek, F. De Angeli, C. Fabricius, R. Guerra, B. Holl, E. Masana, R. Messineo, N. Mowlavi, K. Nienartowicz, P. Panuzzo, J. Portell, M. Riello, G. M. Seabroke, P. Tanga, F. Thévenin, G. Gracia-Abril, G. Comoretto, M. Garcia-Reinaldos, D. Teyssier, M. Altmann, R. Andrae, M. Audard, I. Bellas-Velidis, K. Benson, J. Berthier, R. Blomme, P. Burgess, G. Busso, B. Carry, A. Cellino, G. Clementini, M. Clotet, O. Creevey, M. Davidson, J. De Ridder, L. Delchambre, A. Dell'Oro, C. Ducourant, J. Fernández-Hernández, M. Fouesneau, Y. Frémat, L. Galluccio, M. García-Torres, J. González-Núñez, J. J. González-Vidal, E. Gosset, L. P. Guy, J.-L. Halbwachs, N. C. Hambly, D. L. Harrison, J. Hernández, D. Hestroffer, S. T. Hodgkin, A. Hutton, G. Jasniewicz, A. Jean-Antoine-Piccolo, S. Jordan, A. J. Korn, A. Krone-Martins, A. C. Lanzafame, T. Lebzelter, W. Löffler, M. Manteiga, P. M. Marrese, J. M. Martín-Fleitas, A. Moitinho, A. Mora, K. Muinonen, J. Osinde, E. Pancino, T. Pauwels, J.-M. Petit, A. Recio-Blanco, P. J. Richards, L. Rimoldini, A. C. Robin, L. M. Sarro, C. Siopis, M. Smith, A. Sozzetti, M. Süveges, J. Torra, W. van Reeven,

U. Abbas, A. Abreu Aramburu, S. Accart, C. Aerts, G. Altavilla, M. A. Álvarez, R. Alvarez, J. Alves, R. I. Anderson, A. H. Andrei, E. Anglada Varela, E. Antiche, T. Antoja, B. Arcay, T. L. Astraatmadja, N. Bach, S. G. Baker, L. Balaguer-Núñez, P. Balm, C. Barache, C. Barata, D. Barbato, F. Barblan, P. S. Barklem, D. Barrado, M. Barros, M. A. Barstow, S. Bartholomé Muñoz, J.-L. Bassilana, U. Becciani, M. Bellazzini, A. Berihuete, S. Bertone, L. Bianchi, O. Bienaymé, S. Blanco-Cuaresma, T. Boch, C. Boeche, A. Bombrun, R. Borrachero, D. Bossini, S. Bouquillon, G. Bourda, A. Bragaglia, L. Bramante, M. A. Breddels, A. Bressan, N. Brouillet, T. Brüsemeister, E. Brugaletta, B. Bucciarelli, A. Burlacu, D. Busonero, A. G. Butkevich, R. Buzzi, E. Caffau, R. Cancelliere, G. Cannizzaro, T. Cantat-Gaudin, R. Carballo, T. Carlucci, J. M. Carrasco, L. Casamiquela, M. Castellani, A. Castro-Ginard, P. Charlot, L. Chemin, A. Chiavassa, G. Cocozza, G. Costigan, S. Cowell, F. Crifo, M. Crosta, C. Crowley, J. Cuypers†, C. Dafonte, Y. Damerdji, A. Dapergolas, P. David, M. David, P. de Laverny, F. De Luise, R. De March, D. de Martino, R. de Souza, A. de Torres, J. Debosscher, E. del Pozo, M. Delbo, A. Delgado, H. E. Delgado, P. Di Matteo, S. Diakite, C. Diener, E. Distefano, C. Dolding, P. Drazinos, J. Durán, B. Edvardsson, H. Enke, K. Eriksson, P. Esquej, G. Eynard Bontemps, C. Fabre, M. Fabrizio, S. Faigler, A. J. Falcão, M. Farràs Casas, L. Federici, G. Fedorets, P. Fernique, F. Figueras, F. Filippi, K. Findeisen, A. Fonti, E. Fraile, M. Fraser, B. Frézouls, M. Gai, S. Galleti, D. Garabato, F. García-Sedano, A. Garofalo, N. Garralda, A. Gavel, P. Gavras, J. Gerssen, R. Geyer, P. Giacobbe, G. Gilmore, S. Girona, G. Giuffrida, F. Glass, M. Gomes, M. Granvik, A. Gueguen, A. Guerrier, J. Guiraud, R. Gutiérrez-Sánchez, R. Haigron, D. Hatzidimitriou, M. Hauser, M. Haywood, U. Heiter, A. Helmi, J. Heu, T. Hilger, D. Hobbs, W. Hofmann, G. Holland, H. E. Huckle, A. Hypki, V. Icardi, K. Janßen, G. Jevardat de Fombelle, P. G. Jonker, Á. L. Juhász, F. Julbe, A. Karampelas, A. Kewley, J. Klar, A. Kochoska, R. Kohley, K. Kolenberg, M. Kontizas, E. Kontizas, S. E. Koposov, G. Kordopatis, Z. Kostrzewa-Rutkowska, P. Koubsky, S. Lambert, A. F. Lanza, Y. Lasne, J.-B. Lavigne, Y. Le Fustec, C. Le Poncin-Lafitte, Y. Lebreton, S. Leccia, N. Leclerc, I. Lecoeur-Taibi, H. Lenhardt, F. Leroux, S. Liao, E. Licata, H. E. P. Lindstrøm, T. A. Lister, E. Livanou, A. Lobel, M. López, S. Managau, R. G. Mann, G. Mantelet, O. Marchal, J. M. Marchant, M. Marconi, S. Marinoni, G. Marschalkó, D. J. Marshall, M. Martino, G. Marton, N. Mary, D. Massari, G. Matijevič, T. Mazeh, P. J. McMillan, S. Messina, D. Michalik, N. R. Millar, D. Molina, R. Molinaro, L. Molnár, P. Montegriffo, R. Mor, R. Morbidelli, T. Morel, D. Morris, A. F. Mulone, T. Muraveva, I. Musella, G. Nelemans, L. Nicastro, L. Noval, W. O'Mullane, C. Ordénovic, D. Ordóñez-Blanco, P. Osborne, C. Pagani, I. Pagano, F. Pailler, H. Palacin, L. Palaversa, A. Panahi, M. Pawlak, A. M. Piersimoni, F.-X. Pineau, E. Plachy, G. Plum, E. Poggio, E. Poujoulet, A. Prša, L. Pulone, E. Racero, S. Ragaini, N. Rambaux, M. Ramos-Lerate, S. Regibo, C. Reylé, F. Riclet, V. Ripepi, A. Riva, A. Rivard, G. Rixon, T. Roegiers, M. Roelens, M. Romero-Gómez, N. Rowell, F. Royer, L. Ruiz-Dern, G. Sadowski, T. Sagristà Sellés, J. Sahlmann,

J. Salgado, E. Salguero, N. Sanna, T. Santana-Ros, M. Sarasso, H. Savietto, M. Schultheis, E. Sciacca, M. Segol, J. C. Segovia, D. Ségransan, I-C. Shih, L. Siltala, A. F. Silva, R. L. Smart, K. W. Smith, E. Solano, F. Solitro, R. Sordo, S. Soria Nieto, J. Souchay, A. Spagna, F. Spoto, U. Stampa, I. A. Steele, H. Steidelmüller, C. A. Stephenson, H. Stoev, F. F. Suess, J. Surdej, L. Szabados, E. Szegedi-Elek, D. Tapiador, F. Taris, G. Tauran, M. B. Taylor, R. Teixeira, D. Terrett, P. Teyssandier, W. Thuillot, A. Titarenko, F. Torra Clotet, C. Turon, A. Ulla, E. Utrilla, S. Uzzi, M. Vaillant, G. Valentini, V. Valette, A. van Elteren, E. Van Hemelryck, M. van Leeuwen, M. Vaschetto, A. Vecchiato, J. Veljanoski, Y. Viala, D. Vicente, S. Vogt, C. von Essen, H. Voss, V. Votruba, S. Voutsinas, G. Walmsley, M. Weiler, O. Wertz, T. Wevers, Ł. Wyrzykowski, A. Yoldas, M. Žerjal, H. Ziaeepour, J. Zorec, S. Zschocke, S. Zucker, C. Zurbach, and T. Zwitter. Gaia data release 2. *Astronomy & Astrophysics*, 616:A1, 8 2018.

[22] Robin M. Canup. Simulations of a late lunar-forming impact. *Icarus*, 168:433–456, 4 2004.

[23] Robin. M. Canup. Forming a moon with an earth-like composition via a giant impact. *Science*, 338:1052–1055, 11 2012.

[24] John M. Carpenter, Eric E. Mamajek, Lynne A. Hillenbrand, and Michael R. Meyer. Evidence for Mass-dependent Circumstellar Disk Evolution in the 5 Myr Old Upper Scorpius OB Association. *The Astrophysical Journal*, 651(1):L49–L52, November 2006.

[25] Stefan I. B. Cartledge, David M. Meyer, and J. T. Lauroesch. The Homogeneity of Interstellar Krypton in the Galactic Disk. *Astrophysical Journal*, 597(1):408–413, November 2003.

[26] P. Cassen and A. Moosman. On the formation of protostellar disks. *Icarus*, 48(3):353–376, December 1981.

[27] G. Chabrier, A. Johansen, M. Janson, and R. Rafikov. Giant Planet and Brown Dwarf Formation. In Henrik Beuther, Ralf S. Klessen, Cornelis P. Dullemond, and Thomas Henning, editors, *Protostars and Planets VI*, page 619, January 2014.

[28] Alice Chau, Christian Reinhardt, Ravit Helled, and Joachim Stadel. Forming mercury by giant impacts. *The Astrophysical Journal*, 865:35, 9 2018.

[29] C. H. Chen, B. A. Sargent, C. Bohac, K. H. Kim, E. Leibensperger, M. Jura, J. Najita, W. J. Forrest, D. M. Watson, G. C. Sloan, and L. D. Keller. Spitzer irs spectroscopy of iras-discovered debris disks. *The Astrophysical Journal Supplement Series*, 166:351–377, 9 2006.

[30] J. E. Chiar, A. G. G. M. Tielens, A. J. Adamson, and A. Ricca. The Structure, Origin, and Evolution of Interstellar Hydrocarbon Grains. *The Astrophysical Journal*, 770(1):78, June 2013.

[31] Fred J. Ciesla. Dust coagulation and settling in layered protoplanetary disks. *The Astrophysical Journal*, 654:L159–L162, 1 2007.

[32] Fred J. Ciesla and Jeffrey N. Cuzzi. The evolution of the water distribution in a viscous protoplanetary disk. *Icarus*, 181(1):178–204, March 2006.

[33] Fred J. Ciesla, Sebastiaan Krijt, Reika Yokochi, and Scott Sandford. The efficiency of noble gas trapping in astrophysical environments. *The Astrophysical Journal*, 867:146, 11 2018.

[34] Lucas Cieza, Deborah L. Padgett, Karl R. Stapelfeldt, Jean-Charles Augereau, Paul Harvey, II Evans, Neal J., Bruno Merín, David Koerner, Anneila Sargent, Ewine F. van Dishoeck, Lori Allen, Geoffrey Blake, Timothy Brooke, Nicholas Chapman, Tracy Huard, Shih-Ping Lai, Lee Mundy, Philip C. Myers, William Spiesman, and Zahed Wahhaj. The Spitzer c2d Survey of Weak-Line T Tauri Stars. II. New Constraints on the Timescale for Planet Building. *The Astrophysical Journal*, 667(1):308–328, September 2007.

[35] L. Ilsedore Cleeves, Edwin A. Bergin, Conel M. O. 'D. Alexander, Fujun Du, Dawn Graninger, Karin I. Öberg, and Tim J. Harries. The ancient heritage of water ice in the solar system. *Science*, 345(6204):1590–1593, September 2014.

[36] M. P. Collings, V.L. Frankland, J. Lasne, D. Marchione, A. Rosu-Finsen, and M. R. S. McCoustra. Probing model interstellar grain surfaces with small molecules. *Monthly Notices of the Royal Astronomical Society*, 449:1826–1833, 5 2015.

[37] J. Cote. B and a type stars with unexpectedly large colour excesses at iras wavelengths. *Astronomy and Astrophysics*, 181:77–84, 1987.

[38] Patrick F. Cronin-Coltsmann, Grant M. Kennedy, Paul Kalas, Julien Milli, Cathie J. Clarke, Gaspard Duchêne, Jane Greaves, Samantha M. Lawler, Jean-François Lestrade, Brenda C. Matthews, Andrew Shannon, and Mark C. Wyatt. ALMA imaging of the M-dwarf Fomalhaut C's debris disc. *Monthly Notices of the Royal Astronomical Society*, 504(3):4497–4510, July 2021.

[39] Thayne Currie, Ryan Cloutier, Sean Brittain, Carol Grady, Adam Burrows, Takayuki Muto, Scott J. Kenyon, and Marc J. Kuchner. Resolving the HD 100546 Protoplanetary System with the Gemini Planet Imager: Evidence for Multiple Forming, Accreting Planets. *The Astrophysical Journal*, 814(2):L27, December 2015.

[40] Thayne Currie, Kellen Lawson, Glenn Schneider, Wladimir Lyra, John Wisniewski, Carol Grady, Olivier Guyon, Motohide Tamura, Takayuki Kotani,

Hajime Kawahara, Timothy Brandt, Taichi Uyama, Takayuki Muto, Ruobing Dong, Tomoyuki Kudo, Jun Hashimoto, Misato Fukagawa, Kevin Wagner, Julien Lozi, Jeffrey Chilcote, Taylor Tobin, Tyler Groff, Kimberly Ward-Duong, William Januszewski, Barnaby Norris, Peter Tuthill, Nienke van der Marel, Michael Sitko, Vincent Deo, Sebastien Vievard, Nemanja Jovanovic, Frantz Martinache, and Nour Skaf. Images of embedded Jovian planet formation at a wide separation around AB Aurigae. *Nature Astronomy*, April 2022.

[41] Jeffrey N. Cuzzi and Kevin J. Zahnle. Material Enhancement in Protoplanetary Nebulae by Particle Drift through Evaporation Fronts. *The Astrophysical Journal*, 614(1):490–496, October 2004.

[42] Paola D'Alessio, Nuria Calvet, and Lee Hartmann. Accretion Disks around Young Objects. III. Grain Growth. *The Astrophysical Journal*, 553(1):321–334, May 2001.

[43] Trevor J. David and Lynne A. Hillenbrand. The ages of early-type stars: StrÖmgren photometric methods calibrated, validated, tested, and applied to hosts and prospective hosts of directly imaged exoplanets. *The Astrophysical Journal*, 804:146, 5 2015.

[44] J. Huw Davies. Did a mega-collision dry venus' interior? *Earth and Planetary Science Letters*, 268:376–383, 4 2008.

[45] Marie Jourdain de Muizon. Debris Discs Around Stars: The 2004 ISO Legacy. *Space Science Reviews*, 119(1-4):201–214, August 2005.

[46] Sarah E. Dodson-Robinson, Karen Willacy, Peter Bodenheimer, Neal J. Turner, and Charles A. Beichman. Ice lines, planetesimal composition and solid surface density in the solar nebula. *Icarus*, 200(2):672–693, April 2009.

[47] J. S. Dohnanyi. Collisional Model of Asteroids and Their Debris. *Journal of Geophysical Research*, 74:2531–2554, May 1969.

[48] C. Dominik and A. G. G. M. Tielens. The Physics of Dust Coagulation and the Structure of Dust Aggregates in Space. *The Astrophysical Journal*, 480(2):647–673, May 1997.

[49] M. Doronin, M. Bertin, X. Michaut, L. Philippe, and J.-H. Fillion. Adsorption energies and prefactor determination for ch ₃ oh adsorption on graphite. *The Journal of Chemical Physics*, 143:084703, 8 2015.

[50] B. T. Draine. Interstellar Dust Grains. *Annual Review of Astronomy and Astrophysics*, 41:241–289, January 2003.

[51] B. T. Draine. On the Submillimeter Opacity of Protoplanetary Disks. *The Astrophysical Journal*, 636(2):1114–1120, January 2006.

[52] Maria N. Drozdovskaya, Ewine F. van Dishoeck, Martin Rubin, Jes K. Jørgensen, and Kathrin Altwegg. Ingredients for solar-like systems: protostar IRAS 16293-2422 B versus comet 67P/Churyumov-Gerasimenko. *Monthly Notices of the Royal Astronomical Society*, 490(1):50–79, November 2019.

[53] Gaspard Duchêne, Malena Rice, Justin Hom, Joseph Zalesky, Thomas M. Esposito, Maxwell A. Millar-Blanchaer, Bin Ren, Paul Kalas, Michael P. Fitzgerald, Pauline Arriaga, Sebastian Bruzzone, Joanna Bulger, Christine H. Chen, Eugene Chiang, Tara Cotten, Ian Czekala, Robert J. De Rosa, Ruobing Dong, Zachary H. Draper, Katherine B. Follette, James R. Graham, Li-Wei Hung, Ronald Lopez, Bruce Macintosh, Brenda C. Matthews, Johan Mazoyer, Stan Metchev, Jennifer Patience, Marshall D. Perrin, Julien Rameau, Inseok Song, Kevin Stahl, Jason Wang, Schuyler Wolff, Ben Zuckerman, S. Mark Ammons, Vanessa P. Bailey, Travis Barman, Jeffrey Chilcote, Rene Doyon, Benjamin L. Gerard, Stephen J. Goodsell, Alexandra Z. Greenbaum, Pascale Hibon, Patrick Ingraham, Quinn Konopacky, Jérôme Maire, Franck Marchis, Mark S. Marley, Christian Marois, Eric L. Nielsen, Rebecca Oppenheimer, David Palmer, Lisa Poyneer, Laurent Pueyo, Abhijith Rajan, Fredrik T. Rantakyrö, Jean-Baptiste Ruffio, Dmitry Savransky, Adam C. Schneider, Anand Sivaramakrishnan, Rémi Soummer, Sandrine Thomas, and Kimberley Ward-Duong. The Gemini Planet Imager View of the HD 32297 Debris Disk. *The Astronomical Journal*, 159(6):251, June 2020.

[54] C. Eiroa, J. P. Marshall, A. Mora, B. Montesinos, O. Absil, J. Ch. Augereau, A. Bayo, G. Bryden, W. Danchi, C. del Burgo, S. Ertel, M. Fridlund, A. M. Heras, A. V. Krivov, R. Launhardt, R. Liseau, T. Löhne, J. Maldonado, G. L. Pilbratt, A. Roberge, J. Rodmann, J. Sanz-Forcada, E. Solano, K. Stapelfeldt, P. Thébault, S. Wolf, D. Ardila, M. Arévalo, C. Beichmann, V. Faramaz, B. M. González-García, R. Gutiérrez, J. Lebreton, R. Martínez-Arnáiz, G. Meeus, D. Montes, G. Olofsson, K. Y. L. Su, G. J. White, D. Barrado, M. Fukagawa, E. Grün, I. Kamp, R. Lorente, A. Morbidelli, S. Müller, H. Mutschke, T. Nakagawa, I. Ribas, and H. Walker. DUst around NEarby Stars. The survey observational results. *Astronomy and Astrophysics*, 555:A11, July 2013.

[55] N. Engler, H. M. Schmid, S. P. Quanz, H. Avenhaus, and A. Bazzon. Detection of scattered light from the hot dust in hd 172555. *Astronomy & Astrophysics*, 151:1–15, 2018.

[56] Edith C. Fayolle, Jodi Balfe, Ryan Loomis, Jennifer Bergner, Dawn Graninger, Mahesh Rajappan, and Karin I. Öberg. N_2 and CO Desorption Energies from Water Ice. *Astrophysical Journal Letters*, 816(2):L28, January 2016.

[57] F. Feroz, M. P. Hobson, and M. Bridges. Multinest: an efficient and robust bayesian inference tool for cosmology and particle physics. *Monthly Notices of the Royal Astronomical Society*, 398:1601–1614, 10 2009.

[58] Daniel Foreman-Mackey, David W. Hogg, Dustin Lang, and Jonathan Goodman. <tt>emcee</tt> : The mcmc hammer. *Publications of the Astronomical Society of the Pacific*, 125:306–312, 3 2013.

[59] R. T. Garrod and T. Pauly. On the Formation of CO_2 and Other Interstellar Ices. *Astrophysical Journal*, 735(1):15, July 2011.

[60] Christopher R. Glein. A whiff of nebular gas in titan's atmosphere – potential implications for the conditions and timing of titan's formation. *Icarus*, 293:231–242, 9 2017.

[61] D. A. Golimowski, J. E. Krist, K. R. Stapelfeldt, C. H. Chen, D. R. Ardila, G. Bryden, M. Clampin, H. C. Ford, G. D. Illingworth, P. Plavchan, G. H. Rieke, and K. Y. L. Su. Hubble and Spitzer Space Telescope Observations of the Debris Disk around the nearby K Dwarf HD 92945. *The Astronomical Journal*, 142(1):30, July 2011.

[62] R. Gomes, H. F. Levison, K. Tsiganis, and A. Morbidelli. Origin of the cataclysmic Late Heavy Bombardment period of the terrestrial planets. *Nature*, 435(7041):466–469, May 2005.

[63] G. A. Gontcharov. Pulkovo compilation of radial velocities for 35 495 hipparcos stars in a common system. *Astronomy Letters*, 32:759–771, 11 2006.

[64] J. S. Greaves and W. K. M. Rice. Have protoplanetary discs formed planets? *Monthly Notices of the Royal Astronomical Society*, 407(3):1981–1988, September 2010.

[65] B. Gundlach and J. Blum. The Stickiness of Micrometer-sized Water-ice Particles. *The Astrophysical Journal*, 798(1):34, January 2015.

[66] B. Gundlach, S. Kilias, E. Beitz, and J. Blum. Micrometer-sized ice particles for planetary-science experiments – i. preparation, critical rolling friction force, and specific surface energy. *Icarus*, 214:717–723, 8 2011.

[67] C. Güttler, J. Blum, A. Zsom, C. W. Ormel, and C. P. Dullemond. The outcome of protoplanetary dust growth: pebbles, boulders, or planetesimals?. I. Mapping the zoo of laboratory collision experiments. *Astronomy and Astrophysics*, 513:A56, April 2010.

[68] Daniel Harsono, Per Bjerkeli, Matthijs H. D. van der Wiel, Jon P. Ramsey, Luke T. Maud, Lars E. Kristensen, and Jes K. Jørgensen. Evidence for the start of planet formation in a young circumstellar disk. *Nature Astronomy*, 2:646–651, June 2018.

[69] Lee Hartmann, Nuria Calvet, Erik Gullbring, and Paola D'Alessio. Accretion and the Evolution of T Tauri Disks. *The Astrophysical Journal*, 495(1):385–400, March 1998.

[70] Tatsuhiko I. Hasegawa, Eric Herbst, and Chun M. Leukng. Models of gas-grain chemistry in dense interstellar clouds with complex organic molecules. *The Astrophysical Journal Supplement Series*, 82:167, 9 1992.

[71] A. N. Heays, A. D. Bosman, and E. F. van Dishoeck. Photodissociation and photoionisation of atoms and molecules of astrophysical interest. *Astronomy & Astrophysics*, 602:A105, 6 2017.

[72] Lynne A. Hillenbrand, John M. Carpenter, Jinyoung Serena Kim, Michael R. Meyer, Dana E. Backman, Amaya Moro-Martín, David J. Hollenbach, Dean C. Hines, Ilaria Pascucci, and Jeroen Bouwman. The Complete Census of 70 μm-Bright Debris Disks within "The Formation and Evolution of Planetary Systems" Spitzer Legacy Survey of Sun-like Stars. *The Astrophysical Journal*, 677(1):630–656, April 2008.

[73] Robert Hodyss, Mathieu Choukroun, Christophe Sotin, and Patricia Beauchamp. The solubility of ⁴⁰ ar and ⁸⁴ kr in liquid hydrocarbons: Implications for titan's geological evolution. *Geophysical Research Letters*, 40:2935–2940, 6 2013.

[74] J.A. Hogbom. Aperture synthesis with a non-regular distribution of interferometer baselines. *Astronomy and Astrophysics Supplement*, 15:417–426, 1974.

[75] Wayne S. Holland, Brenda C. Matthews, Grant M. Kennedy, Jane S. Greaves, Mark C. Wyatt, Mark Booth, Pierre Bastien, Geoff Bryden, Harold Butner, Christine H. Chen, Antonio Chrysostomou, Claire L. Davies, William R. F. Dent, James Di Francesco, Gaspard Duchêne, Andy G. Gibb, Per Friberg, Rob J. Ivison, Tim Jenness, JJ Kavelaars, Samantha Lawler, Jean-François Lestrade, Jonathan P. Marshall, Amaya Moro-Martin, Olja Panić, Neil Phillips, Stephen Serjeant, Gerald H. Schieven, Bruce Sibthorpe, Laura Vican, Derek Ward-Thompson, Paul van der Werf, Glenn J. White, David Wilner, and Ben Zuckerman. SONS: The JCMT legacy survey of debris discs in the submillimetre. *Monthly Notices of the Royal Astronomical Society*, 470(3):3606–3663, September 2017.

[76] David Hollenbach, Michael J. Kaufman, Edwin A. Bergin, and Gary J. Melnick. Water, o2, and ice in molecular clouds. *Astrophysical Journal*, 2009.

[77] A. Meredith Hughes, Gaspard Duchêne, and Brenda C. Matthews. Debris Disks: Structure, Composition, and Variability. *Annual Review of Astronomy and Astrophysics*, 56:541–591, September 2018.

[78] T.-O. Husser, S. Wende von Berg, S. Dreizler, D. Homeier, A. Reiners, T. Barman, and P. H. Hauschildt. A new extensive library of phoenix stellar atmospheres and synthetic spectra. *Astronomy & Astrophysics*, 553:A6, 5 2013.

[79] Andrea Isella, Jane Huang, Sean M. Andrews, Cornelis P. Dullemond, Tilman Birnstiel, Shangjia Zhang, Zhaohuan Zhu, Viviana V. Guzmán, Laura M. Pérez,

Xue-Ning Bai, Myriam Benisty, John M. Carpenter, Luca Ricci, and David J. Wilner. The disk substructures at high angular resolution project (dsharp). ix. a high-definition study of the hd 163296 planet-forming disk. *The Astrophysical Journal*, 869:L49, 12 2018.

[80] Alan P. Jackson and Mark C. Wyatt. Debris from terrestrial planet formation: the Moon-forming collision. *Monthly Notices of the Royal Astronomical Society*, 425(1):657–679, September 2012.

[81] Arshia M. Jacob, Karl M. Menten, Friedrich Wyrowski, Benjamin Winkel, and David A. Neufeld. Extending the view of ArH^+ chemistry in diffuse clouds. *Astronomy & Astrophysics*, 643:A91, November 2020.

[82] Anders Johansen, Jeffrey S. Oishi, Mordecai-Mark Mac Low, Hubert Klahr, Thomas Henning, and Andrew Youdin. Rapid planetesimal formation in turbulent circumstellar disks. *Nature*, 448:1022–1025, 8 2007.

[83] B. C. Johnson, C. M. Lisse, C. H. Chen, H. J. Melosh, M. C. Wyatt, P. Thebault, W. G. Henning, E. Gaidos, L. T. Elkins-Tanton, J. C. Bridges, and A. Morlok. A self-consistent model of the circumstellar debris created by a giant hypervelocity impact in the hd 172555 system. *Astrophysical Journal*, 761, 2012.

[84] Paul Kalas, Gaspard Duchene, Michael P. Fitzgerald, and James R. Graham. Discovery of an Extended Debris Disk around the F2 V Star HD 15745. *The Astrophysical Journal*, 671(2):L161–L164, December 2007.

[85] Paul Kalas, James R. Graham, and Mark Clampin. A planetary system as the origin of structure in Fomalhaut's dust belt. *Nature*, 435(7045):1067–1070, June 2005.

[86] Paul Kalas, James R. Graham, Mark C. Clampin, and Michael P. Fitzgerald. First Scattered Light Images of Debris Disks around HD 53143 and HD 139664. *The Astrophysical Journal*, 637(1):L57–L60, January 2006.

[87] A. T. Kearsley, G. A. Graham, J. A. M. McDonnell, E. A. Taylor, G. Drolshagen, R. J. Chater, D. McPhail, and M. J. Burchell. The chemical composition of micrometeoroids impacting upon the solar arrays of the Hubble Space Telescope. *Advances in Space Research*, 39(4):590–604, January 2007.

[88] J. A. Kegerreis, V. R. Eke, D. C. Catling, R. J. Massey, L. F. A. Teodoro, and K. J. Zahnle. Atmospheric erosion by giant impacts onto terrestrial planets: A scaling law for any speed, angle, mass, and density. *The Astrophysical Journal*, 901:L31, 9 2020.

[89] Grant M. Kennedy and Scott J. Kenyon. Stellar mass dependent disk dispersal. *The Astrophysical Journal*, 695:1210–1226, 4 2009.

[90] Scott J. Kenyon and Benjamin C. Bromley. Collisional Cascades in Planetesimal Disks. II. Embedded Planets. *The Astronomical Journal*, 127(1):513–530, January 2004.

[91] M. Keppler, M. Benisty, A. Müller, Th. Henning, R. van Boekel, F. Cantalloube, C. Ginski, R. G. van Holstein, A. L. Maire, A. Pohl, M. Samland, H. Avenhaus, J. L. Baudino, A. Boccaletti, J. de Boer, M. Bonnefoy, G. Chauvin, S. Desidera, M. Langlois, C. Lazzoni, G. D. Marleau, C. Mordasini, N. Pawellek, T. Stolker, A. Vigan, A. Zurlo, T. Birnstiel, W. Brandner, M. Feldt, M. Flock, J. Girard, R. Gratton, J. Hagelberg, A. Isella, M. Janson, A. Juhasz, J. Kemmer, Q. Kral, A. M. Lagrange, R. Launhardt, A. Matter, F. Ménard, J. Milli, P. Mollière, J. Olofsson, L. Pérez, P. Pinilla, C. Pinte, S. P. Quanz, T. Schmidt, S. Udry, Z. Wahhaj, J. P. Williams, E. Buenzli, M. Cudel, C. Dominik, R. Galicher, M. Kasper, J. Lannier, D. Mesa, D. Mouillet, S. Peretti, C. Perrot, G. Salter, E. Sissa, F. Wildi, L. Abe, J. Antichi, J. C. Augereau, A. Baruffolo, P. Baudoz, A. Bazzon, J. L. Beuzit, P. Blanchard, S. S. Brems, T. Buey, V. De Caprio, M. Carbillet, M. Carle, E. Cascone, A. Cheetham, R. Claudi, A. Costille, A. Delboulbé, K. Dohlen, D. Fantinel, P. Feautrier, T. Fusco, E. Giro, L. Gluck, C. Gry, N. Hubin, E. Hugot, M. Jaquet, D. Le Mignant, M. Llored, F. Madec, Y. Magnard, P. Martinez, D. Maurel, M. Meyer, O. Möller-Nilsson, T. Moulin, L. Mugnier, A. Origné, A. Pavlov, D. Perret, C. Petit, J. Pragt, P. Puget, P. Rabou, J. Ramos, F. Rigal, S. Rochat, R. Roelfsema, G. Rousset, A. Roux, B. Salasnich, J. F. Sauvage, A. Sevin, C. Soenke, E. Stadler, M. Suarez, M. Turatto, and L. Weber. Discovery of a planetary-mass companion within the gap of the transition disk around PDS 70. *Astronomy and Astrophysics*, 617:A44, September 2018.

[92] K. Koch, B. Hunger, O. Klepel, and M. Heuchel. A new method of analysing temperature-programmed desorption (tpd) profiles using an extended integral equation. *Journal of Catalysis*, 172:187–193, 11 1997.

[93] Quentin Kral, Sebastian Marino, Mark C Wyatt, Mihkel Kama, and Luca Matrá. Imaging [ci] around hd 131835: reinterpreting young debris discs with protoplanetary disc levels of co gas as shielded secondary discs. *Monthly Notices of the Royal Astronomical Society*, 11 2018.

[94] Quentin Kral, Luca Matrà, Mark C. Wyatt, and Grant M. Kennedy. Predictions for the secondary co, c and o gas content of debris discs from the destruction of volatile-rich planetesimals. *Monthly Notices of the Royal Astronomical Society*, 469:521–550, 7 2017.

[95] Sebastiaan Krijt, Fred J. Ciesla, and Edwin A. Bergin. Tracing Water Vapor and Ice During Dust Growth. *The Astrophysical Journal*, 833(2):285, December 2016.

[96] Sebastiaan Krijt, Kamber R. Schwarz, Edwin A. Bergin, and Fred J. Ciesla. Transport of CO in Protoplanetary Disks: Consequences of Pebble Formation,

Settling, and Radial Drift. *The Astrophysical Journal*, 864(1):78, September 2018.

[97] Hiroyuki Kurokawa, Yayoi N. Miura, Seiji Sugita, Yuichiro Cho, François Leblanc, Naoki Terada, and Hiromu Nakagawa. Mars' atmospheric neon suggests volatile-rich primitive mantle. *Icarus*, 370:114685, December 2021.

[98] Helmut Lammer, Ramon Brasser, Anders Johansen, Manuel Scherf, and Martin Leitzinger. Formation of Venus, Earth and Mars: Constrained by Isotopes. *Space Science Reviews*, 217(1):7, February 2021.

[99] Helmut Lammer, Aubrey L. Zerkle, Stefanie Gebauer, Nicola Tosi, Lena Noack, Manuel Scherf, Elke Pilat-Lohinger, Manuel Güdel, John Lee Grenfell, Mareike Godolt, and Athanasia Nikolaou. Origin and evolution of the atmospheres of early venus, earth and mars. *The Astronomy and Astrophysics Review*, 26:2, 11 2018.

[100] Trish Lauck, Leendertjan Karssemeijer, Katherine Shulenberger, Mahesh Rajappan, Karin I Öberg, and Herma M Cuppen. Co diffusion into amorphous h 2 o ices. *The Astrophysical Journal*, 801:118, 2015.

[101] A. Li and J. M. Greenberg. A unified model of interstellar dust. *Astronomy and Astrophysics*, 323:566–584, July 1997.

[102] Aigen Li and B. T. Draine. Infrared Emission from Interstellar Dust. II. The Diffuse Interstellar Medium. *The Astrophysical Journal*, 554(2):778–802, June 2001.

[103] Aigen Li and J. Mayo Greenberg. A comet dust model for the beta Pictoris disk. *Astronomy and Astrophysics*, 331:291–313, March 1998.

[104] Hailong Li, Aigerim Karina, Marjorie Ladd-Parada, Alexander Späh, Fivos Perakis, Chris Benmore, and Katrin Amann-Winkel. Long-range structures of amorphous solid water. *The Journal of Physical Chemistry B*, 125:13320–13328, 12 2021.

[105] C. M. Lisse, C. H. Chen, M. C. Wyatt, A. Morlok, I. Song, G. Bryden, and P. Sheehan. Abundant circumstellar silica dust and sio gas created by a giant hypervelocity collision in the 12 myr hd172555 system. *Astrophysical Journal*, 701:2019–2032, 2009.

[106] Meredith A. MacGregor, Samantha M. Lawler, David J. Wilner, Brenda C. Matthews, Grant M. Kennedy, Mark Booth, and James Di Francesco. ALMA Observations of the Debris Disk of Solar Analog τ Ceti. *The Astrophysical Journal*, 828(2):113, September 2016.

[107] Meredith A. MacGregor, Luca Matrà, Paul Kalas, David J. Wilner, Margaret Pan, Grant M. Kennedy, Mark C. Wyatt, Gaspard Duchene, A. Meredith

Hughes, George H. Rieke, Mark Clampin, Michael P. Fitzgerald, James R. Graham, Wayne S. Holland, Olja Panić, Andrew Shannon, and Kate Su. A Complete ALMA Map of the Fomalhaut Debris Disk. *The Astrophysical Journal*, 842(1):8, June 2017.

[108] Meredith A. MacGregor, Alycia J. Weinberger, A. Meredith Hughes, D. J. Wilner, Thayne Currie, John H. Debes, Jessica K. Donaldson, Seth Redfield, Aki Roberge, and Glenn Schneider. ALMA Detection of Extended Millimeter Halos in the HD 32297 and HD 61005 Debris Disks. *The Astrophysical Journal*, 869(1):75, December 2018.

[109] Meredith A. MacGregor, Alycia J. Weinberger, Erika R. Nesvold, A. Meredith Hughes, D. J. Wilner, Thayne Currie, John H. Debes, Jessica K. Donaldson, Seth Redfield, Aki Roberge, and Glenn Schneider. Multiple Rings of Millimeter Dust Emission in the HD 15115 Debris Disk. *The Astrophysical Journal*, 877(2):L32, June 2019.

[110] Eric E. Mamajek. Initial Conditions of Planet Formation: Lifetimes of Primordial Disks. In Tomonori Usuda, Motohide Tamura, and Miki Ishii, editors, *Exoplanets and Disks: Their Formation and Diversity*, volume 1158 of *American Institute of Physics Conference Series*, pages 3–10, August 2009.

[111] Eric E. Mamajek and Cameron P. M. Bell. On the age of the β pictoris moving group. *Monthly Notices of the Royal Astronomical Society*, 445:2169–2180, 12 2014.

[112] U. Marboeuf, A. Bonsor, and J.-C. Augereau. Extrasolar comets: The origin of dust in exozodiacal disks? *Planetary and Space Science*, 133:47–62, 11 2016.

[113] S. Marino, L. Matrà, C. Stark, M. C. Wyatt, S. Casassus, G. Kennedy, D. Rodriguez, B. Zuckerman, S. Perez, W. R. F. Dent, M. Kuchner, A. M. Hughes, G. Schneider, A. Steele, A. Roberge, J. Donaldson, and E. Nesvold. Exocometary gas in the hd 181327 debris ring. *Monthly Notices of the Royal Astronomical Society*, 460:2933–2944, 8 2016.

[114] S. Marino, M. C. Wyatt, O. Panić, L. Matrà, G. M. Kennedy, A. Bonsor, Q. Kral, W. R. F Dent, G. Duchene, D. Wilner, C. M. Lisse, J.-F. Lestrade, and B. Matthews. Alma observations of the η corvi debris disc: inward scattering of co-rich exocomets by a chain of 3–30 $m_\oplus$ planets? *Monthly Notices of the Royal Astronomical Society*, 465:2595–2615, 3 2017.

[115] S. Marino, B. Yelverton, M. Booth, V. Faramaz, G. M. Kennedy, L. Matrà, and M. C. Wyatt. A gap in HD 92945's broad planetesimal disc revealed by ALMA. *Monthly Notices of the Royal Astronomical Society*, 484(1):1257–1269, March 2019.

[116] Sebastian Marino, Amy Bonsor, Mark C Wyatt, and Quentin Kral. Scattering of exocomets by a planet chain: exozodi levels and the delivery of cometary

material to inner planets. *Monthly Notices of the Royal Astronomical Society*, 479:1651–1671, 9 2018.

[117] Margarita M. Marinova, Oded Aharonson, and Erik Asphaug. Mega-impact formation of the mars hemispheric dichotomy. *Nature*, 453:1216–1219, 6 2008.

[118] Jonathan P. Marshall, S. T. Maddison, E. Thilliez, B. C. Matthews, D. J. Wilner, J. S. Greaves, and W. S. Holland. New constraints on the millimetre emission of six debris discs. *Monthly Notices of the Royal Astronomical Society*, 468(3):2719–2725, July 2017.

[119] R. Martín-Doménech, J. Manzano-Santamaría, G. M. Muñoz Caro, G. A. Cruz-Díaz, Y.-J. Chen, V. J. Herrero, and I. Tanarro. Uv photoprocessing of co ₂ ice: a complete quantification of photochemistry and photon-induced desorption processes. *Astronomy & Astrophysics*, 584:A14, 12 2015.

[120] Rafael Martín-Doménech, Pavlo Maksiutenko, Karin I. Öberg, and Mahesh Rajappan. Exploring the Chemistry Induced by Energetic Processing of the H2-bearing, CO-rich Apolar Ice Layer. *Astrophysical Journal*, 902(2):116, October 2020.

[121] B. Marty, K. Altwegg, H. Balsiger, A. Bar-Nun, D. V. Bekaert, J.-J. Berthelier, A. Bieler, C. Briois, U. Calmonte, M. Combi, J. De Keyser, B. Fiethe, S. A. Fuselier, S. Gasc, T. I. Gombosi, K. C. Hansen, M. Hässig, A. Jäckel, E. Kopp, A. Korth, L. Le Roy, U. Mall, O. Mousis, T. Owen, H. Rème, M. Rubin, T. Sémon, C.-Y. Tzou, J. H. Waite, and P. Wurz. Xenon isotopes in 67p/churyumov-gerasimenko show that comets contributed to earth's atmosphere. *Science*, 356:1069–1072, 2017.

[122] B. Marty and A. Meibom. Noble gas signature of the late heavy bombardment in the earth's atmosphere. *Earth*, 2:43–49, 10 2007.

[123] Bernard Marty. The origins and concentrations of water, carbon, nitrogen and noble gases on earth. *Earth and Planetary Science Letters*, 313-314:56–66, 1 2012.

[124] Bernard Marty, Guillaume Avice, Yuji Sano, Kathrin Altwegg, Hans Balsiger, Myrtha Hässig, Alessandro Morbidelli, Olivier Mousis, and Martin Rubin. Origins of volatile elements (h, c, n, noble gases) on earth and mars in light of recent results from the rosetta cometary mission. *Earth and Planetary Science Letters*, 441:91–102, 2016.

[125] Alessandra Mastrobuono-Battisti, Hagai B. Perets, and Sean N. Raymond. A primordial origin for the compositional similarity between the earth and the moon. *Nature*, 520:212–215, 4 2015.

[126] L. Matrà, M. A. MacGregor, P. Kalas, M. C. Wyatt, G. M. Kennedy, D. J. Wilner, G. Duchene, A. M. Hughes, M. Pan, A. Shannon, M. Clampin, M. P.

Fitzgerald, J. R. Graham, W. S. Holland, O. Panić, and K. Y. L. Su. Detection of exocometary co within the 440 myr old fomalhaut belt: A similar co+co ₂ ice abundance in exocomets and solar system comets. *The Astrophysical Journal*, 842:9, 6 2017.

[127] L. Matrà, S. Marino, G. M. Kennedy, M. C. Wyatt, K. I. Öberg, and D. J. Wilner. An empirical planetesimal belt radius–stellar luminosity relation. *The Astrophysical Journal*, 859:72, 5 2018.

[128] L. Matrà, O. Panić, M. C. Wyatt, and W. R.F. Dent. Co mass upper limits in the fomalhaut ring - the importance of nlte excitation in debris discs and future prospects with alma. *Monthly Notices of the Royal Astronomical Society*, 447:3936–3947, 2015.

[129] L. Matrà, D. J. Wilner, K. I. Öberg, S. M. Andrews, R. A. Loomis, M. C. Wyatt, and W. R. F. Dent. Molecular reconnaissance of the β pictoris gas disk with the sma: A low hcn/(co+co ₂) outgassing ratio and predictions for future surveys. *The Astrophysical Journal*, 853:147, 2 2018.

[130] L. Matrà, K. I. Öberg, D. J. Wilner, J. Olofsson, and A. Bayo. On the ubiquity and stellar luminosity dependence of exocometary co gas: Detection around m dwarf twa 7. *The Astronomical Journal*, 157:117, 2 2019.

[131] Brenda C. Matthews, Paul G. Kalas, and Mark C. Wyatt. Mass and Temperature of the TWA 7 Debris Disk. *The Astrophysical Journal*, 663(2):1103–1109, July 2007.

[132] Marco Minissale, Yuri Aikawa, Edwin Bergin, M. Bertin, Wendy A. Brown, Stephanie Cazaux, Steven B. Charnley, Audrey Coutens, Herma M. Cuppen, Victoria Guzman, Harold Linnartz, Martin R. S. McCoustra, Albert Rimola, Johanna G. M. Schrauwen, Celine Toubin, Piero Ugliengo, Naoki Watanabe, Valentine Wakelam, and Francois Dulieu. Thermal desorption of interstellar ices. A review on the controlling parameters and their implications fromsnowlines to chemical complexity. *arXiv e-prints*, page arXiv:2201.07512, January 2022.

[133] Tushar Mittal, Christine H. Chen, Hannah Jang-Condell, P. Manoj, Benjamin A. Sargent, Dan M. Watson, and Carey M. Lisse. The Spitzer Infrared Spectrograph Debris Disk Catalog. II. Silicate Feature Analysis of Unresolved Targets. *The Astrophysical Journal*, 798(2):87, January 2015.

[134] B. Montesinos, C. Eiroa, A. V. Krivov, J. P. Marshall, G. L. Pilbratt, R. Liseau, A. Mora, J. Maldonado, S. Wolf, S. Ertel, A. Bayo, J. C. Augereau, A. M. Heras, M. Fridlund, W. C. Danchi, E. Solano, F. Kirchschlager, C. del Burgo, and D. Montes. Incidence of debris discs around FGK stars in the solar neighbourhood. *Astronomy and Astrophysics*, 593:A51, September 2016.

[135] A. Morbidelli, M. Lambrechts, S. Jacobson, and B. Bitsch. The great dichotomy of the Solar System: Small terrestrial embryos and massive giant planet cores. *Icarus*, 258:418–429, September 2015.

[136] A Morbidelli, J. I. Lunine, D. P. O'Brien, S. N. Raymond, and K. J. Walsh. Building terrestrial planets. *Annual Review of Earth and Planetary Sciences*, 40:251–275, 5 2012.

[137] M. A. Morris and S. J. Desch. Thermal histories of chondrules in solar nebula shocks. *The Astrophysical Journal*, 722:1474–1494, 10 2010.

[138] Olivier Mousis, Jonathan I. Lunine, Sylvain Picaud, Daniel Cordier, J. Hunter Waite Jr., and Kathleen E. Mandt. Removal of titan's atmospheric noble gases by their sequestration in surface clathrates. *The Astrophysical Journal*, 740:L9, 10 2011.

[139] Olivier Mousis, Jonathan I. Lunine, Caroline Thomas, Matthew Pasek, Ulysse Marbœuf, Yann Alibert, Vincent Ballenegger, Daniel Cordier, Yves Ellinger, Françoise Pauzat, and Sylvain Picaud. Clathration of volatiles in the solar nebula and implications for the origin of titan's atmosphere. *The Astrophysical Journal*, 691:1780–1786, 2 2009.

[140] Joan Najita and Jonathan P. Williams. An 850 μm Survey for Dust around Solar-Mass Stars. *The Astrophysical Journal*, 635(1):625–635, December 2005.

[141] Yoshitsugu Nakagawa, Minoru Sekiya, and Chushiro Hayashi. Settling and growth of dust particles in a laminar phase of a low-mass solar nebula. *Icarus*, 67:375–390, 9 1986.

[142] David Nesvorný, William F. Bottke, Harold F. Levison, and Luke Dones. Recent Origin of the Solar System Dust Bands. *The Astrophysical Journal*, 591(1):486–497, July 2003.

[143] David Nesvorný, Peter Jenniskens, Harold F. Levison, William F. Bottke, David Vokrouhlický, and Matthieu Gounelle. Cometary Origin of the Zodiacal Cloud and Carbonaceous Micrometeorites. Implications for Hot Debris Disks. *The Astrophysical Journal*, 713(2):816–836, April 2010.

[144] David Nesvorný, David Vokrouhlický, and Alessandro Morbidelli. Capture of Trojans by Jumping Jupiter. *The Astrophysical Journal*, 768(1):45, May 2013.

[145] David A. Neufeld, Miwa Goto, T. R. Geballe, Rolf Güsten, Karl M. Menten, and Helmut Wiesemeyer. Detection of Vibrational Emissions from the Helium Hydride Ion (HeH^+) in the Planetary Nebula NGC 7027. *Astrophysical Journal*, 894(1):37, May 2020.

[146] H. B. Niemann, S. K. Atreya, J. E. Demick, D. Gautier, J. A. Haberman, D. N. Harpold, W. T. Kasprzak, J. I. Lunine, T. C. Owen, and F. Raulin. Composition of titan's lower atmosphere and simple surface volatiles as measured by

the cassini-huygens probe gas chromatograph mass spectrometer experiment. *Journal of Geophysical Research*, 115:E12006, 12 2010.

[147] G. A. Niklasson, C. G. Granqvist, and O. Hunderi. Effective medium models for the optical properties of inhomogeneous materials. *Applied Optics*, 20(1):26–30, January 1981.

[148] F. Nimmo, S. D. Hart, D. G. Korycansky, and C. B. Agnor. Implications of an impact origin for the martian hemispheric dichotomy. *Nature*, 453:1220–1223, 6 2008.

[149] J. A. Noble, E. Congiu, F. Dulieu, and H. J. Fraser. Thermal desorption characteristics of co, o2 and co2 on non-porous water, crystalline water and silicate surfaces at submonolayer and multilayer coverages. *Monthly Notices of the Royal Astronomical Society*, pages no–no, 1 2012.

[150] G. Notesco and A. Bar-Nun. A ∼25 k temperature of formation for the submicron ice grains which formed comets. *Icarus*, 175:546–550, 6 2005.

[151] G Notesco, D. Laufer, A. Bar-Nun, and T. Owen. An experimental study of the isotopic enrichment in ar, kr, and xe when trapped in water ice. *Icarus*, 142:298–300, 11 1999.

[152] Karin I. Öberg and Edwin A. Bergin. Astrochemistry and compositions of planetary systems. *Physics Reports*, 893:1–48, January 2021.

[153] Karin I. Öberg, Viviana V. Guzmán, Catherine Walsh, Yuri Aikawa, Edwin A. Bergin, Charles J. Law, Ryan A. Loomis, Felipe Alarcón, Sean M. Andrews, Jaehan Bae, Jennifer B. Bergner, Yann Boehler, Alice S. Booth, Arthur D. Bosman, Jenny K. Calahan, Gianni Cataldi, L. Ilsedore Cleeves, Ian Czekala, Kenji Furuya, Jane Huang, John D. Ilee, Nicolas T. Kurtovic, Romane Le Gal, Yao Liu, Feng Long, François Ménard, Hideko Nomura, Laura M. Pérez, Chunhua Qi, Kamber R. Schwarz, Anibal Sierra, Richard Teague, Takashi Tsukagoshi, Yoshihide Yamato, Merel L. R. van't Hoff, Abygail R. Waggoner, David J. Wilner, and Ke Zhang. Molecules with ALMA at Planet-forming Scales (MAPS). I. Program Overview and Highlights. *The Astrophysical Journal Supplement Series*, 257(1):1, November 2021.

[154] Karin I. Öberg, Ruth Murray-Clay, and Edwin A. Bergin. The effects of snowlines on c/o in planetary atmospheres. *The Astrophysical Journal*, 743:L16, 12 2011.

[155] Karin I Öberg and Robin Wordsworth. Jupiter's composition suggests its core assembled exterior to the n ₂ snowline. *The Astronomical Journal*, 158:194, 10 2019.

[156] David P. O'Brien, Alessandro Morbidelli, and William F. Bottke. The primordial excitation and clearing of the asteroid belt—Revisited. *Icarus*, 191(2):434–452, November 2007.

[157] Kazumasa Ohno and Takahiro Ueda. Jupiter's "cold" formation in the protosolar disk shadow. *Astronomy & Astrophysics*, 651:L2, 7 2021.

[158] J. Olofsson, A. Juhász, Th. Henning, H. Mutschke, A. Tamanai, A. Moór, and P. Ábrahám. Transient dust in warm debris disks (Corrigendum). Detection of Fe-rich olivine grains. *Astronomy and Astrophysics*, 547:C1, November 2012.

[159] Masaaki Otsuka and Akito Tajitsu. Chemical Abundances in the Extremely Carbon-rich and Xenon-rich Halo Planetary Nebula H4-1. *Astrophysical Journal*, 778(2):146, December 2013.

[160] Deborah L. Padgett, Lucas Cieza, Karl R. Stapelfeldt, II Evans, Neal J., David Koerner, Anneila Sargent, Misato Fukagawa, Ewine F. van Dishoeck, Jean-Charles Augereau, Lori Allen, Geoff Blake, Tim Brooke, Nicholas Chapman, Paul Harvey, Alicia Porras, Shih-Ping Lai, Lee Mundy, Philip C. Myers, William Spiesman, and Zahed Wahhaj. The SPITZER c2d Survey of Weak-Line T Tauri Stars. I. Initial Results. *The Astrophysical Journal*, 645(2):1283–1296, July 2006.

[161] Nicole Pawellek and Alexander V. Krivov. The dust grain size-stellar luminosity trend in debris discs. *Monthly Notices of the Royal Astronomical Society*, 454(3):3207–3221, December 2015.

[162] P. Pinilla, A. Pohl, S. M. Stammler, and T. Birnstiel. Dust Density Distribution and Imaging Analysis of Different Ice Lines in Protoplanetary Disks. *The Astrophysical Journal*, 845(1):68, August 2017.

[163] Ana-Maria A. Piso, Karin I. Öberg, Tilman Birnstiel, and Ruth A. Murray-Clay. C/O and Snowline Locations in Protoplanetary Disks: The Effect of Radial Drift and Viscous Gas Accretion. *The Astrophysical Journal*, 815(2):109, December 2015.

[164] Dina Prialnik and Eric D. Rosenberg. Can ice survive in main-belt comets? long-term evolution models of comet 133p/elst-pizarro. *Monthly Notices of the Royal Astronomical Society: Letters*, 399:L79–L83, 10 2009.

[165] Silvia Protopapa, Jessica M. Sunshine, Lori M. Feaga, Michael S. P. Kelley, Michael F. A'Hearn, Tony L. Farnham, Olivier Groussin, Sebastien Besse, Frédéric Merlin, and Jian-Yang Li. Water ice and dust in the innermost coma of comet 103P/Hartley 2. *Icarus*, 238:191–204, August 2014.

[166] T. Prusti, J. H. J. de Bruijne, A. G. A. Brown, A. Vallenari, C. Babusiaux, C. A. L. Bailer-Jones, U. Bastian, M. Biermann, D. W. Evans, L. Eyer, F. Jansen, C. Jordi, S. A. Klioner, U. Lammers, L. Lindegren, X. Luri, F. Mignard, D. J. Milligan, C. Panem, V. Poinsignon, D. Pourbaix, S. Randich, G. Sarri, P. Sartoretti, H. I. Siddiqui, C. Soubiran, V. Valette, F. van Leeuwen, N. A. Walton, C. Aerts, F. Arenou, M. Cropper, R. Drimmel, E. Høg, D. Katz, M. G. Lattanzi, W. O'Mullane, E. K. Grebel, A. D. Holland, C. Huc, X. Passot,

L. Bramante, C. Cacciari, J. Castañeda, L. Chaoul, N. Cheek, F. De Angeli, C. Fabricius, R. Guerra, J. Hernández, A. Jean-Antoine-Piccolo, E. Masana, R. Messineo, N. Mowlavi, K. Nienartowicz, D. Ordóñez-Blanco, P. Panuzzo, J. Portell, P. J. Richards, M. Riello, G. M. Seabroke, P. Tanga, F. Thévenin, J. Torra, S. G. Els, G. Gracia-Abril, G. Comoretto, M. Garcia-Reinaldos, T. Lock, E. Mercier, M. Altmann, R. Andrae, T. L. Astraatmadja, I. Bellas-Velidis, K. Benson, J. Berthier, R. Blomme, G. Busso, B. Carry, A. Cellino, G. Clementini, S. Cowell, O. Creevey, J. Cuypers, M. Davidson, J. De Ridder, A. de Torres, L. Delchambre, A. Dell'Oro, C. Ducourant, Y. Frémat, M. García-Torres, E. Gosset, J.-L. Halbwachs, N. C. Hambly, D. L. Harrison, M. Hauser, D. Hestroffer, S. T. Hodgkin, H. E. Huckle, A. Hutton, G. Jasniewicz, S. Jordan, M. Kontizas, A. J. Korn, A. C. Lanzafame, M. Manteiga, A. Moitinho, K. Muinonen, J. Osinde, E. Pancino, T. Pauwels, J.-M. Petit, A. Recio-Blanco, A. C. Robin, L. M. Sarro, C. Siopis, M. Smith, K. W. Smith, A. Sozzetti, W. Thuillot, W. van Reeven, Y. Viala, U. Abbas, A. Abreu Aramburu, S. Accart, J. J. Aguado, P. M. Allan, W. Allasia, G. Altavilla, M. A. Álvarez, J. Alves, R. I. Anderson, A. H. Andrei, E. Anglada Varela, E. Antiche, T. Antoja, S. Antón, B. Arcay, A. Atzei, L. Ayache, N. Bach, S. G. Baker, L. Balaguer-Núñez, C. Barache, C. Barata, A. Barbier, F. Barblan, M. Baroni, D. Barrado y Navascués, M. Barros, M. A. Barstow, U. Becciani, M. Bellazzini, G. Bellei, A. Bello García, V. Belokurov, P. Bendjoya, A. Berihuete, L. Bianchi, O. Bienaymé, F. Billebaud, N. Blagorodnova, S. Blanco-Cuaresma, T. Boch, A. Bombrun, R. Borrachero, S. Bouquillon, G. Bourda, H. Bouy, A. Bragaglia, M. A. Breddels, N. Brouillet, T. Brüsemeister, B. Bucciarelli, F. Budnik, P. Burgess, R. Burgon, A. Burlacu, D. Busonero, R. Buzzi, E. Caffau, J. Cambras, H. Campbell, R. Cancelliere, T. Cantat-Gaudin, T. Carlucci, J. M. Carrasco, M. Castellani, P. Charlot, J. Charnas, P. Charvet, F. Chassat, A. Chiavassa, M. Clotet, G. Cocozza, R. S. Collins, P. Collins, G. Costigan, F. Crifo, N. J. G. Cross, M. Crosta, C. Crowley, C. Dafonte, Y. Damerdji, A. Dapergolas, P. David, M. David, P. De Cat, F. de Felice, P. de Laverny, F. De Luise, R. De March, D. de Martino, R. de Souza, J. Debosscher, E. del Pozo, M. Delbo, A. Delgado, H. E. Delgado, F. di Marco, P. Di Matteo, S. Diakite, E. Distefano, C. Dolding, S. Dos Anjos, P. Drazinos, J. Durán, Y. Dzigan, E. Ecale, B. Edvardsson, H. Enke, M. Erdmann, D. Escolar, M. Espina, N. W. Evans, G. Eynard Bontemps, C. Fabre, M. Fabrizio, S. Faigler, A. J. Falcão, M. Farràs Casas, F. Faye, L. Federici, G. Fedorets, J. Fernández-Hernández, P. Fernique, A. Fienga, F. Figueras, F. Filippi, K. Findeisen, A. Fonti, M. Fouesneau, E. Fraile, M. Fraser, J. Fuchs, R. Furnell, M. Gai, S. Galleti, L. Galluccio, D. Garabato, F. García-Sedano, P. Garé, A. Garofalo, N. Garralda, P. Gavras, J. Gerssen, R. Geyer, G. Gilmore, S. Girona, G. Giuffrida, M. Gomes, A. González-Marcos, J. González-Núñez, J. J. González-Vidal, M. Granvik, A. Guerrier, P. Guillout, J. Guiraud, A. Gúrpide, R. Gutiérrez-Sánchez, L. P. Guy, R. Haigron, D. Hatzidimitriou, M. Haywood, U. Heiter, A. Helmi, D. Hobbs, W. Hofmann, B. Holl, G. Holland, J. A. S. Hunt, A. Hypki, V. Icardi, M. Irwin, G. Jevardat de Fombelle, P. Jofré, P. G. Jonker, A. Jorissen,

F. Julbe, A. Karampelas, A. Kochoska, R. Kohley, K. Kolenberg, E. Kontizas, S. E. Koposov, G. Kordopatis, P. Koubsky, A. Kowalczyk, A. Krone-Martins, M. Kudryashova, I. Kull, R. K. Bachchan, F. Lacoste-Seris, A. F. Lanza, J.-B. Lavigne, C. Le Poncin-Lafitte, Y. Lebreton, T. Lebzelter, S. Leccia, N. Leclerc, I. Lecoeur-Taibi, V. Lemaitre, H. Lenhardt, F. Leroux, S. Liao, E. Licata, H. E. P. Lindstrøm, T. A. Lister, E. Livanou, A. Lobel, W. Löffler, M. López, A. Lopez-Lozano, D. Lorenz, T. Loureiro, I. MacDonald, T. Magalhães Fernandes, S. Managau, R. G. Mann, G. Mantelet, O. Marchal, J. M. Marchant, M. Marconi, J. Marie, S. Marinoni, P. M. Marrese, G. Marschalkó, D. J. Marshall, J. M. Martín-Fleitas, M. Martino, N. Mary, G. Matijevič, T. Mazeh, P. J. McMillan, S. Messina, A. Mestre, D. Michalik, N. R. Millar, B. M. H. Miranda, D. Molina, R. Molinaro, M. Molinaro, L. Molnár, M. Moniez, P. Montegriffo, D. Monteiro, R. Mor, A. Mora, R. Morbidelli, T. Morel, S. Morgenthaler, T. Morley, D. Morris, A. F. Mulone, T. Muraveva, I. Musella, J. Narbonne, G. Nelemans, L. Nicastro, L. Noval, C. Ordénovic, J. Ordieres-Meré, P. Osborne, C. Pagani, I. Pagano, F. Pailler, H. Palacin, L. Palaversa, P. Parsons, T. Paulsen, M. Pecoraro, R. Pedrosa, H. Pentikäinen, J. Pereira, B. Pichon, A. M. Piersimoni, F.-X. Pineau, E. Plachy, G. Plum, E. Poujoulet, A. Prša, L. Pulone, S. Ragaini, S. Rago, N. Rambaux, M. Ramos-Lerate, P. Ranalli, G. Rauw, A. Read, S. Regibo, F. Renk, C. Reylé, R. A. Ribeiro, L. Rimoldini, V. Ripepi, A. Riva, G. Rixon, M. Roelens, M. Romero-Gómez, N. Rowell, F. Royer, A. Rudolph, L. Ruiz-Dern, G. Sadowski, T. Sagristà Sellés, J. Sahlmann, J. Salgado, E. Salguero, M. Sarasso, H. Savietto, A. Schnorhk, M. Schultheis, E. Sciacca, M. Segol, J. C. Segovia, D. Segransan, E. Serpell, I-C. Shih, R. Smareglia, R. L. Smart, C. Smith, E. Solano, F. Solitro, R. Sordo, S. Soria Nieto, J. Souchay, A. Spagna, F. Spoto, U. Stampa, I. A. Steele, H. Steidelmüller, C. A. Stephenson, H. Stoev, F. F. Suess, M. Süveges, J. Surdej, L. Szabados, E. Szegedi-Elek, D. Tapiador, F. Taris, G. Tauran, M. B. Taylor, R. Teixeira, D. Terrett, B. Tingley, S. C. Trager, C. Turon, A. Ulla, E. Utrilla, G. Valentini, A. van Elteren, E. Van Hemelryck, M. van Leeuwen, M. Varadi, A. Vecchiato, J. Veljanoski, T. Via, D. Vicente, S. Vogt, H. Voss, V. Votruba, S. Voutsinas, G. Walmsley, M. Weiler, K. Weingrill, D. Werner, T. Wevers, G. Whitehead, Ł. Wyrzykowski, A. Yoldas, M. Žerjal, S. Zucker, C. Zurbach, T. Zwitter, A. Alecu, M. Allen, C. Allende Prieto, A. Amorim, G. Anglada-Escudé, V. Arsenijevic, S. Azaz, P. Balm, M. Beck, H.-H. Bernstein, L. Bigot, A. Bijaoui, C. Blasco, M. Bonfigli, G. Bono, S. Boudreault, A. Bressan, S. Brown, P.-M. Brunet, P. Bunclark, R. Buonanno, A. G. Butkevich, C. Carret, C. Carrion, L. Chemin, F. Chéreau, L. Corcione, E. Darmigny, K. S. de Boer, P. de Teodoro, P. T. de Zeeuw, C. Delle Luche, C. D. Domingues, P. Dubath, F. Fodor, B. Frézouls, A. Fries, D. Fustes, D. Fyfe, E. Gallardo, J. Gallegos, D. Gardiol, M. Gebran, A. Gomboc, A. Gómez, E. Grux, A. Gueguen, A. Heyrovsky, J. Hoar, G. Iannicola, Y. Isasi Parache, A.-M. Janotto, E. Joliet, A. Jonckheere, R. Keil, D.-W. Kim, P. Klagyivik, J. Klar, J. Knude, O. Kochukhov, I. Kolka, J. Kos, A. Kutka, V. Lainey, D. LeBouquin, C. Liu, D. Loreggia, V. V. Makarov, M. G. Marseille, C. Martayan, O. Martinez-Rubi, B. Massart, F. Mey-

nadier, S. Mignot, U. Munari, A.-T. Nguyen, T. Nordlander, P. Ocvirk, K. S. O'Flaherty, A. Olias Sanz, P. Ortiz, J. Osorio, D. Oszkiewicz, A. Ouzounis, M. Palmer, P. Park, E. Pasquato, C. Peltzer, J. Peralta, F. Péturaud, T. Pieniluoma, E. Pigozzi, J. Poels, G. Prat, T. Prod'homme, F. Raison, J. M. Rebordao, D. Risquez, B. Rocca-Volmerange, S. Rosen, M. I. Ruiz-Fuertes, F. Russo, S. Sembay, I. Serraller Vizcaino, A. Short, A. Siebert, H. Silva, D. Sinachopoulos, E. Slezak, M. Soffel, D. Sosnowska, V. Straižys, M. ter Linden, D. Terrell, S. Theil, C. Tiede, L. Troisi, P. Tsalmantza, D. Tur, M. Vaccari, F. Vachier, P. Valles, W. Van Hamme, L. Veltz, J. Virtanen, J.-M. Wallut, R. Wichmann, M. I. Wilkinson, H. Ziaeepour, and S. Zschocke. The gaia mission. *Astronomy & Astrophysics*, 595:A1, 11 2016.

[167] P.A. Redhead. Thermal desorption of gases. *Vacuum*, 12:203–211, 7 1962.

[168] R. Rejoub, B. G. Lindsay, and R. F. Stebbings. Determination of the absolute partial and total cross sections for electron-impact ionization of the rare gases. *Physical Review A*, 65:042713, 4 2002.

[169] Bin Ren, Élodie Choquet, Marshall D. Perrin, Dimitri Mawet, Christine H. Chen, Julien Milli, John H. Debes, Isabel Rebollido, Christopher C. Stark, J. Brendan Hagan, Dean C. Hines, Maxwell A. Millar-Blanchaer, Laurent Pueyo, Aki Roberge, Glenn Schneider, Eugene Serabyn, Rémi Soummer, and Schuyler G. Wolff. A Layered Debris Disk around M Star TWA 7 in Scattered Light. *The Astrophysical Journal*, 914(2):95, June 2021.

[170] L. Ricci, J. M. Carpenter, B. Fu, A. M. Hughes, S. Corder, and A. Isella. ALMA Observations of the Debris Disk around the Young Solar Analog HD 107146. *The Astrophysical Journal*, 798(2):124, January 2015.

[171] Timothy J. Rodigas, Christopher C. Stark, Alycia Weinberger, John H. Debes, Philip M. Hinz, Laird Close, Christine Chen, Paul S. Smith, Jared R. Males, Andrew J. Skemer, Alfio Puglisi, Katherine B. Follette, Katie Morzinski, Ya-Lin Wu, Runa Briguglio, Simone Esposito, Enrico Pinna, Armando Riccardi, Glenn Schneider, and Marco Xompero. On the Morphology and Chemical Composition of the HR 4796A Debris Disk. *The Astrophysical Journal*, 798(2):96, January 2015.

[172] K. Ros and A. Johansen. Ice condensation as a planet formation mechanism. *Astronomy & Astrophysics*, 552:A137, 4 2013.

[173] Hilke E. Schlichting and Sujoy Mukhopadhyay. Atmosphere impact losses. *Space Science Reviews*, 214:34, 2 2018.

[174] Glenn Schneider, Carol A. Grady, Dean C. Hines, Christopher C. Stark, John H. Debes, Joe Carson, Marc J. Kuchner, Marshall D. Perrin, Alycia J. Weinberger, John P. Wisniewski, Murray D. Silverstone, Hannah Jang-Condell, Thomas Henning, Bruce E. Woodgate, Eugene Serabyn, Amaya Moro-Martin, Motohide

Tamura, Phillip M. Hinz, and Timothy J. Rodigas. Probing for Exoplanets Hiding in Dusty Debris Disks: Disk Imaging, Characterization, and Exploration with HST/STIS Multi-roll Coronagraphy. *The Astronomical Journal*, 148(4):59, October 2014.

[175] Glenn Schneider, Carol A. Grady, Christopher C. Stark, Andras Gaspar, Joseph Carson, John H. Debes, Thomas Henning, Dean C. Hines, Hannah Jang-Condell, Marc J. Kuchner, Marshall Perrin, Timothy J. Rodigas, Motohide Tamura, and John P. Wisniewski. Deep HST/STIS Visible-light Imaging of Debris Systems around Solar Analog Hosts. *The Astronomical Journal*, 152(3):64, September 2016.

[176] Tajana Schneiderman, Luca Matrà, Alan P. Jackson, Grant M. Kennedy, Quentin Kral, Sebastián Marino, Karin I. Öberg, Kate Y. L. Su, David J. Wilner, and Mark C. Wyatt. Carbon monoxide gas produced by a giant impact in the inner region of a young system. *Nature*, 598(7881):425–428, October 2021.

[177] Aldo G. Sepulveda, Luca Matrà, Grant M. Kennedy, Carlos del Burgo, Karin I. Öberg, David J. Wilner, Sebastián Marino, Mark Booth, John M. Carpenter, Claire L. Davies, William R. F. Dent, Steve Ertel, Jean-Francois Lestrade, Jonathan P. Marshall, Julien Milli, Mark C. Wyatt, Meredith A. MacGregor, and Brenda C. Matthews. The reasons survey: Resolved millimeter observations of a large debris disk around the nearby f star hd 170773. *The Astrophysical Journal*, 881:84, 8 2019.

[178] B. Sibthorpe, G. M. Kennedy, M. C. Wyatt, J. F. Lestrade, J. S. Greaves, B. C. Matthews, and G. Duchêne. Analysis of the Herschel DEBRIS Sun-like star sample. *Monthly Notices of the Royal Astronomical Society*, 475(3):3046–3064, April 2018.

[179] Alexia Simon, Karin I. Öberg, Mahesh Rajappan, and Pavlo Maksiutenko. Entrapment of co in co ₂ ice. *The Astrophysical Journal*, 883:21, 9 2019.

[180] R. Smith, M. C. Wyatt, and C. A. Haniff. Resolving the terrestrial planet forming regions of hd113766 and hd172555 with midi. *Monthly Notices of the Royal Astronomical Society*, 422:2560–2580, 2012.

[181] R. Scott Smith, R. Alan May, and Bruce D. Kay. Desorption kinetics of ar, kr, xe, n2, o2, co, methane, ethane, and propane from graphene and amorphous solid water surfaces. *Journal of Physical Chemistry B*, 120:1979–1987, 2016.

[182] Colin Snodgrass, Jessica Agarwal, Michael Combi, Alan Fitzsimmons, Aurelie Guilbert-Lepoutre, Henry H. Hsieh, Man-To Hui, Emmanuel Jehin, Michael S. P. Kelley, Matthew M. Knight, Cyrielle Opitom, Roberto Orosei, Miguel de Val-Borro, and Bin Yang. The main belt comets and ice in the solar system. *The Astronomy and Astrophysics Review*, 25:5, 11 2017.

[183] C. Spangler, A. I. Sargent, M. D. Silverstone, E. E. Becklin, and B. Zuckerman. Dusty Debris around Solar-Type Stars: Temporal Disk Evolution. *The Astrophysical Journal*, 555(2):932–944, July 2001.

[184] S. Alan Stern. On the Collisional Environment, Accretion Time Scales, and Architecture of the Massive, Primordial Kuiper Belt. *The Astronomical Journal*, 112:1203, September 1996.

[185] David J. Stevenson and Jonathan I. Lunine. Rapid formation of Jupiter by diffusive redistribution of water vapor in the solar nebula. *Icarus*, 75(1):146–155, July 1988.

[186] Kate Y. L. Su, George H. Rieke, Carl Melis, Alan P. Jackson, Paul S. Smith, Huan Y. A. Meng, and András Gáspár. Mid-infrared studies of hd 113766 and hd 172555: Assessing variability in the terrestrial zone of young exoplanetary systems. *The Astrophysical Journal*, 898:21, 7 2020.

[187] Steven L. Tait, Zdenek Dohnálek, Charles T. Campbell, and Bruce D. Kay. n-alkanes on mgo(100). i. coverage-dependent desorption kinetics of n-butane. *The Journal of Chemical Physics*, 122:164707, 4 2005.

[188] Edward W. Thommes, Geoffrey Bryden, Yanqin Wu, and Frederic A. Rasio. From Mean Motion Resonances to Scattered Planets: Producing the Solar System, Eccentric Exoplanets, and Late Heavy Bombardments. *The Astrophysical Journal*, 675(2):1538–1548, March 2008.

[189] A.G.G.M. Tielens and W. Hagen. Model calculations of the molecular composition of interstellar grain mantles. *Astronomy and Astrophysics*, 114:245–260, 1982.

[190] G. Tobie, D. Gautier, and F. Hersant. Titan's bulk composition constrained by cassini-huygens : Implication for internal outgassing. *The Astrophysical Journal*, 752:125, 6 2012.

[191] S. M. Vicente and J. Alves. Size distribution of circumstellar disks in the Trapezium cluster. *Astronomy and Astrophysics*, 441(1):195–205, October 2005.

[192] M. Villenave, K. R. Stapelfeldt, G. Duchene, F. Menard, M. Lambrechts, A. Sierra, C. Flores, W. R. F. Dent, S. Wolff, A. Ribas, M. Benisty, N. Cuello, and C. Pinte. A highly settled disk around Oph 163131. *arXiv e-prints*, page arXiv:2204.00640, April 2022.

[193] R. Visser, E. F. van Dishoeck, S. D. Doty, and C. P. Dullemond. The chemical history of molecules in circumstellar disks. *Astronomy & Astrophysics*, 495:881–897, 3 2009.

[194] Koji Wada, Hidekazu Tanaka, Satoshi Okuzumi, Hiroshi Kobayashi, Toru Suyama, Hiroshi Kimura, and Tetsuo Yamamoto. Growth efficiency of dust aggregates through collisions with high mass ratios. *Astronomy and Astrophysics*, 559:A62, November 2013.

[195] S. G. Warren. Optical constants of ice from the ultraviolet to the microwave. *Applied Optics*, 23:1206–1225, April 1984.

[196] Jacob Aaron White, J. Aufdenberg, A. C. Boley, M. Devlin, S. Dicker, P. Hauschildt, A. G. Hughes, A. M. Hughes, B. Mason, B. Matthews, A. Moór, T. Mroczkowski, C. Romero, J. Sievers, S. Stanchfield, F. Tapia, and D. Wilner. The mesas project: Long-wavelength follow-up observations of sirius a. *The Astrophysical Journal*, 875:55, 4 2019.

[197] Jonathan P. Williams and Lucas A. Cieza. Protoplanetary Disks and Their Evolution. *Annual Review of Astronomy and Astrophysics*, 49(1):67–117, September 2011.

[198] Hugh F. Wilson and Burkhard Militzer. Sequestration of noble gases in giant planet interiors. *Physical Review Letters*, 104:121101, 3 2010.

[199] M. C. Wyatt. Evolution of debris disks. *Annual Review of Astronomy and Astrophysics*, 46:339–383, September 2008.

[200] M. C. Wyatt, A. Bonsor, A. P. Jackson, S. Marino, and A. Shannon. How to design a planetary system for different scattering outcomes: giant impact sweet spot, maximizing exocomets, scattered discs. *Monthly Notices of the Royal Astronomical Society*, 464:3385–3407, 1 2017.

[201] M. C. Wyatt, S. F. Dermott, C. M. Telesco, R. S. Fisher, K. Grogan, E. K. Holmes, and R. K. Pina. How observations of circumstellar disk asymmetries can reveal hidden planets: Pericenter glow and its application to the hr 4796 disk. *The Astrophysical Journal*, 527:918–944, 12 1999.

[202] M. C. Wyatt, O. Panić, G. M. Kennedy, and L. Matrà. Five steps in the evolution from protoplanetary to debris disk. *Astrophysics and Space Science*, 357:103, 6 2015.

[203] M. C. Wyatt, R. Smith, J. S. Greaves, C. A. Beichman, G. Bryden, and C. M. Lisse. Transience of Hot Dust around Sun-like Stars. *The Astrophysical Journal*, 658(1):569–583, March 2007.

[204] M. C. Wyatt, R. Smith, K. Y. L. Su, G. H. Rieke, J. S. Greaves, C. A. Beichman, and G. Bryden. Steady state evolution of debris disks around a stars. *The Astrophysical Journal*, 663:365–382, 7 2007.

[205] Mark C. Wyatt and Alan P. Jackson. Insights into planet formation from debris disks. *Space Science Reviews*, 205:231–265, 12 2016.

[206] Ben Yelverton, Grant M Kennedy, Kate Y L Su, and Mark C Wyatt. A statistically significant lack of debris discs in medium separation binary systems. *Monthly Notices of the Royal Astronomical Society*, 488:3588–3606, 9 2019.

[207] Evgenij Zubko, Karri Muinonen, Gorden Videen, and Nikolai N. Kiselev. Dust in Comet C/1975 V1 (West). *Monthly Notices of the Royal Astronomical Society*, 440(4):2928–2943, June 2014.

[208] V. G. Zubko, V. Mennella, L. Colangeli, and E. Bussoletti. Optical constants of cosmic carbon analogue grains - I. Simulation of clustering by a modified continuous distribution of ellipsoids. *Monthly Notices of the Royal Astronomical Society*, 282(4):1321–1329, October 1996.

[209] B. Zuckerman and Inseok Song. A 40 myr old gaseous circumstellar disk at 49 ceti: Massive co-rich comet clouds at young a-type stars. *The Astrophysical Journal*, 758:77, 10 2012.

[210] B. Zuckerman, Inseok Song, M. S. Bessell, and R. A. Webb. The β pictoris moving group. *The Astrophysical Journal*, 562:L87–L90, 11 2001.

[211] Álvaro Ribas, Hervé Bouy, and Bruno Merín. Protoplanetary disk lifetimes vs. stellar mass and possible implications for giant planet populations. *Astronomy & Astrophysics*, 576:A52, 4 2015.